Cracow University of Technology

Faculty of Civil Engineering

Chair for Computational Engineering

Doctoral thesis

Multiscale finite element modeling of mechanical properties of selected advanced materials

Author:
Mateusz Dryzek, MSc

Supervisor:
Prof. Witold Cecot

Krakow, 2022

Abstract

In recent years, we can observe a significant development of new materials and the technological advancements these new materials have allowed. The most relevant examples would be these of composites, metamaterials, and 3D printing. The growing demand for numerical modeling that include multiscale nature of materials is the main motivation for the research presented in this dissertation. One example of a numerical method capable of resolving problems with many scales is the Multiscale Finite Element Method (MsFEM) that is the main topic of this thesis.

The thesis presents investigation on the MsFEM capabilities of modeling the mechanical behavior of advanced materials. During the course of the research, original modifications to the method were proposed and numerically tested to confirm its accuracy and efficiency. This includes: an introduction of the higher-order B-splines as a new way of building the MsFEM basis functions; modeling sandwich beams and plates with complex lattice layers using the anisotropic higher-order coarse-scale approximation and the novel shape functions that take into account the microscale boundary conditions incorporated into the method in the iterative corrector scheme; and an adaptation of MsFEM for modeling the mechanical behavior of 3D printed elements using a three-scale approach. Moreover, numerical tests were accompanied by novel experimental measurements of 3D printed material samples and parts to validate the method in an engineering scenario.

The applicability of MsFEM was demonstrated on linear problems of steady-state flow in heterogeneous media, elasticity, and free vibrations of objects made of heterogeneous, anisotropic material with mesostructure with voids. Number of degrees of freedom was reduced even by four orders of magnitude compared to standard finite element models without introducing a significant additional approximation error as demonstrated in a few examples. Moreover, a new way of building multiscale basis functions using B-splines was shown that it outperforms original MsFEM. The additional error can be reduced by increasing the order of the B-spline used. When using the method with the iterative corrector scheme, it was shown that proposed approach with higher-order functions gives a new possibility of reaching desired accuracy faster with a large reduction of the necessary number of degrees of freedom. In case of modeling 3D printed elements, the multiscale solutions correlate well with experimental tests for both static and dynamic, yielding a 2-5% difference of the experiment and higher-order MsFEM results.

Keywords: *multiscale finite element method, higher-order shape functions, composite structures, extrusion 3D printing testing*

Acknowledgments

I want to express my sincere gratitude to my supervisors Professor Witold Cecot for his support and encouragement throughout this research. I am also grateful to my parents for their support and scientific insight.

This work was supported by the scholarship under Grant No. 2017/25/B/ST8/02752, funded by National Science Centre.

Contents

Chapter 1

Introduction

1.1 Challenges and motivation

All materials have a multiscale structure. Since appropriately designed fine-scale characteristics allow for the achievement of material properties needed for challenging tasks of modern engineering, synthetic composites and metamaterials receive increasing attention. Composites are created by mixing two or more constituent materials, usually in the form of bonded layers or as a dispersed phase made of particles or fibers introduced into a matrix phase. Meanwhile, the macroscopic properties of metamaterials are defined by mesoscopic structures of repeating truss-like patterns. Furthermore, progress in the field of advanced materials was possible due to the novel production techniques, e.g., additive manufacturing (AM), commonly called 3D printing, that are capable of rearranging a base material in an assemble that is hardly possible to obtain by traditional manufacturing, creating optimal mesostructures that strengthen particularly vulnerable sections of manufactured parts.

During the design process of advanced materials and parts manufactured with them, numerical simulations are widely used. They allow designers to reduce the cost of experimental testing and accelerate the process. In order to reproduce quantities of interest on a coarse scale, it is necessary to take into consideration certain features of the microscale when modeling. However, the direct numerical solutions of such multiscale problems is a great challenge. The main difficulty arises from complexity introduced by finer scales. For the conventional numerical methods like the finite element method (FEM), it leads to a large number of degrees of freedom (DoFs). Since one problem may need to be recalculated many times, e.g., in optimization process, the global numerical simulation may become impractical. Thus, the need emerges to develop multiscale methods capable of capturing small-scale details in simulation of macro-scale parts and still being computationally feasible.

The main purpose of any multiscale method is to significantly reduce the size of the problem and the cost of a numerical simulation. It is done by establishing a relationship between micro-scale characteristics and macro-scale properties. A variety of multiscale methods can be derived depending on a problem properties like scale separability or periodicity. When a multiscale problem is formulated by a partial differential equation with fast varying coefficients, one possible method is to introduce coarse-scale special basis functions that capture the microscale details and then use them to find the solution. This upscaling technique is called the multiscale finite element method (MsFEM) and is the central topic of this dissertation.

The main goal of this work was to investigate and enhance the MsFEM capabilities

of modeling the mechanical behavior of advanced materials. During the course of the research, certain original modifications to the method were proposed and numerically tested to confirm its accuracy and efficiency. They are: a utilization of the higher-order B-splines as a new way of building the MsFEM basis functions; an anisotropic higher-order coarse-scale approximation, and novel shape functions that take into account the boundary conditions in problems of beams and plates. Moreover, an adaptation of MsFEM was proposed for modeling the mechanical behavior of 3D printed elements. Numerical tests were accompanied by novel experimental measurements of 3D printed material samples and parts to validate the method in an engineering scenario.

In the scope of the dissertation, linear problems were considered. The range of solved and tested problems includes the steady-state flow, as well as statics and free vibrations of elastic bodies. The parts tested experimentally were manufactured using a material extrusion technique and acrylonitrile butadiene styrene (ABS) was chosen as the base material.

1.2 Outline of the dissertation

This is a paper-based dissertation. It consists of five chapters that are preceded by the acknowledgments and the table of contents. This section ends the introductory chapter, including the motivation and aim of the research, as well as the structure of the dissertation.

Chapter 2 presents a literature overview on the topic of multiscale modeling of heterogeneous materials. Three fundamental multiscale approaches, i.e. the asymptotic homogenization and representative volume element method, as well as the multiscale finite element method, are presented briefly with their advantages and limitations. The section about MsFEM is further expanded upon the original modifications to the method proposed in recent publications.

Chapter 3 consists of the full texts of the following four papers constituting the doctoral thesis:

Article 1 M. Dryzek and W. Cecot. A coupling of multiscale finite element method and isogeometric analysis. *International Journal for Multiscale Computational Engineering*, 18(4):439–454, 2020. 40 points, IF = 1.591.

Article 2 M. Dryzek and W. Cecot. The iterative multiscale finite element method for sandwich beams and plates. *International Journal for Numerical Methods in Engineering*, 122:6714–6735, 2021. 200 points, IF = 3.477.

Article 3 M. Dryzek and E. Dryzek. Positron annihilation lifetime spectroscopy of ABS objects manufactured by fused deposition modelling. *Acta Physica Polonica A*, 132(5):1506-1508 , 2017. 40 points, IF = 0.577.

Article 4 M. Dryzek, W. Cecot, and M. Tekieli. Experimental and multiscale computational static and dynamic study of 3D printed elements with mesostructure. *Finite Elements in Analysis and Design*, 215:103876, 2023. 100 points, IF = 2.618.

The first article presents the idea and its realization in numerical tests of utilizing the higher-order B-splines as a new way of building the MsFEM basis functions. The second article explores the possibility of modeling sandwich beams and plates with complex lattice layers using MsFEM. The anisotropic higher-order coarse-scale approximation and

the novel shape functions that take into account the boundary conditions are introduced into the method in the iterative corrector scheme. The third and forth papers present experimental analysis of 3D printed material as well as an adaptation of MsFEM using a three-scale approach and the higher-order approximation for the prediction of mechanical behavior of 3D printed parts with complex mesostructure.

Chapter 4 consists of supplementary materials not presented in the articles and the results of additional numerical experiments conducted during the course of the research.

Chapter 5 includes conclusions, final remarks, and prospects of future work.

The structure of the dissertation ends with a bibliography containing references to the literature cited in the presented work, a list of figures, and a summary written in Polish.

Chapter 2

Literature overview

Many multiscale numerical methods have been developed and presented in the literature. These methods can be divided, after Fish [15], into two categories: information-passing or concurrent.

In the information-passing multiscale methods, the fine-scale details are idealized in a small volume of material, and their averaged response is embedded into the coarse scale. Coefficients of coarse-scale equations are computed by solving an auxiliary problems in small domain. Special features of the fine-scale problem, such as scale separation and periodicity, are usually taken advantage of. Mathematically-based asymptotic homogenization or physically-based representative volume element (RVE) approach belong to this category. MsFEM also belongs to this category of methods [11].

In the concurrent methods, the coarse-scale equations are not formulated explicitly, but are implied from the equations on the fine scale. Fine-scale information is simultaneously evaluated in different portions of the problem domain and has to be carried out throughout the whole simulation. The notable example in this category is the finite element squared method [14, 20, 46]. Another approach is Cellular Automata Finite Element (CAFE) were problem is resolved in parallel scales using FEM at macro scale and Cellular Automata at micro scale [39, 40].

A brief introduction to the asymptotic homogenization, the RVE method, and the MsFEM upscaling are presented to give the reader a coherent view through the whole dissertation. To illustrate each method, a problem of the steady-state flow in an isotropic heterogeneous material will be considered:

$$-\nabla \cdot (k(\boldsymbol{x}) \nabla u) = f(\boldsymbol{x}), \text{ in } \Omega, \tag{2.1}$$

$$u \text{ subjected to appropriate boundary conditions,} \tag{2.2}$$

where $k(\boldsymbol{x})$ denotes the material parameter that, in the case of steady-state flow, represents permeability.

2.1 Asymptotic homogenization

Asymptotic homogenization is a well-known mathematical technique that exploits distinct scale separation and the periodicity of microstructures to obtain the homogenized solution. Let l and L denote the characteristic size at the microscale and the macroscale, respectively. Their ratio

$$\varepsilon = \frac{l}{L} \ll 1, \tag{2.3}$$

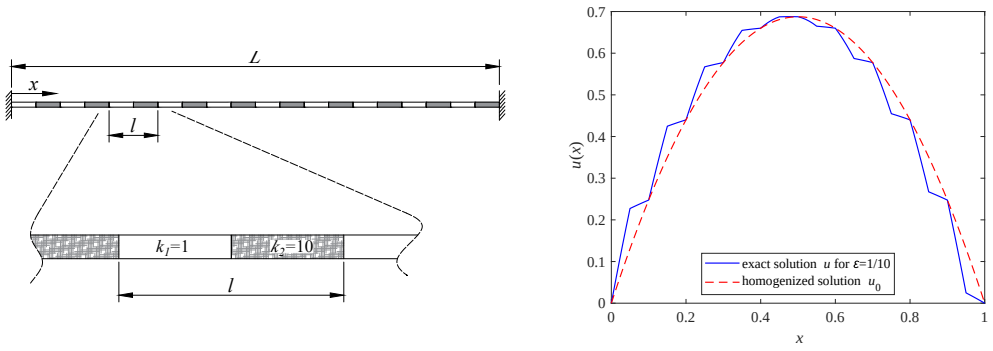

(a) (b)

Figure 2.1: 1D example: material distribution and a unit cell (a). The exact solution and homogenized solution (b).

is a parameter that describes the separability of the scales. If $k(\boldsymbol{x})$ is periodic with a period of order ε, it is called the rapidly oscillating coefficient and unknown function u can be formally represented by a regular expansion in the power series of ε:

$$u = u_0 + \varepsilon u_1 + \varepsilon^2 u_2 + \dots, \tag{2.4}$$

which converges to the homogenized solution u_0 as $\varepsilon \to 0$. The homogenized solution u_0 can be evaluated as the solution of

$$-\hbar \triangle u_0 = f(\boldsymbol{x}), \text{ in } \Omega, \tag{2.5}$$

$$u_0 \text{ subjected to appropriate boundary conditions} \tag{2.6}$$

where $\triangle(\bullet) = \nabla \cdot \nabla(\bullet)$ and $\hbar$ is called the effective coefficient that describes the macroscopic properties of the heterogeneous medium and is a constant. $\hbar$ is defined by an integral of an auxiliary function that is a solution to a problem defined in a periodic (unit) cell with boundary conditions that reflect periodicity assumptions. A comparison between the exact solution and the homogenized solution to a 1D exemplary two-phase problem is presented in Fig. 2.1. The problem reads:

$$-\frac{\mathrm{d}}{\mathrm{d}x}\left(k\left(x\right)\frac{\mathrm{d}u}{\mathrm{d}x}\right) = 1, \text{for } x \in (0, L) \setminus \{x_i\}, \tag{2.7}$$

$$u(0) = 0, \quad u(L) = 0, \tag{2.8}$$

where $k(x) = 5.5 - 4.5\,\mathrm{sgn}\left(\sin\frac{2\pi x}{l}\right)$, $L = 1$, and $l = 0.1$ and the resulting $\hbar = \frac{2}{11}$. For the regularity requirement, the natural jump conditions across the phase interfaces x_i are given as:

$$u^+(x_i) = u^-(x_i), \tag{2.9}$$

$$k(x_i)^+ \frac{\mathrm{d}}{\mathrm{d}x}u^+(x_i) = k(x_i)^- \frac{\mathrm{d}}{\mathrm{d}x}u^-(x_i). \tag{2.10}$$

where $x_i = il$ for $i = 1$ to $\frac{L}{2l} - 1$.

Mathematical homogenization theory dates back to the French school [2] and provides a theoretical background for multiscale methods. The asymptotic homogenization method is restricted to problems with periodic coefficients and scale separation. Later developments generalized the method for spatially homogeneous random media and nonperiodic materials [45].

2.2 Representative volume element

A physically-based approach to multiscale problem can be derived assuming that there exist a finite volume of the material whose behavior represents that of the bulk of the material. This small volume is called the representative volume element. Information gathered from the RVE is used to define the model parameters assumed on a coarse scale. In the considered problem (2.1) the RVE is used to identify permeability of the homogenized medium on a coarse scale. For the characterization of the permeability properties of the medium, a constitutive relationship between flux $\boldsymbol{q}$ and the gradient of u will be assumed:

$$\begin{bmatrix} q_x \\ q_y \\ q_z \end{bmatrix} = - \begin{bmatrix} \hbar_{11} & \hbar_{12} & \hbar_{13} \\ \hbar_{21} & \hbar_{22} & \hbar_{23} \\ \hbar_{31} & \hbar_{32} & \hbar_{33} \end{bmatrix} \begin{bmatrix} \dfrac{\partial u}{\partial x} \\ \dfrac{\partial u}{\partial y} \\ \dfrac{\partial u}{\partial z} \end{bmatrix}, \tag{2.11}$$

where $\hbar_{ij}$ $(i, j = 1, 2, 3)$ are effective coefficients that are to be identified.

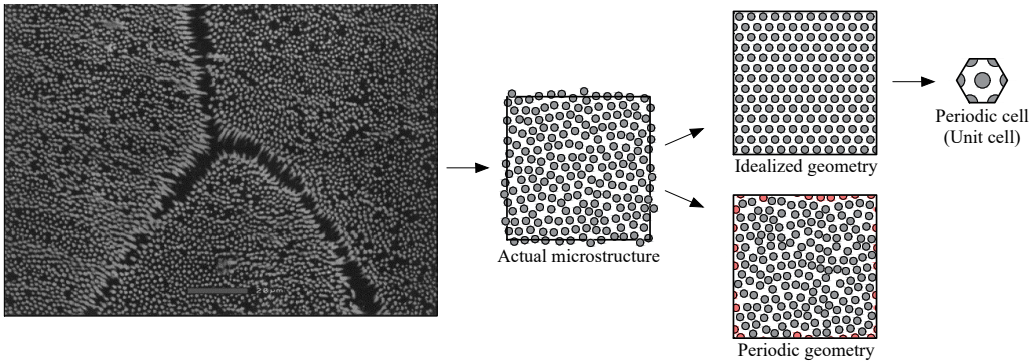

Figure 2.2: Examples of RVEs in unidirectional fiber composite based on micrograph of a metal matrix composite $NiAl_2$–Cr [51].

The first step in the multiscale modeling using RVE is to select the representative part of the microstructure. The ideal situation would be to select the region as large as possible so that as much information about heterogeneity can be retained. However, some reasonable simplification must be made to limit the size of the RVE. In case of periodicity, simply periodic cell is sufficient to represent the material. In case of a microstructure with random distribution, some idealization must be performed. The possible options for RVEs are to assume periodicity and idealize the geometry or to keep randomness within the microstructure and manipulate the fiber location at the boundary so that the geometry is periodic (see Fig. 2.2). In general, the choice of RVE regions has a small influence on macroscopic properties, however, it is relevant when evaluating the microscopic variables e.g. stresses [51].

To evaluate effective coefficients, one needs to conduct a series of tests by solving boundary value problems in the RVE imposing different boundary conditions. In the simplest case, it is done by imposing Dirichlet boundary conditions implied by constant

unit values of the gradient of u:

$$\nabla u^{(1)} = \begin{bmatrix} \dfrac{\partial u}{\partial x} \\ \dfrac{\partial u}{\partial y} \\ \dfrac{\partial u}{\partial z} \end{bmatrix} = \begin{bmatrix} 1 \\ 0 \\ 0 \end{bmatrix}, \quad \nabla u^{(2)} = \begin{bmatrix} 0 \\ 1 \\ 0 \end{bmatrix}, \quad \text{and } \nabla u^{(3)} = \begin{bmatrix} 0 \\ 0 \\ 1 \end{bmatrix} \tag{2.12}$$

as the three test cases. From the analysis of the problem (2.1) in RVE with these boundary conditions, one computes the average fluxes: $\boldsymbol{q}^{(1)}$, $\boldsymbol{q}^{(2)}$, and $\boldsymbol{q}^{(3)}$, respectively. Inserting these results in Eq. (2.11) it is easy to obtain the effective coefficients. If the boundary value problems are solved numerically, this analysis is called numerical material testing. The analogy can be found to physical testing, i.e. tensile strength testing. Different types of boundary conditions can be imposed on RVE i.e. Dirichlet, Neumann, or periodic ones. The latter yields the best results even for small RVEs [48, 51].

Given a wide range of multiscale problems in modern sciences and engineering, the use of RVEs has become a popular means of analysis, as can be found at many conferences, academic papers, and textbooks [35]. With the assumption of scale separation, numerical tests on RVE can be easily applied to identify parameters of nonlinear constitutive relations, as well [50]. Moreover, it is possible not to assume any constitutive relation on a coarse scale and compute the macroscopic stress tensor at every necessary point (e.g. Gaussian abscissas) by solving boundary value problems in RVE. This multi-scale computational homogenization [20] was later called finite element squared method (FE^2).

2.3 The multiscale finite element method

In MsFEM two meshes are employed. Let $\mathcal{T}_H$ be a partition of Ω into finite elements of characteristic size H. This is a coarse grid of macroelements K that usually do not fit to the heterogeneity of the material. Each macroelement is then refined with a mesh of much smaller characteristic size h, called a fine grid, fitted to the fine-scale details that is illustrated in Fig. 2.3.

The introduction to the method will be presented after [42], starting with a decomposition of the solution u:

$$u = u_a + u_b. \tag{2.13}$$

The first component u_a satisfies the homogeneous differential equation:

$$-\nabla \cdot (k(\boldsymbol{x}) \nabla u_a) = 0, \text{ in } K, \tag{2.14}$$

$$u_a = u|_{\partial K}, \text{ on } \partial K. \tag{2.15}$$

The second component, u_b, also referred to as a 'bubble' part of the solution u, satisfies the following non-homogeneous equation in the macroelement domain K:

$$-\nabla \cdot (k(\boldsymbol{x}) \nabla u_b) = f, \text{ in } K, \tag{2.16}$$

$$u_b = 0, \text{ on } \partial K. \tag{2.17}$$

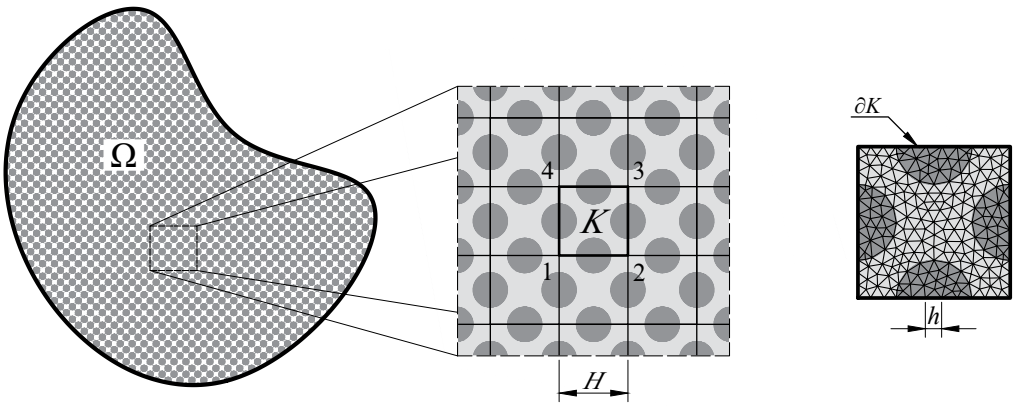

Figure 2.3: MsFEM coarse grid and fine mesh in macroelement K. Shades of gray represent different permeability values.

These two components are $k(\boldsymbol{x})$-orthogonal, i.e. they satisfy $\int_K \nabla u_b \cdot k(\boldsymbol{x}) \nabla u_a \mathrm{d}\Omega = 0$. Since by using Green's first identity as well as properties of u_a and u_b:

$$\int_K \nabla u_b \cdot k(\boldsymbol{x}) \nabla u_a \mathrm{d}\Omega = -\int_K u_b \nabla \cdot (k(\boldsymbol{x}) \nabla u_b) \,\mathrm{d}\Omega + \int_{\partial K} u_b \left(k(\boldsymbol{x}) \nabla u_a \cdot \boldsymbol{n}\right) \mathrm{d}S = 0, \tag{2.18}$$

where $\boldsymbol{n}$ is the outward pointing unit normal to the boundary ∂K.

Since the Dirichlet boundary condition in Eq. (2.15) is missing (u is not known), an iterative schema described in Sect. 2.3.3 is used or Eq. (2.15) is modified in order to define multiscale basis functions $\phi_i \in H_0^1(\Omega)$ in macroelement K as a solution to the following problem:

$$-\nabla \cdot (k(\boldsymbol{x}) \nabla \phi_i) = 0, \text{ in } K, \tag{2.19}$$

$$\phi_i = N_i, \text{ on } \partial K, \tag{2.20}$$

where N_i denotes the standard finite element shape functions on the coarse grid ($i = 1, 2, \ldots, M$, where M is the number of coarse DoFs). Sometimes, N_i is not used directly on ∂K but after certain modifications or for larger domain by the oversampling method what is described later in this section.

The multiscale basis functions are used in the standard finite element scheme of finding an approximation $u^H = \sum_{i=1}^{M} \alpha_i \phi_i \in V^H = \mathrm{span}\{\phi_i(\boldsymbol{x})\} \subset H_0^1(\Omega)$:

$$B(u^H, \phi_i(\boldsymbol{x})) = L(\phi_i(\boldsymbol{x})), \;\; i = 1, 2, \ldots, M, \tag{2.21}$$

where for the considered exemplary problem

$$B(u, v) = \int_\Omega \nabla u \cdot k(\boldsymbol{x}) \nabla v \mathrm{d}\Omega, \quad L(v) = \int_\Omega f v \mathrm{d}\Omega. \tag{2.22}$$

Finally, multiscale solution u_{ms} is obtained as the sum of u^H and the bubble part u_b [27]:

$$u_{ms} = u^H + u_b. \tag{2.23}$$

In practice, problem (2.19)-(2.20) is solved numerically on a fine mesh for each macroelement K individually, unless the considered domain is periodic. The values of

the fine mesh DoFs for each multiscale shape function ϕ_i^K for element K are stored in matrix $\boldsymbol{P} = (p_{ij})$ that is called the prolongation matrix. This ϕ_i^K can be expressed in the following way:

$$\phi_i^K = p_{ij}\phi_j^h, \tag{2.24}$$

where ϕ_j^h are basis functions of the fine grid. To calculate entries of a K-element stiffness matrix k_{ij}, the trail u and the test v functions in (2.22) are substituted with multiscale shape functions ϕ_i^K and ϕ_j^K expressed by formula (2.24):

$$k_{ij} = \int_K \nabla\phi_i^K \cdot k(\boldsymbol{x})\nabla\phi_j^K \mathrm{d}\Omega = p_{il}\, p_{jm} \int_K \nabla\phi_l^h \cdot k(\boldsymbol{x})\nabla\phi_m^h \mathrm{d}\Omega. \tag{2.25}$$

Assuming the assembled over coarse element domain fine-mesh stiffness matrix $\boldsymbol{K}^h = (k_{lm}^h)$, where $k_{lm}^h = \int_K \nabla\phi_l^h \cdot k(\boldsymbol{x})\nabla\phi_m^h \mathrm{d}\Omega$, the coarse grid stiffness matrix can be computed using the following matrix formula:

$$\boldsymbol{K}^H = \boldsymbol{P}^T \boldsymbol{K}^h \boldsymbol{P}. \tag{2.26}$$

Similarly, the loading vector for element K is evaluated by the following formula:

$$\boldsymbol{f}^H = \boldsymbol{P}^T \boldsymbol{f}^h, \tag{2.27}$$

where $\boldsymbol{f}^h$ is the fine mesh loading vector assembled over the coarse element domain and it equals to $f_l^h = \int_K f\phi_l^h \mathrm{d}\Omega$.

MsFEM consists of two steps: numerical evaluation of the multiscale basis functions and coarse-grid analysis on these functions. The basis functions are built using the boundary value problem that contains information about the fine scale distribution of coefficient $k(\boldsymbol{x})$. The global formulation uses these basis functions to provide an approximation of the solution enhanced with the fine-scale heterogeneous features.

The idea of using basis functions that satisfy the differential equation is not new and can be traced back to a pioneering article by Babuška et al. [1] on the problem of unidirectional composite materials. Generalization of this idea for all types of composite materials and porous media was introduced by Hou and Wu in paper [25] where the method got its name. MsFEM is closely related to the variational multiscale method (VMS) [29, 30]. Both methods yield same results, provided that the right-hand side is treated the same in both methods [15] (consider problem (2.16)-(2.17) and Eq. (2.23)). Moreover, a parallel can be drawn between MsFEM and the multigrid method [16, 17]. The same numerical techniques are utilized in both methods, e.g., prolongation.

Originally, MsFEM was developed to effectively solve problems of flow in highly heterogeneous porous media utilized in high-fidelity reservoir simulations [49]. A framework for non-linear problems of flow was later presented in [10]. More recently, the method was modified to solve problems of elasticity of composites and metamaterials in [56], where it was called the extended multiscale finite element method. Several other engineering problems were modeled using MsFEM, including beam and plate problems [57], viscoelastic asphalt concrete [31, 33], heterogeneous piezoelectric composites [18], and regional soil subsidence [52].

The primary benefit of MsFEM over the other multiscale methods is the absence of assumptions about periodicity and scale separation. Moreover, macroelements are not limited to standard elements. They can have arbitrary shapes even with curved edges or faces [55, 44]. From a technical perspective, the multiscale shape functions are calculated numerically on a fine grid for each macrolement independently that allows for parallel computing. If the material is periodic and the coarse elements fit the periodicity, then

the shape functions can be reused leading to further cost reductions. It is also worth noting, that by using Galerkin coarsening (Eq. (2.26) and (2.27)) no integration is needed to obtain the matrices at the coarse level.

The main difficulty of the method is to choose appropriate boundary conditions that determine multiscale basis functions in Eq. (2.20). For example, N_i can simply be chosen to be linear on the boundaries of the macroelement. However, this approach neglects fine-scale oscillations of the true multiscale solution at the macroelement interfaces. This can lead to large errors, caused by resonance effects that was identified for the first time in [28] and is a recurring theme in studies about MsFEM. This effect typically occurs when the macroelement size H and the parameter ε that characterizes the small scale of the problem are of the same order. The following subsections present possible strategies to mitigate this effect and generally improve the MsFEM solution.

2.3.1 Oscillatory boundary conditions

A good choice of boundary conditions can significantly improve the accuracy of the multiscale method, as has been proven theoretically using an asymptotic expansion in [25, 28]. In this subsection, typical methods of generating boundary condition in problem (2.19)-(2.20) that account for fine-scale details will be recalled.

The first intuitive approach to oscillate the boundary conditions in 2D problems is to consider a reduced problem on each edge of ∂K [25]. The reduced problem is obtained from Eq. (2.19) by removing the partial derivative in the direction normal to the given macroelement edge (after transferring the equations to the master element). For example, consider the macroelement K presented in Fig. 2.3 which edge $\Gamma_{12} \subset \partial K$ between nodes 1 and 2 is perpendicular to the direction y. For this edge, the reduced problem reads:

$$\frac{\partial}{\partial x} k(\boldsymbol{x}) \frac{\partial N_i}{\partial x} = 0 \tag{2.28}$$

The boundary conditions for this two-point problem are given by $N_i(\boldsymbol{x}_j) = \delta_{ij}$ for $i, j = 1, 2$, where $\boldsymbol{x}_j$ are the coordinates of the nodes j and δ is the Kronecker delta. In the 3D case this approach is performed in two steps: first solving the 1D problems of type (2.28) along each edge, then imposing the solutions as a boundary condition to the 2D reduced problem on each macroelement face. A detailed description of each problem can be found in [6, 32].

The next approach was suggested in [28] after thorough discrete error analysis of MsFEM. It was observed that by imposing artificial boundary conditions in problem (2.19)-(2.20) the resulting multiscale solution exhibits a boundary layer near ∂K that is the main source of the resonance effect. This layer, however, is thin; thus raises the idea of exploiting this by reformulating the problem of multiscale basis function to a larger region and using only the interior information to construct the functions. The technique was called oversampling and can be implemented in the following way: consider larger domain K' with the corresponding nodes $(1', 2', 3', 4')$ that covers the quadrilateral macroelement K as illustrated in Fig. 2.4a. Temporary shape functions ψ_j^K will be calculated for each node, using equations (2.19) in domain K' with boundary conditions on $\partial K'$ defined on each edge as a linear function that takes values 1 in j-th node and 0 in the remaining ones (see example in Fig. 2.4b). The modified shape function ϕ_i^K of the macroelement K is going to be calculated as a linear combination of the temporary shape functions:

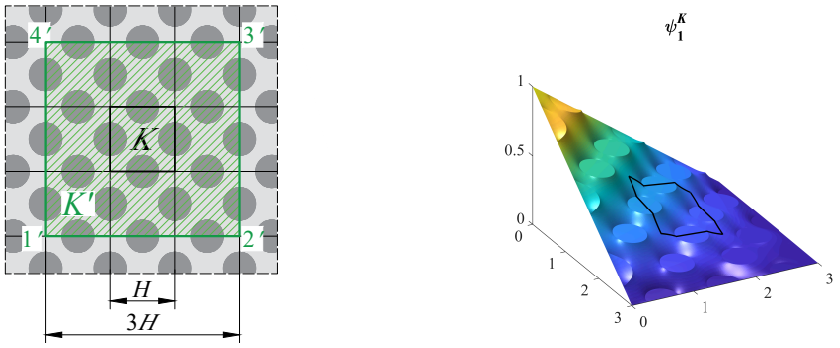

(a) (b)

Figure 2.4: Oversampling domain of size $3H \times 3H$ in green (a) and temporary shape function ψ_1^K with outline of a solution on ∂K (b).

$$\phi_i^K = \sum_{j=1}^{4} c_{ij}\psi_j^K, \; i = 1, \ldots, 4, \tag{2.29}$$

where c_{ij} are constants determined by solving the set of 4×4 linear equations $\phi_i^K(\boldsymbol{x}_j) = \delta_{ij}$, where $\boldsymbol{x}_j$ denote coordinates of the macroelement nodes (for $i, j = 1, 2, 3, 4$). The best size of K' was numerically estimated in [54] to be $3H \times 3H$. This approach indeed mitigates the resonance effect; however, it results in non-conforming approximation with discontinuities along macroelement edges ∂K. The error of non-conformity was estimated to be small in [12]. Although oversampling can be simply translated to 3D macroelements, a special oversampling technique for this case was proposed in [53]. An improvement of the technique was presented in [27] where oversampling is used for each macroelement edge separately to obtain boundary conditions to calculate optimal multiscale basis functions.

The third technique was inspired by the RVE method. The authors of [54, 55] proposed to utilize periodic boundary conditions in the problem of multiscale basis functions. To illustrate it, consider the 2D rectangular macroelement K aligned with x and y axis (Fig. 2.3). To calculate the multiscale shape function ϕ_1^K associated with node 1, the following constraints are applied to individual edges:

$$N_1|_{\Gamma 12} = N_1|_{\Gamma 43} + \Delta x, \text{ on } \Gamma_{12}, \tag{2.30}$$

$$N_1|_{\Gamma 14} = N_1|_{\Gamma 23} + \Delta y, \text{ on } \Gamma_{12}, \tag{2.31}$$

where Δx and Δy are linear functions that take values 1 at node 1, and 0 at nodes 2, 3, and 4. This technique can be further expanded in the vector problem of elasticity where the values of Δx and Δy can be oscillated using the oversampling technique.

2.3.2 Higher-order approximation

In problem (2.19)-(2.20), N_i can be any function that provides conforming multiscale functions. Thus, rises the idea of enriching multiscale function space in a manner similar to the p-refinement in the standard FEM. To construct multiscale basis functions, N_i functions were defined using higher-order shape functions of Lagrange [19], hierarchical [36] or Crouzeix-Raviart [7] type. Multi-node macroelements were introduced in [4, 5] that are created by adding nodes along the edges and inside the elements. This approach

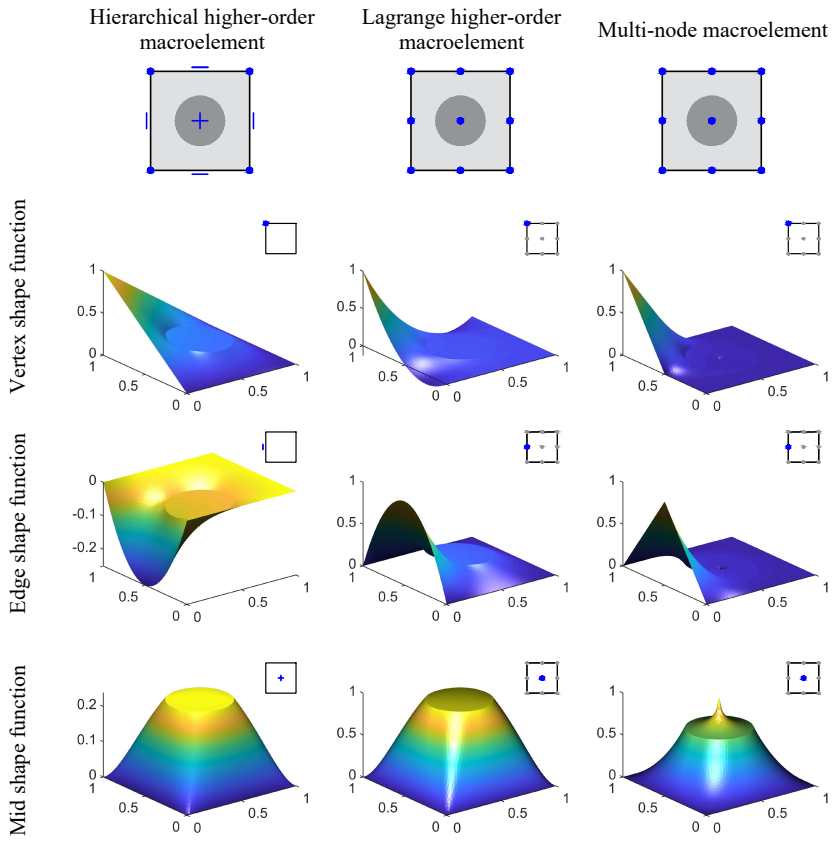

Figure 2.5: Multiscale shape functions types for hierarchical [6], Lagrange [19], and multi-node macroelements [4] (for detail definitions refer to the cited articles).

was also combined with the oversampling technique, e.g., in [38]. Higher-order boundary conditions were also oscillated using reduced problems along edges in [6]. The increase of DoFs on a fixed coarse grid was studied in the context of adaptivity [43, 31] and topology optimization [37].

The new multiscale shape functions can be divided into vertex, edge, and mid types, as illustrated in Fig. 2.5 for three function families. Vertex or edge types shape functions are generated using Eq. (2.19)-(2.20). To create the mid functions of hierarchical and Lagrange type, with zero Dirichlet boundary condition, problem (2.19)-(2.20) has to be modified by introducing the source term on the right-hand side, after [47]:

$$-\nabla\cdot\left(k(\boldsymbol{x})\nabla\phi_i^K\right) = \triangle N_i^K, \text{ in } K, \tag{2.32}$$

$$\phi_i^K = 0, \text{ on } \partial K, \tag{2.33}$$

where N_i^K is the bubble function of higher-order type in macroelement K. Moreover, the Lagrange shape factions should be normalized.

In case of multi-node macroelements [4], each shape function in this approach can be interpreted as the field obtained by imposing unit values at each of the coarse scale DoF while all others are set to zero. The mid shape functions are generated using Eq. (2.19)-(2.20) and value 1 of a selected fine-scale DoF. However, one should note that for 2D and 3D second order problems pointwise conditions are ill-posed. Probably this is the reason of almost singular behavior of the mid shape functions.

It is worth noticing, that at a discrete fine-scale level this approach of decreasing of DoFs number in MsFEM resemble the superelement constructed by the static condensation technique [23]. By using a static condensation on a single macroelement, a dependency relations between fine-mesh interior DoFs and DoFs on the macroelement boundary can be formulated, and the interior DoFs can be eliminated out of the global system. What is left is a macroelement with DoFs only on edges, which is referred to as superelement. In contrast, MsFEM reduces even more DoFs; however, it does not fully resolve the fine-mesh solution. The way of model order reduction using superelements is commercially successful and can be found in many FEM programs, e.g., [13, 21].

2.3.3 Iterative correction

To improve the accuracy of local boundary conditions (2.20), information of the global solution u_{ms} can be used. This approach creates an iterative loop of using the current solution to correct basis functions to obtain a new solution that can be used for a new correction, and so on. First, it was used to iteratively modify multiscale basis obtained by the oversampling technique to smooth the solution and obtain a conforming (continuous) solution [9, 8]. Similarly, the multigrid algorithm, e.g, two-grid cycle scheme in the multigrid terminology [24, 26], has been applied to converge the MsFEM solution to the fine-scale numerical solution.

Iterative methods will be illustrated with a recently developed residual-driven local iterative technique in [42, 41], where core idea is to correct individual multiscale basis functions. Let us assume that MsFEM solution u_{ms} was calculated using a standard bilinear multiscale nodal basis. Using this solution, it is possible to rewrite original Eq. (2.1) to calculate the right-hand sides in domains $\widetilde{K}_i$ that are the supports of multiscale basis functions ϕ_i (patches of several macroelements):

$$f_{ms} = - \bigtriangledown \cdot (k(\boldsymbol{x}) \bigtriangledown u_{ms}), \text{ in } \widetilde{K}_i, \ i = 1, 2, \ldots, M, \tag{2.34}$$

where M is the number of coarse DoFs. Note that the right-hand sides are marked with ms index and typically differ from the right-hand side of the original problem. The exact solution u in $\widetilde{K}_i$ is the sum of the multiscale solution and some unknown term u_c, a local corrector:

$$u = u_{ms} + u_c. \tag{2.35}$$

By linearity of the problem, u_c satisfies the following residuum-driven problem:

$$- \bigtriangledown \cdot (k(\boldsymbol{x}) \bigtriangledown u_c) = f - f_{ms}, \text{ in } \widetilde{K}_i, \tag{2.36}$$

$$u_c = (u - u_{ms})|_{\partial \widetilde{K}_i}, \text{ on } \partial \widetilde{K}_i. \tag{2.37}$$

In order to localize each correction, u_c takes value 0 on boundary $\partial \widetilde{K}_i$. As a result, this problem is only driven by the residuum of the approximate solution and can be solved on a fine grid. u_c is later combined with ϕ_i to create a new corrected multiscale basis function. After correcting all the multiscale basis functions, a new multiscale solution can be obtained. This concept was theoretically and numerically proven to converge to the best possible fine-mesh accuracy. The corrector term is an approximation of the error and is computed similarly to the implicit error estimation method [22]. In MsFEM, the subdomains consist of the macroelement patches.

Chapter 3

Full texts of the articles constituting the doctoral thesis

This chapter presents the full texts of four research articles indexed in the Journal Citation Reports (JCR) database constituting the submitted doctoral thesis. Each paper is attached in the following sections with the bibliographic information with the number of points assigned by the Polish Department of Education to the journal in which the specific article is published and the Impact Factor assigned to the journal[1].

This set of articles presents investigation on the topic of MsFEM capabilities of modeling the mechanical behavior and properties of advanced materials. The research consist of certain original improvements of the method, numerous numerical examples of modeling of composites and materials with lattice microstructure, and experimental measurements of 3D printed samples that were used to validate the numerical method.

Article 1 (page 25) introduces the higher-order spline approximation in MsFEM methodology. The idea of B-splines spanned on several macroelements as a basis for building multiscale trail and test functions was examined. To compute the new multiscale basis function a source term on the right-hand side is introduced as in Eq. (2.32)-(2.33). However, in contrast to standard MsFEM where the shape functions are evaluated macroelement by macroelement, in this approach the basis functions are computed at once at theirs whole supports . Modified MsFEM with the new basis functions was tested on selected numerical experiments on problems of flow in porous media with periodic and random material properties distribution. The modified method indeed improves standard MsFEM for fast oscillating material properties even though resonance effect was observed when the ratio of inclusion size and coarse mesh size approaches one ($\varepsilon/H \to 1$). However, for some examples, it could be reduced by increasing the order of B-splines.

In Article 2 (page 43), an adaptation of MsFEM to the analysis of sandwich beams and plates with complex lattice layers was proposed. In these problems, one geometric dimension (thickness) is much smaller compared with the others, thus only one layer of macroelements can be used. Furthermore, the boundary conditions on the top and bottom edges (or faces) are often zero traction. This allows for significant reduction of DoFs and introduction of approximation exclusively in the direction of beam axis or plate mid plane. The novel higher-order multiscale shape functions that take into account the microscale boundary conditions were introduced. Additionally, the local iterative corrector scheme (see Sect. 2.3.3) adapted for the bending-dominated responses

[1] Values of the current point score in lists of journals of the Ministry of Science and Higher Education in Poland and Impact Factor as of October 31, 2022.

of sandwich structures provides converges of the coarse mesh approximation to the best possible fine-mesh solution. Several numerical examples are presented to demonstrate the capabilities of the method. The proposed modifications of the shape functions and the higher-order coarse mesh approximation increase the convergence rate. The method was validated by comparison of the numerical results with experimental ones for a sandwich panel with a dual corrugated high-density fiberboard core. Very good consistency of both results was observed.

In Article 3 (page 66), Positron Annihilation Lifetime Spectroscopy (PALS) was used to study ABS specimens manufactured using material extrusion technique. This study was conducted as a prelude to numerical multiscale modeling of 3D printing elements. It gave insight to the structure of the 3D printed material using the advance experimental measuring technique and gave the author of this thesis opportunity to familiarize with extrusion-based additive manufacturing technique. PALS is a non-destructive spectroscopic method of materials research widely used for investigation of metals, semiconductors, ceramics, polymers, and porous materials. In case of polymers, from the obtained positron lifetime spectra, information about the molecular microstructure can be derived due to the fact that ortho-positronium (a bound state of electron and positron) is a probe of local free volumes in their structure (for more details see Sect. 3.3.1). Knowing that certain features of a microstructure affect macroscopic mechanical properties a correlation between these properties and the positron annihilation parameters can be established. In the study, a set of 3D printed specimens was prepared to explore possibilities of identifying differences in molecular structure for different print configurations. Square tiles (10 mm × 10 mm) and long rectangular tiles (100 mm and 200 mm long) with all filament roads parallel to longer edge were prepared. All types of tiles were produced with various infill line distance parameter that results in different overlapping of the roads in horizontal and vertical directions. The slight increase of the ortho-positronium lifetime indicating increase of the mean free volume radius and was observed for the longest tiles for which influence of weld interface is expected to be most pronounced. This study was conducted in Institute of Nuclear Physics Polish Academy of Sciences in Cracow.

In Article 4 (page 71), numerical and experimental studies were conducted to demonstrate the applicability of MsFEM with the higher-order approximation to the prediction of mechanical behavior of 3D printed parts with complex mesostructure. Three scales are considered: the microscale, at which the filament paths are homogenized using an orthotropic material model with experimentally identified properties; the mesoscale with 3D printed structure that is upscaled by MsFEM; and the macroscale, at which the overall problem is effectively solved. To validate the approach experimental measurements of static bending and free vibrations of beams with four different mesostructures and two print orientations were conducted. The measurements were performed using digital image correlation and were compared with numerical modeling. Both results coincide very well for a number of examples. Moreover, the study revealed that the hierarchical higher-order shape functions can accurately represent free vibrations even for the high frequencies.

3.1 Article 1: A coupling of multiscale finite element method and isogeometric analysis

M. Dryzek and W. Cecot. A coupling of multiscale finite element method and isogeometric analysis. *International Journal for Multiscale Computational Engineering*, 18(4):439–454, 2020. 40 points, IF = 1.591, https://doi.org/10.1615/IntJMultCompEng.2020034287.

A Coupling of Multiscale Finite Element Method and Isogeometric Analysis

M. Dryzek[1)], W. Cecot[1)]

[1)] *Chair for Computational Engineering*
Department of Civil Engineering
Cracow University of Technology
Krakow, Poland
e-mails: mdryzek@l5.pk.edu.pl, plcecot@cyf-kr.edu.pl

Abstract

In this paper, we propose to use the B-splines spanned on several macroelements as a basis for building the Multiscale Finite Element Method (MsFEM) trail functions. The main benefit of our approach is calculation of the multiscale functions in one step on the whole support, in contrast to standard MsFEM shape functions that are evaluated coarse element by element and require a cumbersome gluing.

Selected numerical experiments for flow in porous media with periodic and random material properties distributions were performed to test our modified MsFEM with the new basis functions. We found that the method indeed improves standard MsFEM for fast oscillating material properties. We observed that the resonance effect, when the ratio of inclusion size and coarse mesh size approaches one ($\varepsilon/H \to 1$) can be reduced by increasing the order of B-splines.

Keywords: Multiscale finite element method, Higher order shape functions, B-splines

1 Introduction

The main purpose of any multiscale method is to reduce significantly the number of degrees of freedom in numerical simulation of partial differential equations with fast varying coefficients. It is done by establishing at first a relationship between microscale characteristics and macroscale properties. The most frequently used approaches to this problem are *the asymptotic homogenization*, *the representative volume element method* (including FE^2), and *the multiscale finite element method*.

The asymptotic approach makes use of the unit cell analysis followed by a solution of a boundary value problem with constant coefficients to evaluate the homogenized solution, understood as the limit of a certain sequence of functions. The method proposed by Bensoussan, Lions and Papanicolaou [1] was studied for modeling of a periodic composite. However, it reveals its limitations when applied to solve nonperiodic material problems.

The representative volume element method (RVE) uses a minimal material volume that contains sufficient information about the microstructure. The macroscale properties are determined by imposing specific boundary conditions to this representative volume and computing numerical material testes. The gathered information is later used in analysis on the macro level, facilitating the acquisition of macroscopic and microscopic stress and strain fields. A few key types of the method are:

- *numerical homogenization* - by a single RVE analysis with a constitutive law assumed a'priori (Zohdi and Wriggers [2]),
- *computational homogenization* - that is free of coarse-scale constitutive equations with RVE attributed to selected (e.g. Gauss integration, points, and material parameter tangent tensor ($\partial\sigma/\partial\epsilon$) evaluated on the fly as proposed by Geers, Kouznetzova, and Brekelmans [3], and called later by Feyel and Chaboche as FE^2 method [4]),
- *heterogeneous multiscale method* - in which the integrand (integrated function) values at Gauss points are computed on the fly by micro-cell analysis, as in the method proposed by E and Engquist [5],
- *cellular automata based approach* (CAFE) - developed by Madej, Pietrzyk, and Hodgson [6, 7], who incorporated a quite different technique at the RVE level, instead of the FEM analyses.

The RVE approach may be used if two assumptions are satisfied i.e. periodicity and scale separation.

The multiscale finite element method starts with a macroscale discretization, which is followed by the independent refinement of each coarse-scale element in order to obtain a discretization that complies with the material heterogeneity. The multiscale shape functions of the method are obtained by solution of auxiliary local problems in the macroelement domains. The MsFEM solution is then composed of the multiscale basis functions. This way, the microscale details are incorporated in the macroelement stiffness matrices (see Hou and Wu [8]).

While defining the local problem of the multiscale shape functions appropriate boundary conditions should be imposed, ideally equal to the exact solution. Since we do not know the solution in advance, we have to make certain approximations. Originally undisturbed linear functions were incorporated. Although these resulting shape functions can capture details of microstructure inside the element domains, there is a significant error on the macroelement boundaries (see Fig.1). The resonance effect occurs when the length of the scale of the microstructure approaches the coarse mesh size, on which the interelement material heterogeneity is neglected [9].

There are several techniques that can improve the result of the MsFEM calculations by introducing oscillatory boundary conditions by the auxiliary BVP. The first option was deduced from a simple observation that the error diminishes quickly across the boundary layer, thus proposition to extend the domain while building the multiscale shape functions. This approach was called oversampling and was introduced simultaneously with MsFEM by Hou et al. [8, 9]. This technique, however, results in a nonconforming MsFEM, where the macroscale basis functions are discontinuous along the edges of macroelements. Another option of reducing the resonance effect is the iterative approach presented e.g. in [10, 11]. After obtaining the solution by MsFEM the residue is used as a load for the correction of the multiscale shape functions. The new solution is obtained from the corrected function space

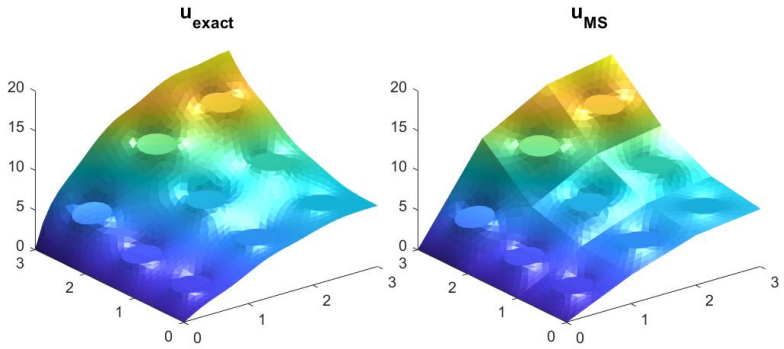

Figure 1: Solutions of an elliptic boundary value problem obtained on a fine mesh (u_{exact}) and on 3×3 coarse quadrilateral mesh using MsFEM with linear boundary conditions (u_{MS}).

and again can be corrected until the residue is small enough. Finally, the increase of the degrees of freedom, in a similar manner to p-refinement in FEM, was studied. Higher order macroscale shape functions were also used of either Lagrange [12] or hierarchic [13, 14] or Crouzeix-Raviart [15] type. Multi-point elements were introduced in [16, 17] bringing MsFEM closer to elements reduced by static condensation method. The increase of degrees of freedom was studied in the context of adaptivity [18, 19] and topology optimization [20].

Originally, the multiscale finite element method was developed to solve flow in highly heterogeneous porous media. More recently, the method was modified to solve vector problems of elasticity (the Extended Multiscale Finite Element Method, [21]) of composites and metamaterials. Several other engineering problems were modeled using MsFEM including: heterogeneous piezoelectric composite [22], 3D eddy currents in laminated media [23], and regional land subsidence [24].

In this work, we propose to utilize the higher order B-splines as a new way of building the MsFEM basis functions. Non-Uniform Rational B-Splines (NURBS) are basis functions used in Isogeometric Analysis (IGA) and the list of benefits of using them over standard FEM approximation includes improved representation of surfaces in contact problems, advantages in vibrations problems, usefulness in plate and shell problems, and most important coupling design model with the analysis model. The isogeometric analysis is widely developed by researchers around the world and coupling it with the multiscale method may also further expand its capabilities. B-splines functions are spanned on patches of several elements. Moreover, B-splines are build of polynomials of higher order with arbitrary order of continuity, thus we expect to achieve better smoothness of the MsFEM solution and there are no need fot introducing oscillations to the boundary conditions of the local problems related to the internal knots since B-splines assume zero values on the patch boundary. The proposed modifications to MsFEM can be also interpreted as a combination of standard FEM approximation on the microscale level and B-splines on the macroscale level. The FEM approximation of C^0 regularity enables the appropriate solution of heterogeneous material deformations while B-splines on the macroscale should provide an appropriate approximation of the macroscopic structure behavior.

The article is divided into 5 sections. In sections 2 we introduce the problem of flow in heterogeneous media and briefly introduce MsFEM with oversampling technique. In sections 3 we refer to the construction of B-splines basis functions and how to use them in MsFEM methodology. In section 4 we show numerical tests of our method in comparison to standard MsFEM and MsFEM with oversampling modification. Finally, in section 5, we present conclusions from this work and further research plans.

2 Problem formulation and MsFEM

We recapitulate briefly the standard MsFEM principle for the problem of a flow in heterogeneous media modeled by the an elliptic equation with highly oscillatory coefficient $a(\boldsymbol{x})$:

Find function u in domain Ω such that:

$$-\nabla \cdot (a(\boldsymbol{x})\nabla u) = f, \text{ in } \Omega, \tag{2.1}$$

$$u = \hat{u}, \text{ on } \partial\Omega^D, \tag{2.2}$$

$$a(\boldsymbol{x})\frac{\partial u}{\partial n} = t, \text{ on } \partial\Omega^N, \tag{2.3}$$

where n is the unit outward normal to $\partial\Omega^N$. We divide the domain Ω into macroelements Ω_i with corresponding nodes $(1, 2...M)$, such that $\Omega = \bigcup_i \Omega_i$, with the characteristic mesh size H. Each macroelement is meshed with a fine mesh of size h. Both discretizations are illustrated in Fig. 2 for a regular mesh. Please note, that the macroelements in general may be of arbitrary shape. Macroelement number of degrees of freedom, is denote to M on course scale and N on fine scale.

The weak form of Eq. 2.1 reads:
Find $u \in U$ in a domain Ω such that:

$$B(u, v) = L(v), \forall v \in V, \tag{2.4}$$

where

$$B(a, v) = \int_\Omega \nabla u \cdot a(\boldsymbol{x})\nabla v \mathrm{d}\Omega, \quad L(v) = \int_\Omega f v \mathrm{d}\Omega. \tag{2.5}$$

and V is the H_1 Sobolev space in this case.

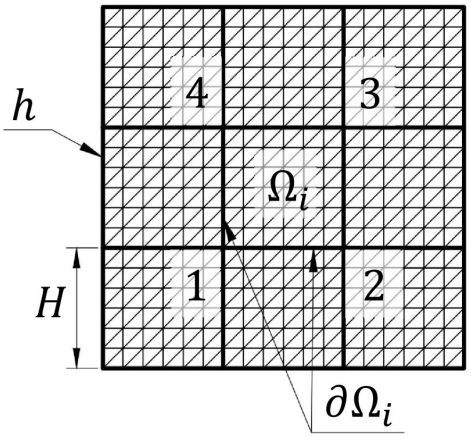

Figure 2: Discretization of the domain Ω.

2.1 The MsFEM idea

We start with the following decomposition of the solution u [11]:

$$u = u_a + u_b. \tag{2.6}$$

The first component, u_a, satisfies homogeneous differential equation on the macroelement domain Ω_i:

$$-\nabla \cdot (a(\boldsymbol{x})\nabla u_a) = 0, \text{ in } \Omega_i, \tag{2.7}$$

$$u_a = u, \text{ on } \partial\Omega_i, \tag{2.8}$$

with the Dirichlet boundary condition defined by the exact solution u. Second component, u_b (also refereed to as a 'bubble' part of the solution u), satisfies the following non-homogeneous equation on the macroelement domain Ω_i:

$$-\nabla \cdot (a(\boldsymbol{x})\nabla u_b) = f, \text{ in } \Omega_i, \tag{2.9}$$

$$u_b = 0, \text{ on } \partial\Omega_i, \tag{2.10}$$

with the zero Dirichlet boundary condition. This two components are orthogonal, i.e. they satisfy $\int_{\Omega_i} \nabla u_b \cdot a(\boldsymbol{x}) \nabla u_a \mathrm{d}\Omega = 0$. As explained in [11], from this property multiscale shape functions ϕ_j of the macroelement Ω_i are defined:

$$\begin{aligned} &-\nabla \cdot (a(\boldsymbol{x}) \nabla \phi_j) = 0, \text{ in } \Omega_i, \\ &+\text{b.c. on } \partial\Omega_i, \end{aligned} \tag{2.11}$$

for $j = 1, 2...M$, where M denotes element number of degrees of freedom (dofs). Different boundary conditions, as mentioned in section 1, can be utilized.

Now, we can establish a new global problem for solution $u^H \in V^H$:

$$B(u^H, v) = L(v), \forall v \in V^H, \tag{2.12}$$

$$V^H = \text{span}\left\{\phi_1(\boldsymbol{x}), \phi_2(\boldsymbol{x}), ...\phi_M(\boldsymbol{x})\right\}. \tag{2.13}$$

Problem (2.11) may be also interpenetrated as a definition of the prolongation operator that transfers M coarse element dofs into N fine mesh dofs. Problem (2.11) is solved numerically on the fine mesh to compose prolongation matrix $P_{N\times M}$ that is used to compute the macroelement stiffness matrix $\boldsymbol{K}^H$ and vector $\boldsymbol{f}^H$ by simple algebraic operations (the Guass coarsening):

$$\boldsymbol{K}^H = \boldsymbol{P}^T \boldsymbol{K}^h \boldsymbol{P}, \quad \boldsymbol{f}^H = \boldsymbol{P}^T \boldsymbol{f}^h, \tag{2.14}$$

where $\boldsymbol{K}^h$ and $\boldsymbol{f}^h$ are assembled on the fine mesh only on macroelement domain Ω_i. We want to stress that $\boldsymbol{K}^h$ was computed previously when solving (2.11) thus can be reused here. It is also worth noting that no integration is done to obtain the matrices on the coarse level.

We can now solve for the coarse mesh dofs $\boldsymbol{u}^H$:

$$\boldsymbol{K}_G^H \boldsymbol{u}^H = \boldsymbol{f}_G^H. \tag{2.15}$$

Knowing $\boldsymbol{u}^H$, it is easy to calculate vector of fine mesh dofs $\boldsymbol{u}^h$ element by element:

$$\boldsymbol{u}_e^h = \boldsymbol{P} \boldsymbol{u}_e^H. \tag{2.16}$$

Finally, multiscale solution $\boldsymbol{u}_{MS}$ is obtain by adding $\boldsymbol{u}^h$ with bubble part $\boldsymbol{u}_b$ which is numerical solution of problem (2.9) with its boundary conditions in each macroelement on fine mesh:

$$\boldsymbol{u}_{MS} = \boldsymbol{u}^h + \boldsymbol{u}_b. \tag{2.17}$$

2.2 Oversampling technique

We will use also the oversampling technique. Thus, after [8],let's consider larger domain Ω_i', with corresponding nodes $(1', 2', 3', 4')$ that covers macroelement as illustrated in Fig. 3. We are going to calculate temporary shape functions ψ_k, for each dof, using equations 2.11 on domain Ω_i' with linear functions on the boundary $\partial\Omega_i'$. Modified shape function ϕ_j on the domain Ω_i are going to be calculated as a linear combinations of the temporary shape functions:

$$\phi_j = \sum_{k=1}^{4} c_{jk} \psi_k, \tag{2.18}$$

where c_{jk} are constants determined by solving set of 4×4 linear equations $\phi_i(\boldsymbol{x}_j) = \delta_{ij}$, where $\boldsymbol{x}_j$ denote coordinates of macroelement vertices (for $i, j = 1, 2, 3, 4$).

It was reported in [21] that the best results are obtained using an oversampling region covering the 3×3 macroelements. For the macroelements sharing an edge with the boundary of the domain Ω only feasible oversampling size is 3×2 (2 in the direction perpendicular to the boundary).

For random coefficient a oversampling technique will generate different results on the edges of macroelements resulting from analysis in different patches. In this work, we are going to take the mean average between values of the same basic function calculated on different macroelements to provide a conforming approximation.

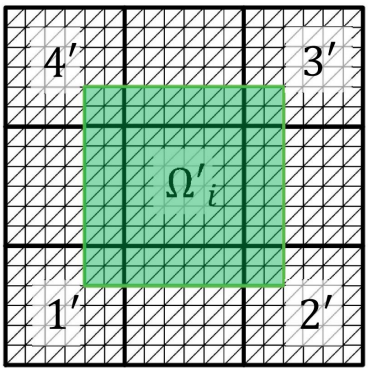

Figure 3: Oversampling domain Ω_i'.

3 B-spline basis functions

B-splines have been long used in the Computed Aided Design (CAD) systems allowing to represent complex geometries by polynomial functions. Further modifications of the functions allowed to represent exactly conic and circular sections. Only recently Hughes et al. proposed in [25] to employ the Non-Uniform Rational B-Splines in numerical analysis framework. The concept became known as the Isogeometric Analysis (IGA) and its idea is to utilize the NURBS functions as basis functions in the finite element analysis for solving partial differential equations.

B-spline functions are defined over a knot vector set $\Xi = \{\xi_1, \xi_2, ..., \xi_{n+p+1}\}$, $\xi_i \leq \xi_{i+1}$, where i is a knot, n is a number of basis functions, and p is order of basis function. B-spline basis functions of order p are defined by the Cox-de Boor recursive relations as:

$$\text{for } p = 0 \quad N_{i,0}(\xi) = \begin{cases} 1 & \text{if } \xi_i \leq \xi \leq \xi_{i+1} \\ 0 & \text{otherwise,} \end{cases} \tag{3.1}$$

$$\text{for } p > 0 \quad N_{i,p}(\xi) = \frac{\xi - \xi_i}{\xi_{i+p} - \xi_i} n_{i,p-1} + \frac{\xi_{i+p+1} - \xi}{\xi_{i+p+1} - \xi_{i+1}} n_{i+1,p-1}. \tag{3.2}$$

Multivariate B-spline basis functions are defined by the tensor product of the univariate functions. The bivariate B-spline basis functions are defined as

$$N_{i,j}^{p,q}(\xi, \eta) = N_{i,p}(\xi) N_{j,q}(\eta). \tag{3.3}$$

Because B-spline functions are constructed in the parametric space, the conventional mapping process of FE analysis has to be redefined. The additional mapping, which requires the transformation of B-spline based elements from the physical to the parametric space, is well described in literature e.g. in [26, 27], thus we refer readers therein.

3.1 B-splines in MsFEM for 1D problems

To introduce our concept lets first consider for illustrative purposes a simplification of equation 2.1 reduced to 1D:

$$-\frac{\mathrm{d}}{\mathrm{d}x}\left(a(x)\frac{\mathrm{d}u}{\mathrm{d}x}\right) = f(x), \; x \in (0, L), \tag{3.4}$$

$$u(0) = \alpha, \tag{3.5}$$

$$a(L)\frac{\mathrm{d}u}{\mathrm{d}x}_{|x=L} = F, \tag{3.6}$$

where α, F, f are given. We use B-spline functions with $p = 2$ over the whole domain and a knot vector Ξ representing coarse mesh. For simplicity we assume the parametric space to be equal to the physical space, although it is not required.

[28] The modified basis functions that take into account heterogeneity of $a(x)$ will be computed by solution of the following auxiliary problem:

$$-\frac{\mathrm{d}}{\mathrm{d}x}\left(a(x)\frac{\mathrm{d}\phi_i}{\mathrm{d}x}\right) = \frac{\mathrm{d}^2 N_i}{\mathrm{d}x^2},\ x \in (x_1^i, x_2^i), \tag{3.7}$$

$$\phi_i(x_1^i) = \phi_i(x_2^i) = 0, \tag{3.8}$$

where (x_1^i, x_2^i) is the support of a B-spline function. It should be noted that the support consist of $p+1$ macroelements. For each B-spline function with non-zero values at 0 or L we are going to add another multiscale basis function constructed from homogeneous differential equation:

$$-\frac{\mathrm{d}}{\mathrm{d}x}\left(a(x)\frac{\mathrm{d}\phi_i^D}{\mathrm{d}x}\right) = 0,\ x \in (x_1^i, x_2^i), \tag{3.9}$$

$$\phi_i(x_1) = N_i(x_1) = 1, \tag{3.10}$$

$$\phi_i(x_2) = 0. \tag{3.11}$$

Problems 3.8 and 3.11 are solved numerically using standard FEM on the fine mesh. The modified shape functions ϕ are presented on the right diagram in Fig. 4 and are used to find MsFEM solution $\boldsymbol{u}^H$.

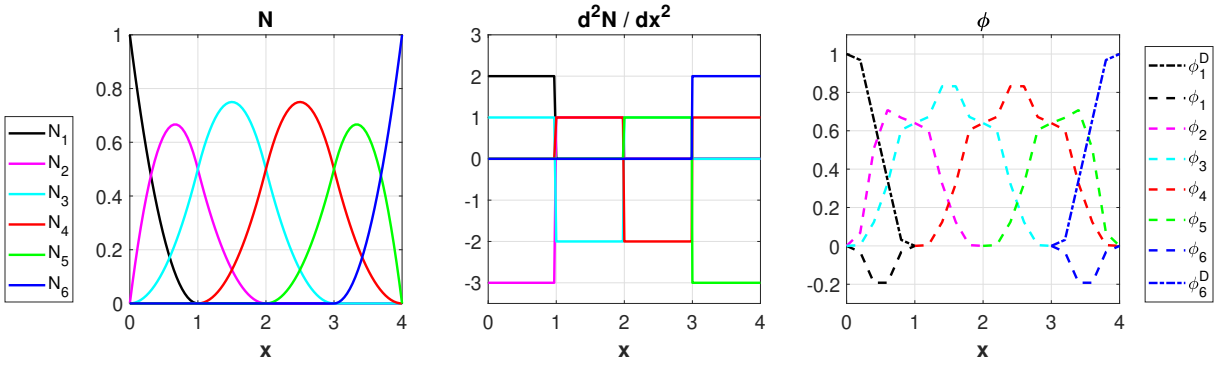

Figure 4: Undisturbed second order B-spline functions for the knot vector $\Xi = \{0,0,0,1,2,3,4,4,4\}$(left), their second derivatives (center), modified multiscale basis functions (right).

3.2 B-splines in MsFEM for 2D problems

Computations of the modified basis functions for 2D problem will be illustrated by an exemplary discretization and B-spline basis functions spanned on 3×3 mesh of macroelements (see Fig. 5). $p = q = 2$ was assumed. To construct multiscale basis function we solve a following local problem with the zero Dirichlet boundary condition and RHS determined by B-spline functions:

$$-\nabla \cdot (a(\boldsymbol{x})\nabla\phi_{i,j}) = \triangle N_{i,j},\ \boldsymbol{x} \in \Omega_i, \tag{3.12}$$

$$\phi_{i,j} = 0,\ \text{on } \partial\Omega_i, \tag{3.13}$$

where Ω_i is the support of $N_{i,j}$ function. In Fig. 6 we present an exemplary B-spline function, the corresponding source term, and the resulting multiscale basis function.

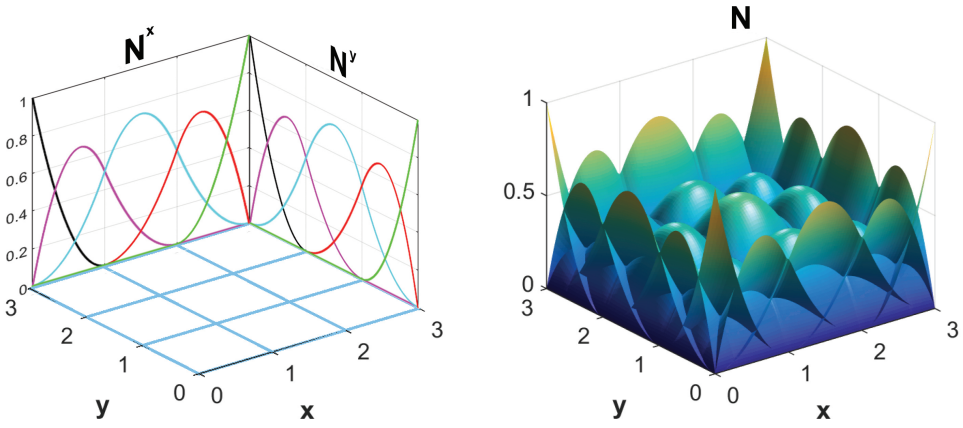

Figure 5: B-spline functions defined for the knot vectors $\Xi^x = \Xi^y = \{0, 0, 0, 1, 2, 3, 3, 3\}$ in 2D space.

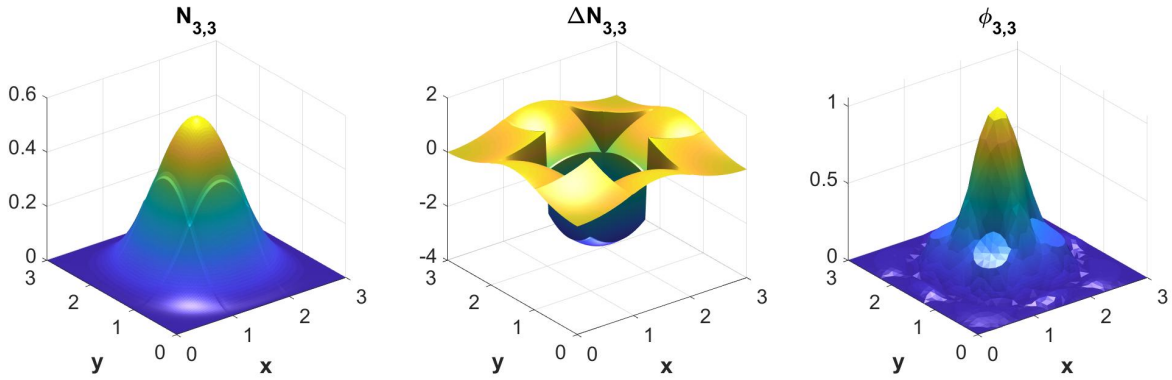

Figure 6: Second order B-spline function in 2D (left), Laplacian of the function (center), modified multiscale basis function (right).

For each B-spline function with non-zero values on the boundary we introduce two additional multiscale basis functions: $\phi^D_{i,j}$ and $\phi^N_{i,j}$. The first one is a solution of the problem:

$$-\nabla \cdot \left(a(\boldsymbol{x})\nabla\phi^D_{i,j}\right) = 0, \ \boldsymbol{x} \in \Omega_i, \tag{3.14}$$

$$\phi^D_{i,j} = N_{i,j}, \text{ on } \partial\Omega_i. \tag{3.15}$$

The second term is obtained by solving the same problem but with the Neumann boundary conditions:

$$-\nabla \cdot \left(a(\boldsymbol{x})\nabla\phi^N_{i,j}\right) = 0, \ \boldsymbol{x} \in \Omega_i, \tag{3.16}$$

$$\phi^N_{i,j} = 0, \text{ on } \partial\Omega_i \cap \partial\Omega, \tag{3.17}$$

$$a(\boldsymbol{x})\frac{\partial\phi^N_{i,j}}{\partial\tilde{n}} = \frac{\partial N_{i,j}}{\partial\tilde{n}}, \text{ on } \partial\Omega_i \cup \partial\Omega. \tag{3.18}$$

In Fig. 7 we present example of an original function and the corresponding modified function used for multiscale analysis.

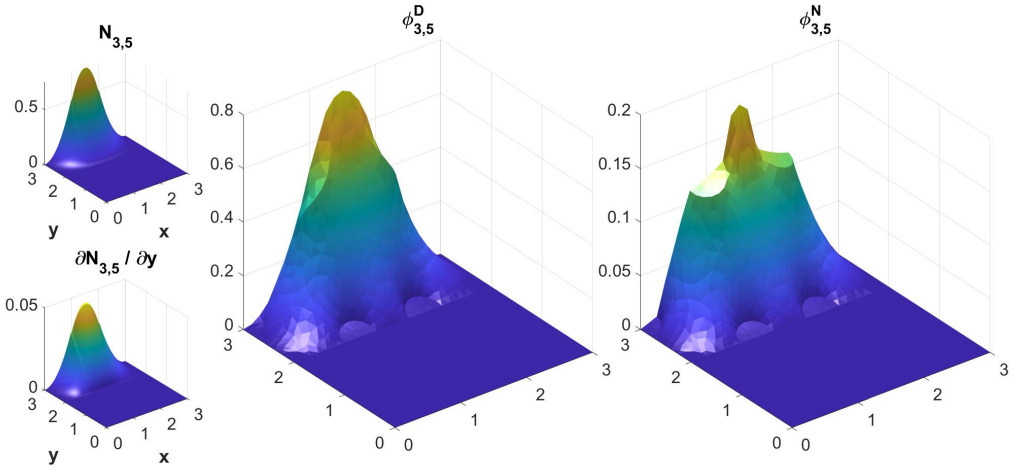

Figure 7: Second order B-spline function with non-zero values on the boundary and gradient on the function (left), two modified multiscale basis functions (center, right).

All the basis functions are computed numerically on the fine mesh. The inner functions $\phi_{i,j}$ approximate the solution inside the domain. The $\phi^D_{i,j}$ functions correspond to the multiscale basis function from 1D example and are responsible for reproducing Dirichlet boundary conditions of the global problem. By introducing $\phi^N_{i,j}$ we enrich function base with functions capable of approximating solution on Neumann boundary of the global problem. The latter functions are equal to zero on Dirichlet boundary $\partial\Omega_D$.

It is worth pointing out that in contrast to standard MsFEM we calculate the modified B-spline basis functions in their supports in one step. If the material and the coarse mesh are periodic one may significantly reduce the computation time since all coarse elements matrices are the same.

4 Numerical experiments

The results obtained from the multiscale method u^H are going to be compared with those obtained using the standard FEM applied on the fine mesh grid u_{FEM}, which will be called a reference solution. The comparison of the FEM results with the multiscale method results will expose the additional modeling error e^m introduced by the multiscale method.

$$e^m = u_{FEM} - u^H. \tag{4.1}$$

This error will be measured in the L_2 norm:

$$||e^m||_{L_2} = \left[\int_\Omega e^m \cdot e^m \mathrm{d}\Omega\right]^{\frac{1}{2}} \tag{4.2}$$

and in the H_1 seminorm:

$$||e^m||_E = \left[\int_\Omega \nabla e^m \cdot \nabla e^m \mathrm{d}\Omega\right]^{\frac{1}{2}}. \tag{4.3}$$

Convergence diagrams shown in this section present relative error norms i.e.:

$$\eta_{L_2} = \frac{||e^m||_{L_2}}{||u||_{L_2}}, \quad \eta_E = \frac{||e^m||_E}{||u||_E}. \tag{4.4}$$

4.1 Initial results

We present two illustrative examples of 1D and 2D problems that were solved using our modified MsFEM with B-spline basis functions.

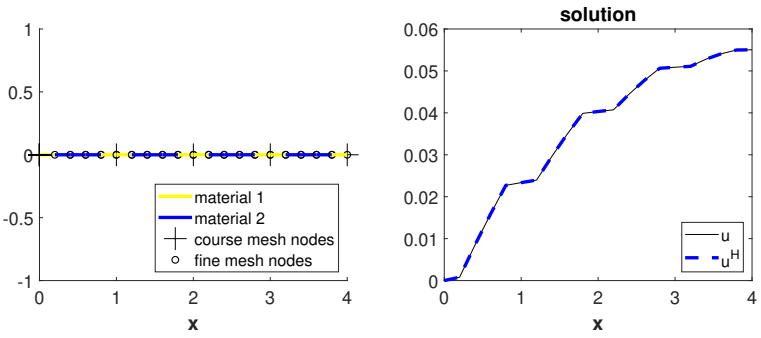

Figure 8: Example 1: Material distribution with coarse and fine meshes (left) and solution (right)

Example 1 In this example 1D problem 3.4 was considered with constant $f = 10$, the zero Dirichlet boundary conditions on the left end, and the Neumann boundary condition $F = 1.5$ on the right end. The domain consisted of nine subintervals with different material properties. We assumed $a = 10^4$ for material 1 and $a = 10^3$ for material 2 (see Fig. 8). The calculations were conducted twofold. The standard FEM approximation (fine mesh) with 21 dofs with linear shape functions was used to obtain a reference solution. Next, modified MsFEM with B-spline basis functions of second order spanned over 4 macroelements (coarse mesh) with 8 dofs was used to find a solution. The displacement achieved by both methods, u and u^H respectively, are shown on the right diagram in Fig. 8. They coincide very well.

Example 2 Next, we analyzed 2D flow in heterogeneous media in a square domain discretized with 3×3 coarse mesh with four different material permeability distributions (coefficient a, see Fig 9). Zero flow on the left edge and constant flux on the top edge and zero flux on the bottom and right edges were assumed. Again results from standard FEM and MsFEM are presented in juxtaposition to observe the difference between the two. Number of dofs for the FE analysis (microscale level) is equal to: (a) - 1085, (b) - 1181, (c) - 1049, (d) - 2401; Number of dofs in multiscale analysis (macroscale level) is equal to 65 for all examples.

This example reveals that the obtained solution with our approach shows good agreement with the reference solution. The maximum error does not exceed 6% measured in the L_2 norm. We observe that with the method we are able to obtain a solution with oscillation on the coarse mesh.

4.2 Convergence tests

In this section, we tested the method for various material distributions, coarse mesh sizes, and order of B-splines. The domain Ω in all examples is a unit square ($L = 1$). Fig. 10 presents three material distributions: M1, M2 (periodic), and RND (random). The examples with periodic material distribution are generated by arranging $n_o \times n_o$ elementary cells of the material pattern. The size of the elementary cell is $\varepsilon = \frac{L}{n_0}$. The random distribution was generated using Gaussian probability density inside the whole domain. The maximum element edge length of microscale mesh was assumed as $h_{max} = \frac{1}{8n_o}$ for periodic distribution and as $h_{max} = \frac{1}{256}$ for random distribution. Quadratic elements were used in the fine mesh.

Examples 3-6 were conducted for a problem with zero essential boundary conditions and various RHS. Example 7 was conducted for a problem with $f = 0$, zero flow on the left edge, constant flux on the top edge, and zero flux on the bottom and right edges. Error norms calculated from the results obtained with our method are shown in juxtaposition with error norms calculated from the results obtained from MsFEM and MsFEM with oversampling (MsFEMo) obtained on the same coarse mesh and are presented on the convergence plots.

Example 3 In this test we assumed homogeneous material with $a = 1$, in which the multiscale basis functions are interpolants of unmodified B-splines. We further assume RHS $f = 1000$ and the maximum element edge lengths of the fine mesh to be $h_{max} = \frac{1}{256}$. Size of macroelement H varied from 1/4 to 1/32. Diagram in Fig. 11 shows dependence of L_2 norm error on the coarse mesh size.

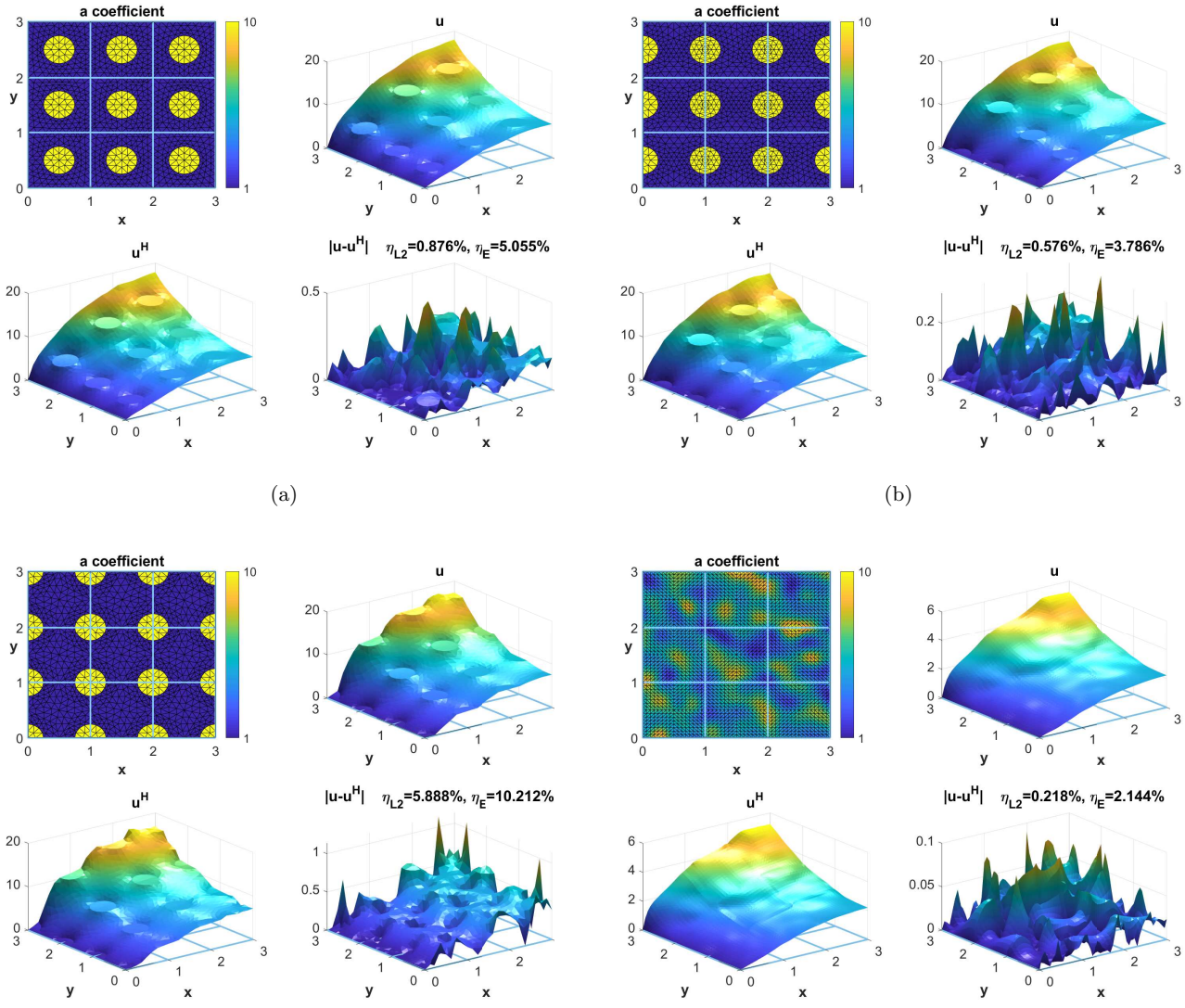

Figure 9: Example 2: 2D stationary flow in heterogeneous media calculations using MsFEM with B-spline basis functions and various permeability coefficient a distribution: (a)(b)(c) periodic, (d) random.

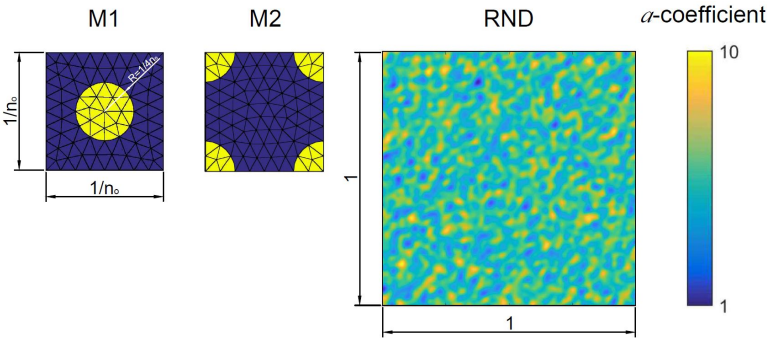

Figure 10: Material properties parameter distributions.

We observe the linear convergence with the decrease of size of the macroelements, that was expected. Also error reduction is observed with an increase of the order of B-splines.

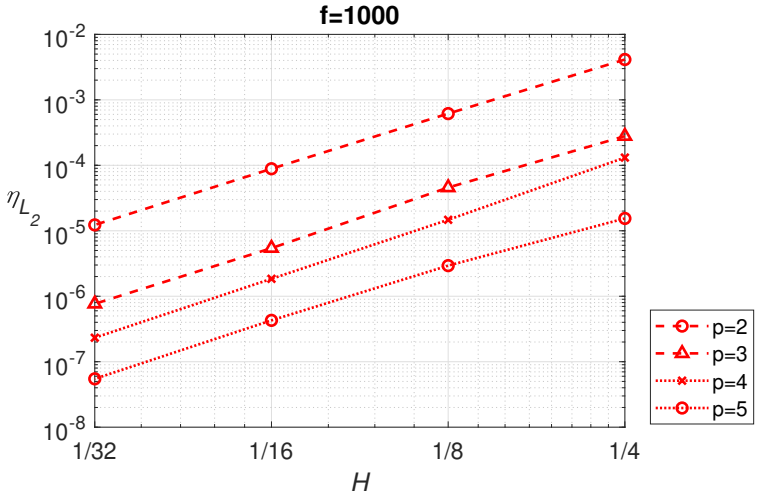

Figure 11: Dependence of L_2 norm error on coarse scale refinement and order of B-splines for homogeneous example, $p = 2 - 5$.

Example 4 Next we present results for different materiel distributions (M1, M2, RND). We assumed constant RHS $f = 1000$ and fixed $n_o = 32$ for both M1 and M2. Size of macroelement varied from $H = 1/4, 1/8, 1/16, 1/32$, which corresponds to $\varepsilon/H = 8, 4, 2, 1$ for periodic examples. The results in Fig. 12 reveal large decrease of the error up to one order of magnitude for $p = 2$ and two orders of magnitude for $p > 2$ in comparison to standard MsFEM and MsFEMo for $\varepsilon/H = 8 - 4$. However, after this point, when $H \approx \varepsilon$ a strong resonance effect [8] is observed for $H < 1/8$, according to the theoretical error bound:

$$||e^m||_{L_2} = O(H^2 + \varepsilon/H). \tag{4.5}$$

Example 5 In this test, we further examine the case with periodic material distribution M2. We decreased gradually characteristic size $\varepsilon = 1/32, 1/64, 1/128$, that corresponds to $n_o = 32, 64, 128$ numbers of repetitions of the elementary cell in the domain. We set order of B-spline functions to $p = 2$. In Fig. 13 we present a convergence plot for these three cases. Indeed the resonance effect becomes dominant for $H < 1/16$ when ε was decreased to $1/128$.

Example 6 In this test we repeat **Example 4** for fixed $\varepsilon/H = 1$ or $H = 1/32$, and we varied order of B-spline from $p = 2 - 8$. In Fig. 14 we can see diagrams of L_2 error norm vs. approximation order p. We observe that B-spline based MsFEM is superior in particular for $p > 3$. In the case of periodic material, error stabilizes to one value. Similar stabilization in MsFEM was reported for the oversampling size in [21]. The increase of oversampling size reduces the error, however, size bigger than 3×3 macroelements did not enhance the results.

Example 7 Our last test shows results for more demanding boundary conditions and zero RHS, while the remaining assumptions were assumed as in **Example 4**. Converges plots, depicted in Fig. 15, again reveal better results for a bigger number of material repetitions in one macroelement. A strong resonance effect is observed.

5 Conclusions

In this paper, we presented applications of B-spline basis functions in the MsFEM framework. B-splines are the linear combination of piecewise smooth basis functions of C^{p-1} continuity. In standard MsFEM, shape functions need to be modified on the boundary, which is usually done by the oversampling technique in order to reduce the error caused by the imposition of the boundary conditions. In our approach, we propose to calculate the whole basis function in one step, thus there is no

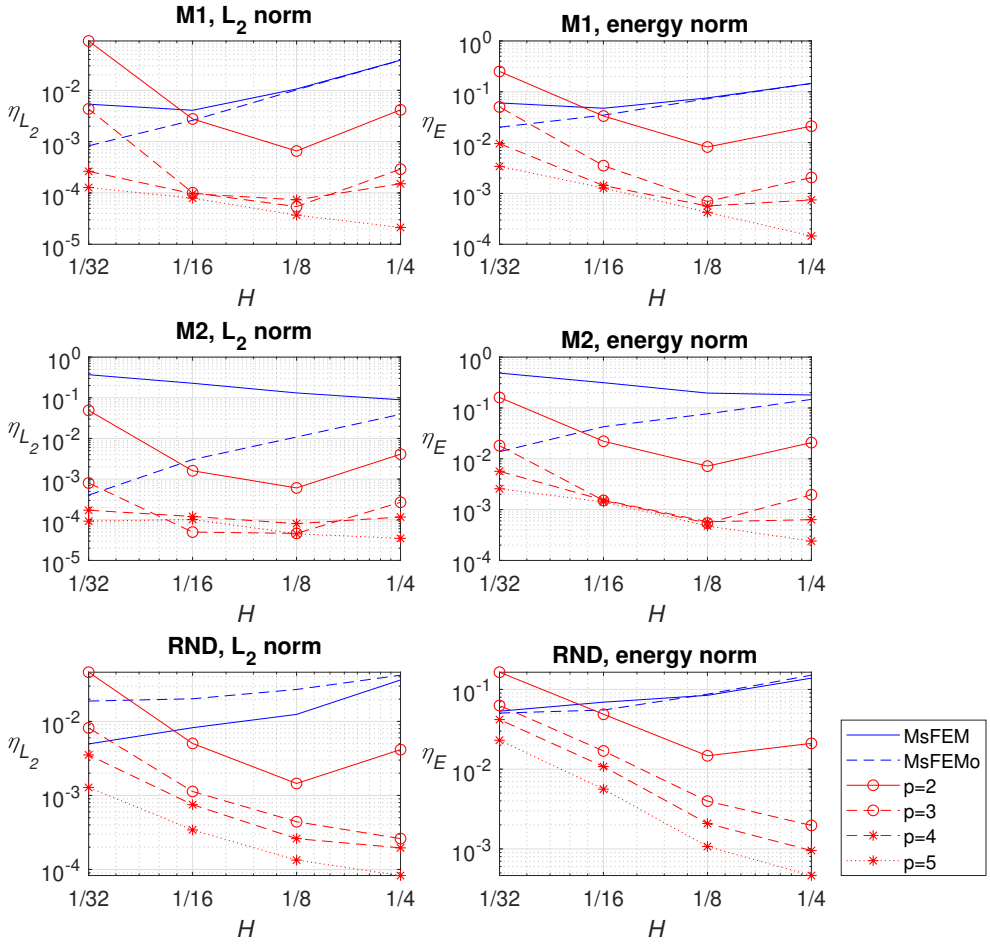

Figure 12: Dependence of L_2 and energy norms of error on coarse scale refinement for M1 and M2 exampels with $n_o = 32$, and RND example.

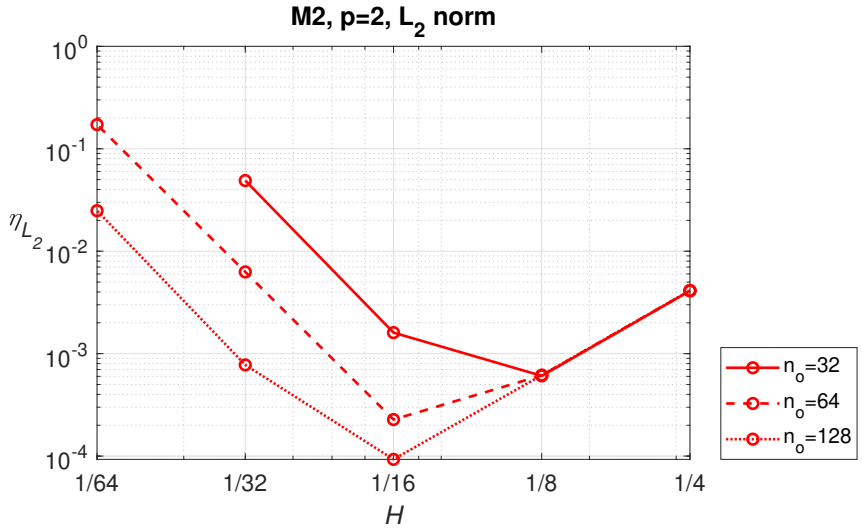

Figure 13: Dependence of L_2 norm of error on coarse scale refinement for M2 example with $n_o = 32$, 64, and 128.

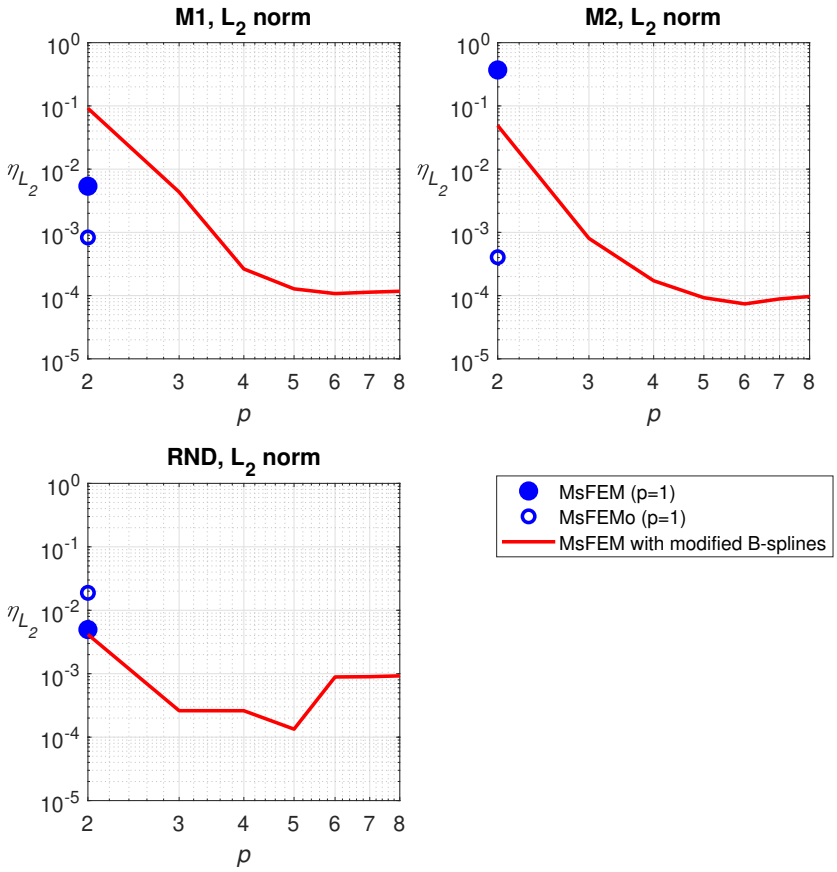

Figure 14: Dependence of L_2 norm of error on p increase for M1, M2 examples with $n_o = 32$ repetitions, and RND example. Fixed coarse mesh size $H = 1/32$ ($\varepsilon/H = 1$). Note that error norm calculated from the results obtained by MsFEM and MsFEMo are depicted as a points and no change of the order of approximation was done in this cases.

need for any modification of the inner basis functions on the edge because they diminish to zero. The approach was tested on the problem of flow in heterogeneous media with multiscale basis functions for the order of $p \geqslant 2$. Several 2D examples with periodic and random material properties distribution were analyzed. Comparison with standard MsFEM and MsFEM with oversampling modification was shown on convergence diagrams.

Results indicate that up to 4-8 oscillations of the material properties per macroelement the method converges and outperforms MsFEM with oversampling modifications. Over that point, when the number of oscillations decreases to 1 per macroelement, we recognized a strong resonance effect. The effect can be reduced by increasing the order of B-spline functions keeping the error at the same level as the results obtained by MsFEM with oversampling, or even smaller.

The proposed approach leads to significant improvement in accuracy for fast varying material properties and produces smooth results of the high order. These conclusions encourage us further to work on the method, in particular, to overcome the resonance effect.

6 Acknowledgment

This work was supported by the project nr 2017/25/B/ST8/02752 funded by National Science Centre.

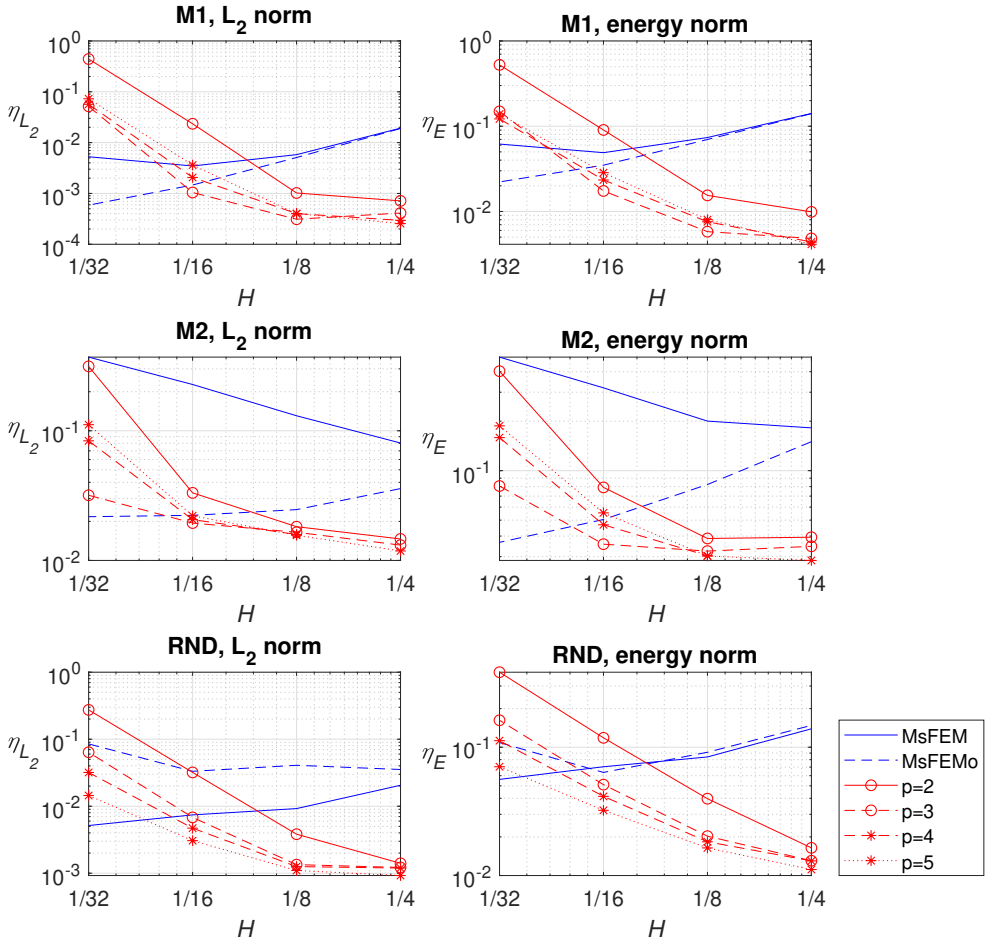

Figure 15: Dependence of L_2 and energy norms of error on coarse scale refinement for M1 and M2 exampels with $n_o = 32$, and RND example.

References

[1] G. Papanicolau, A. Bensoussan, and J. Lions. *Asymptotic Analysis for Periodic Structures*. Studies in Mathematics and its Applications. Elsevier Science, 1978.

[2] T.I. Zohdi and P. Wriggers. *An Introduction to Computational Micromechanics*. Lecture Notes in Applied and Computational Mechanics. Springer Berlin Heidelberg, 2004.

[3] M. G. D. Geers, V. G. Kouznetsova, and W. A. M. Brekelmans. Multi-scale computational homogenization. *International Journal for Numerical Methods in Engineering*, 54:1235–1260, 2002.

[4] F. Feyel and J. L. Chaboche. FE^2 multiscale approach for modelling the elastoviscoplastic behaviour of long fiber SiC/Ti composite materials. *Computer Methods in Applied Mechanics and Engineering*, 183:309–330, 2000.

[5] W. E and B. Engquist. The heterogeneous multiscale methods. *Computational Materials Science*, 1:87–133, 2003.

[6] L. Madej, P. D. Hodgson, and M. Pietrzyk. Multi-scale rheological model for discontinuous phenomena in materials under deformation conditions. *Comput. Mater. Sc.*, 38:685–691, 2007.

[7] L. Madej, P. D. Hodgson, and M. Pietrzyk. The validation of a multiscale rheological model of discontinuous phenomena during metal rolling. *Comput. Mater. Sc.*, 41:236–241, 2007.

[8] T. Hou and X. Wu. A multiscale finite element method for elliptic problems in composite materials and porous media. *Journal of Computational Physics*, 134(1):169–189, 1997.

[9] T. Y. Hou, X.-H. Wu, and Z. Cai. Convergence of a multiscale finite element method for elliptic problems with rapidly oscillating coefficients. *Math. Comput.*, 68(227):913–943, July 1999.

[10] Y. Efendiev, V. Ginting, T. Hou, and R. Ewing. Accurate multiscale finite element methods for two-phase flow simulations. *Journal of Computational Physics*, 220(1):155 – 174, 2006.

[11] L. H. Nguyen and D. Schillinger. A residual-driven local iterative corrector scheme for the multiscale finite element method. *Journal of Computational Physics*, 377:60 – 88, 2019.

[12] Kai Gao, Shubin Fu, and Eric T. Chung. A high-order multiscale finite-element method for time-domain acoustic-wave modeling. *Journal of Computational Physics*, 360:120 – 136, 2018.

[13] W. Cecot and M. Oleksy. High order FEM for multigrid homogenization. *Computers & Mathematics with Applications*, 70(7):1391 – 1400, 2015. High-Order Finite Element and Isogeometric Methods.

[14] H. Liu, X. Sun, Y. Xu, and X. Chu. A hierarchical multilevel finite element method for mechanical analyses of periodical composite structures. *Composite Structures*, 131:115–127, 2015.

[15] P. Degond, A. Lozinski, B. Muljadi, and J. Narski. Crouzeix-raviart MsFEM with bubble functions for diffusion and advection-diffusion in perforated media. *Communications in Computational Physics*, 17, 09 2013.

[16] F. Casadei, J.J. Rimoli, and M. Ruzzene. A geometric multiscale finite element method for the dynamic analysis of heterogeneous solids. *Computer Methods in Applied Mechanics and Engineering*, 263:56 – 70, 2013.

[17] H. Liu and H.W. Zhang. An equivalent multiscale method for 2D static and dynamic analyses of lattice truss materials. *Advances in Engineering Software*, 75:14 – 29, 2014.

[18] M. Oleksy and W. Cecot. Application of hp-adaptive finite element method to two-scale computation. *Archives of Computational Methods in Engineering*, 22(1):105–134, Jan 2015.

[19] M. Klimczak and W. Cecot. An adaptive msfem for nonperiodic viscoelastic composites. *International Journal for Numerical Methods in Engineering*, 114(8):861–881, 2018.

[20] Hui Liu, Yiqiang Wang, Hongming Zong, and Michael Yu Wang. Efficient structure topology optimization by using the multiscale finite element method. *Structural and Multidisciplinary Optimization*, 58(4):1411–1430, Oct 2018.

[21] H.-W. Zhang, J.-K. Wu, J. Lü, and Z.-D. Fu. Extended multiscale finite element method for mechanical analysis of heterogeneous materials. *Acta Mechanica Sinica*, 26(6):899–920, Dec 2010.

[22] Ping Fu, Hui Liu, and Xihua Chu. An efficient multiscale computational formulation for geometric nonlinear analysis of heterogeneous piezoelectric composite. *Composite Structures*, 167:191 – 206, 2017.

[23] K. Hollaus and J. Schöberl. Multi-scale FEM and magnetic vector potential a for 3D eddy currents in laminated media. *COMPEL - The international journal for computation and mathematics in electrical and electronic engineering*, 34(5):1598–1608, 2015.

[24] S. Ye, Y. Xue, and C. Xie. Application of the multiscale finite element method to flow in heterogeneous porous media. *Water Resources Research - WATER RESOUR RES*, 40, 09 2004.

[25] T.J.R. Hughes, J.A. Cottrell, and Y. Bazilevs. Isogeometric analysis: CAD, finite elements, NURBS, exact geometry and mesh refinement. *Computer Methods in Applied Mechanics and Engineering*, 194(39):4135 – 4195, 2005.

[26] Vishal Agrawal and Sachin S. Gautam. IGA: A simplified introduction and implementation details for finite element users. *Journal of The Institution of Engineers (India): Series C*, 100(3):561–585, Jun 2019.

[27] A. Perduta and R. Putanowicz. Tools and techniques for building models for isogeometric analysis. *Advances in Engineering Software*, 127:70 – 81, 2019.

[28] Soheil Soghrati and Ilinca Stanciulescu. Systematic construction of higher order bases for the finite element analysis of multiscale elliptic problems. *Mechanics Research Communications*, 52:11 – 18, 2013.

3.2 Article 2: The iterative multiscale finite element method for sandwich beams and plates

M. Dryzek and W. Cecot. The iterative multiscale finite element method for sandwich beams and plates. *International Journal for Numerical Methods in Engineering*, 122:6714–6735, 2021. 200 points, IF = 3.477, `https://doi.org/10.1002/nme.6808`. Article included under license number 5430170978936.

Received: 19 March 2021 | Revised: 3 August 2021 | Accepted: 9 August 2021

DOI: 10.1002/nme.6808

RESEARCH ARTICLE

WILEY

The iterative multiscale finite element method for sandwich beams and plates

Mateusz Dryzek | **Witold Cecot**

Faculty of Civil Engineering, Cracow University of Technology, Krakow, Poland

Correspondence
Witold Cecot, Cracow University of Technology, Krakow, Poland.
Email: plcecot@cyf-kr.edu.pl

Abstract

We present an adaptation of the multiscale finite element method to the analysis of sandwich beams and plates with complex lattice layers. The proposed modification significantly reduces the number of degrees of freedom (even by four orders) due to the anisotropic higher-order coarse-scale approximation and the novel shape functions that take into account the microscale boundary conditions. Moreover, the local iterative corrector scheme Nguyen and Schillinger (2019) adapted for the bending-dominated responses of sandwich structures provides converges of the coarse mesh approximation to the best possible fine-mesh solution. Several numerical examples are presented to demonstrate the capabilities of the method. We found that the proposed modifications of the shape functions and the higher-order coarse mesh approximation increase the convergence rate. Finally, we validated the proposed model by comparison of the numerical results with experimental ones for a sandwich panel with a dual corrugated high-density fiberboard core. Very good consistency of both results was observed.

KEYWORDS

composite structure, multiscale finite element method, residual-driven correction, sandwich beam and plate

1 | INTRODUCTION

In recent years, we observe a fast development of new materials and the technological advancements that allow for their manufacturing. The most relevant examples include composites and metamaterials that are often obtained by additive manufacturing, commonly referred to as three-dimensional (3D) printing. Scientists and engineers try to bring these materials into cutting-edge sectors of progressive industries including aerospace, medicine, automotive, and building engineering. The novel properties of the materials are usually obtained by combining two or more constituents, or by rearranging matter in a form of sophisticated microstructures (see Figure 1). We focus in this article on structural elements that at the macroscale can be classified by their dimensionality as beams or plates, in particular on composite laminates, sandwich panels, multilayered lattice structures. Modeling such elements with a detailed 3D representation of the microstructure is a very challenging task due to a large number of degrees of freedom (dofs). Therefore, we propose an adaptation of the multiscale finite element method (MsFEM)[1] to reduce the computational cost of modeling composite beams and plates.

The main purpose of any multiscale method is to reduce significantly the number of dofs in numerical simulation of partial differential equations with fast varying coefficients. It is done primarily by establishing a relationship between

FIGURE 1 Examples of sophisticated microstructures: The first in the world 3D printed concrete bridge in Madrid, Spain (A) and a light layer sandwich panel with a dual corrugated high-density fiberboard core (B)

microscale characteristics and macroscale properties. The most frequently used approaches to this problem are *the asymptotic homogenization*,[2] *the representative volume element (RVE) method* (including FE^2),[3] and *the MsFEM*.[1]

The asymptotic approach makes use of a unit cell followed by an analysis of a boundary value problem with constant coefficients to evaluate the homogenized solution understood as the limit of a certain sequence of functions. The method proposed by Papanicolaou et al.[2] is mathematically sound and was successfully applied but only for periodic composites with the scale separation property.

The RVE, that is, a minimal material volume that contains sufficient information about the microstructure, is used to determine the effective macroscale properties by imposing specific boundary conditions to the RVE and performing numerical strength tests. The key type of the RVE based method is FE^2 version[3] that allows predictions of the mechanical behavior of structures made of heterogeneous materials with both linear and nonlinear constitutive laws. It was also considered for modeling of beams and plates and called numerical plate testing for two-scale analyzes.[4] Recently multiscale plate element were developed based on the higher-order computational continua (HC^2) formulation.[5] Experimental validation of the method for fiber metal laminate (FE^2),[6] reinforced concrete beams and plates (FE^2),[7] and fiberboard sandwich panels (RVE)[8] is discussed in the cited papers. It should be noted that the RVE approach may be used if two assumptions are satisfied, that is, periodicity and scale separation.

The MsFEM[1] starts with a macroscale discretization that is followed by the independent refinement of each coarse-scale element (macroelement) in order to obtain a discretization that complies with the material heterogeneity. The multiscale shape functions of the method are obtained as solutions to local problems in the macroelement domains to incorporate the microscale details into the macroelement stiffness matrices (refer to Hou and Wu[1]). The method requires neither the assumption of the scale separation nor the periodicity of the microstructure. Furthermore, the calculations can be easily parallelized.

While defining the local problems for the multiscale shape functions appropriate boundary conditions should be imposed. For the static analysis, the best ones would be determined by the exact solution. Pragmatically, the traces of the standard undisturbed shape functions were assumed at first on the coarse element boundaries. Although the resulting multiscale shape functions could capture details of the microstructure inside the element domains there was a significant error close to the macroelement boundaries. Therefore, a careful choice of the boundary conditions is necessary, for example, one may use functions that are the solutions of the local one-dimensional (1D) problems along coarse element edges[9] or oscillatory boundary conditions as the result of the oversampling technique.[1,10] Another way to improve the MsFEM solution is to use an iterative approach.[11,12] Finally, higher-order macroscale shape functions of either Lagrange,[13] hierarchic,[14,15] Crouzeix-Raviart,[16] or B-spline[17] type are used. Multipoint elements[18,19] were introduced bringing MsFEM closer to the static condensation method. The recent development of the method includes coarse mesh adaptivity,[20,21] topology optimization,[22] as well as coupling with the Discontinuous Petrov–Galerkin method[23] and the RVE approach for the three-level analysis.[24]

Originally, the MsFEM was developed to solve flow in highly heterogeneous porous media. More recently, the method was modified to solve problems of elasticity (the extended MsFEM[25]), composites, and metamaterials. Several other engineering problems were modeled using MsFEM including viscoelastic asphalt concrete,[21,26] heterogeneous piezoelectric

composite,[27] and regional land subsidence.[28] There are only a few articles tying MsFEM with beam and plate problems. We refer to Reference 29 where authors are using boundary conditions of laminate theory with the method.

In this article, an adaptation of MsFEM with a residual-driven corrector scheme to analyze structures with one or two dominant dimensions like beams and plates is proposed. In such structures dominating bending modes are the reasons for large modeling errors. We reduced it significantly by the iterative scheme[12] with a novel anisotropic higher-order approximation and incorporation of the boundary conditions of the microscale problem to the multiscale shape functions.

The article is divided into five sections. In Section 2, we introduce the problem of beams and plates with composite, lattice structures and briefly introduce MsFEM with linear and higher-order multiscale basis functions that incorporate the kinematic and static microscale boundary conditions. Later in this section, we present the iterative scheme derivation based on the residuum as a load source in local corrector problems. In Section 3, we study the convergence of the method on various examples of beams and plates, including model verification with a closed formula and validation by experimental results. In Section 4, we present conclusions and further research plans. Finally, in Appendices A and B we show how to construct multiscale basis functions and how to generate them using higher-order formulas for the considered problems.

2 | PROBLEM FORMULATION AND MSFEM IDEA

We begin with considering sandwich beams and plates as either two-dimensional (2D) or 3D solid bodies satisfying the linear elasticity equations at the microscale that read:

Find displacement $\boldsymbol{u}$ *in domain* $\Omega \subset \mathbb{R}^n (n = 2 \text{ or } 3)$ *such that:*

$$-\bigtriangledown \cdot \left(\boldsymbol{C}(\boldsymbol{x})\bigtriangledown_s \boldsymbol{u}\right) = \boldsymbol{f},\ \forall \omega_s \subset \Omega, \tag{1}$$

$$\boldsymbol{u} = \hat{\boldsymbol{u}},\ \text{on } \Gamma^D, \tag{2}$$

$$\boldsymbol{t} = \hat{\boldsymbol{t}},\ \text{on } \Gamma^N, \tag{3}$$

where Γ^D and Γ^N denote boundary parts with the Dirichlet and Neumann conditions, $\Gamma^D \cup \Gamma^N = \partial\Omega$, and $\Gamma^D \cap \Gamma^N = \emptyset$. Continuity conditions for both displacement and traction on the interfaces between subdomains ω_s are assumed, $\hat{\boldsymbol{u}}$ and $\hat{\boldsymbol{t}}$ donate known displacement and loading, $\boldsymbol{t} = \left(\boldsymbol{C}(\boldsymbol{x})\bigtriangledown_s \boldsymbol{u}\right) \cdot \boldsymbol{n}$, and $\bigtriangledown_s$ is the symmetric part of the gradient operator, that is, $\bigtriangledown_s(\bullet) = ((\bullet) \otimes \bigtriangledown + \bigtriangledown \otimes (\bullet))/2$. $\boldsymbol{C}$ stands for elliptic, bounded, and highly oscillating elasticity tensor. The material parameters are differentiable (typically constant) in each subdomain $\omega_s, s = 1, 2 \ \ldots \ N_\omega$.

The corresponding weak form of (1)–(3) reads:

Find displacement $\boldsymbol{u} \in \boldsymbol{H}_1^0(\Omega) + \hat{\boldsymbol{u}}$ *such that:*

$$\int_\Omega \bigtriangledown \boldsymbol{v} \cdot \left(\boldsymbol{C}(\boldsymbol{x})\bigtriangledown_s \boldsymbol{u}\right) \mathrm{d}\Omega = \int_\Omega \boldsymbol{v} \cdot \boldsymbol{f} \mathrm{d}\Omega + \int_{\Gamma^N} \boldsymbol{v} \cdot \hat{\boldsymbol{t}} \mathrm{d}\Gamma, \forall \boldsymbol{v} \in \boldsymbol{V}, \tag{4}$$

where $\boldsymbol{V} = \boldsymbol{H}_1^0(\Omega)$ and $\boldsymbol{H}_1^0(\Omega) = \{\boldsymbol{v} \in \boldsymbol{H}_1^0(\Omega) \ : \ \boldsymbol{v} = 0|_{\Gamma^D}\}$

In MsFEM two meshes are used. For beams, we start with the generation of a coarse grid of rectangular macroelements Ω_i $(i = 1, 2 \ \ldots \ N_{el})$. We assume that there is only one macroelement in the depth direction (see Figure 2A). Similarly, brick type macroelements for plates have one dimension equal to the plate thickness and quadrilateral top and bottom faces (see Figure 2B). In each macroelement, a fine mesh of size h that captures the microscale details is generated. If we want to use the iterative scheme the fine meshes need to comply (match) on the coarse mesh skeleton.

The following decomposition of the solution $\boldsymbol{u}$ in each macroelement Ω_i is assumed after:[12]

$$\boldsymbol{u} = \boldsymbol{u}_a + \boldsymbol{u}_b, \tag{5}$$

where $\boldsymbol{u}_a$ and $\boldsymbol{u}_b$ are $\boldsymbol{C}(\boldsymbol{x})$-orthogonal, that is, $\int_{\Omega_i} \bigtriangledown \boldsymbol{u}_b \cdot \left(\boldsymbol{C}(\boldsymbol{x})\bigtriangledown_s \boldsymbol{u}_a\right) \mathrm{d}\Omega = \boldsymbol{0}$. The $\boldsymbol{u}_a$ component satisfies the following problem with zero loading:

$$-\bigtriangledown \cdot \left(\boldsymbol{C}(\boldsymbol{x})\bigtriangledown_s \boldsymbol{u}_a\right) = \boldsymbol{0},\ \text{in } \Omega_i, \tag{6}$$

$$\boldsymbol{u}_a = \boldsymbol{u},\ \text{on } \Gamma_i^D, \tag{7}$$

$$\boldsymbol{t}_a = \boldsymbol{0},\ \text{on } \Gamma_i^N, \tag{8}$$

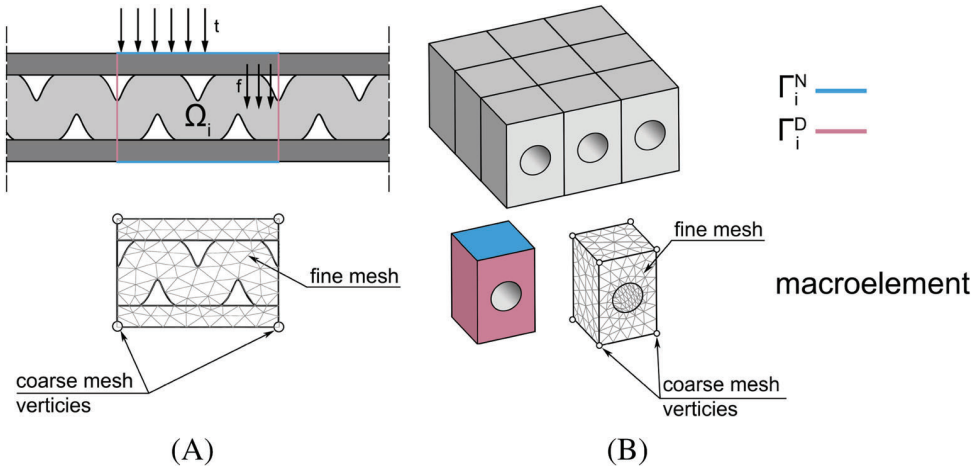

FIGURE 2 Multiscale finite element method discretization of beams (A) and plates (B)

where Γ_i^N denotes top and bottom beam edges or plate faces with known traction $\hat{\boldsymbol{t}}$ and Γ_i^D stands for the vertical element boundaries. The Dirichlet boundary condition is defined by the unknown exact solution $\boldsymbol{u}$ of problem (1)–(3).

By the orthogonality, the second component $\boldsymbol{u}_b$ can be evaluated locally, independently for each macroelement and it satisfies the following nonhomogeneous equation with zero displacement on Γ_i^D:

$$-\bigtriangledown \cdot \left(\boldsymbol{C}(\boldsymbol{x})\bigtriangledown_s \boldsymbol{u}_b\right) = \boldsymbol{f}, \text{ in } \Omega_i, \tag{9}$$

$$\boldsymbol{u}_b = \boldsymbol{0}, \text{ on } \Gamma_i^D, \tag{10}$$

$$\boldsymbol{t}_b = \hat{\boldsymbol{t}}, \text{ on } \Gamma_i^N. \tag{11}$$

Thus, we can define multiscale basis functions $\boldsymbol{\phi}_k$ as solutions to problem (6)–(8) with $\boldsymbol{d}_k$ ($k = 1, 2 \ldots K$) as the assumed Dirichlet boundary condition:

$$-\bigtriangledown \cdot \left(\boldsymbol{C}(\boldsymbol{x})\bigtriangledown_s \boldsymbol{\phi}_k\right) = \boldsymbol{0}, \text{ in } \Omega_i, \tag{12}$$

$$\boldsymbol{\phi}_k = \boldsymbol{d}_k, \text{ on } \Gamma_i^D, \tag{13}$$

$$\boldsymbol{t}_k = \boldsymbol{0}, \text{ on } \Gamma_i^N, \tag{14}$$

where K denotes total number of the multiscale basis functions. All this functions are attributed only to coarse element boundaries and the system of linear equations for coarse scale global solution $\boldsymbol{u}^H \in \boldsymbol{V}^H$ reads:

$$\int_\Omega \bigtriangledown \boldsymbol{v}^H \cdot \left(\boldsymbol{C}(\boldsymbol{x})\bigtriangledown_s \boldsymbol{u}^H\right) \mathrm{d}\Omega = \int_\Omega \boldsymbol{v}^H \cdot \boldsymbol{f} \mathrm{d}\Omega + \int_{\Gamma^N} \boldsymbol{v}^H \cdot \hat{\boldsymbol{t}} \mathrm{d}\Gamma, \quad \forall \boldsymbol{v}^H \in \boldsymbol{V}^H, \tag{15}$$

where $\boldsymbol{V}^H = \text{span}\left\{\boldsymbol{\phi}_1(\boldsymbol{x}), \boldsymbol{\phi}_2(\boldsymbol{x}), \ldots \boldsymbol{\phi}_K(\boldsymbol{x})\right\}$.

Problem (12)–(14) is solved numerically on the fine mesh for each macroelement separately and the obtained dofs set up a column of prolongation matrix $P_{N\times M}$, where M is the number of shape functions in macroelement Ω_i and N is the number of dofs of the fine mesh in Ω_i. The prolongation matrix transforms coarse dofs to fine dofs and is calculated for each macroelement individually. This process is easily parallelized. Moreover, in the case of periodicity, the matrix is calculated only once, greatly reducing the computation time.

The prolongation matrices are used to compute macroelement stiffness matrices $\boldsymbol{K}^H$ and vectors $\boldsymbol{f}^H$ by simple algebraic operation:

$$\boldsymbol{K}_i^H = \boldsymbol{P}_i^T \boldsymbol{K}_i^h \boldsymbol{P}_i, \quad \boldsymbol{f}_i^H = \boldsymbol{P}_i^T \boldsymbol{f}_i^h, \tag{16}$$

where matrices $\boldsymbol{K}_i^h$ and vectors $\boldsymbol{f}_i^h$ are assembled only in macroelements Ω_i. No integration is done to obtain the coarse element matrices and vectors. It is worth pointing out that $\boldsymbol{K}_i^h$ is computed when one solves problem (12)–(14), thus it can be reused here. $\boldsymbol{f}_i^h$ has to be assembled but it will be also needed to compute $\boldsymbol{u}_b$ approximation.

After assembling on the coarse level we can solve for the coarse mesh skeleton dofs $\boldsymbol{u}^H$:

$$\boldsymbol{K}^H \boldsymbol{u}^H = \boldsymbol{f}^H. \tag{17}$$

Knowing $\boldsymbol{u}^H$, it is easy to calculate, element by element, the fine-mesh dofs (approximation of $\boldsymbol{u}_a$):

$$\boldsymbol{u}_i^h = \boldsymbol{P}_i \boldsymbol{u}_i^H. \tag{18}$$

The final multiscale solution $\boldsymbol{u}_i^{ms}$ is obtain by summing $\boldsymbol{u}_i^h$ with locally evaluated bubble part $\boldsymbol{u}_i^b$:

$$\boldsymbol{u}_i^{ms} = \boldsymbol{u}_i^h + \boldsymbol{u}_i^b. \tag{19}$$

2.1 | Novel multiscale shape functions

The test and trial MsFEM shape functions are solutions to problem (12)–(14) where $\boldsymbol{d}_k$ have to be given. In the simplest case of the standard MsFEM, $\boldsymbol{d}_k$ boundary conditions are traces of bilinear standard shape functions on the whole macroelement boundary Γ_i (see example in Figure 3A). Whenever there are holes inside of a macroelement the zero traction condition on their edges are built into the coarse shape functions. We propose to do the same for the top and bottom edges (or faces) of the coarse elements for the considered sandwich structures. Therefore, we assume the kinematic boundary conditions $\boldsymbol{d}_k$ only on Γ_i^D edges (faces). The results are presented in Figure 3(B). Appendix A exemplifies the procedure for the calculation of boundary conditions $\boldsymbol{d}_k$ for a linear multiscale approximation.

For the convenience of the assembling process, we unite both vertices of the vertical edges (beams and plates) or top and bottom edges of the vertical faces (plates) and represent them either by the vertex or the edge nodes on the midplane (see Figure 4). Such a logical interpretation is possible here since all macroelements compose only one layer. Therefore, for each element, there are neither elements above nor below it and virtually one may consider the 2D beam elements as 1D segments as well as 3D plate elements as 2D polygons. This approach gives us 4 (for beams) and 6 (for plates) dofs per a united edge node when the linear approximation is used, and the global solution $\boldsymbol{u}^H$ reads:

$$\text{for beams: } \boldsymbol{u}^H = \sum_{j=1}^{N_{\text{nodes}}} (\boldsymbol{\phi}_{j,bz} u_{j,bz} + \boldsymbol{\phi}_{j,bx} u_{j,bx} + \boldsymbol{\phi}_{j,tz} u_{j,tz} + \boldsymbol{\phi}_{j,tx} u_{j,tx}), \tag{20}$$

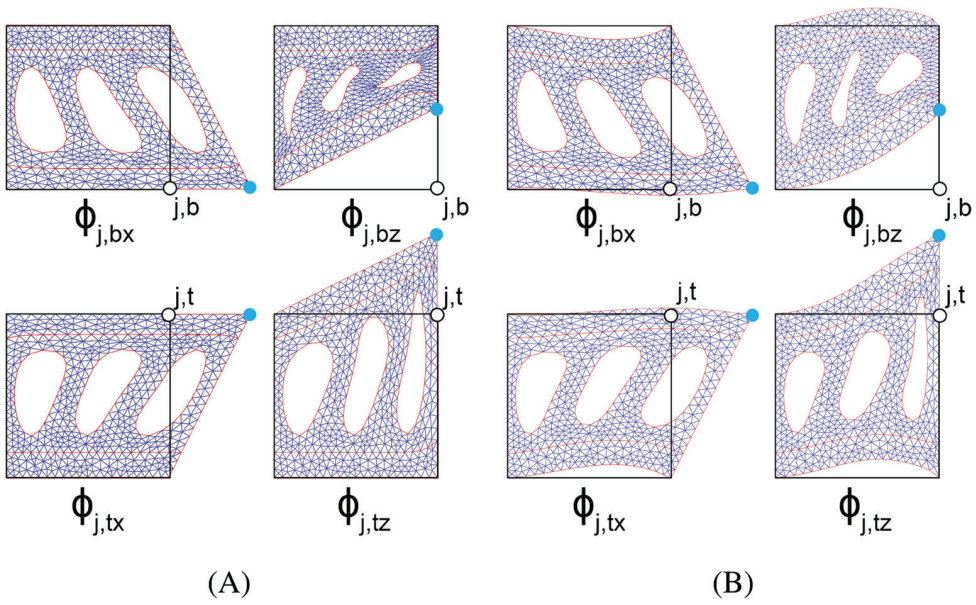

FIGURE 3 Standard multiscale shape functions (A) and new multiscale shape functions used in a beam model (zero traction on top and bottom edges) (B)

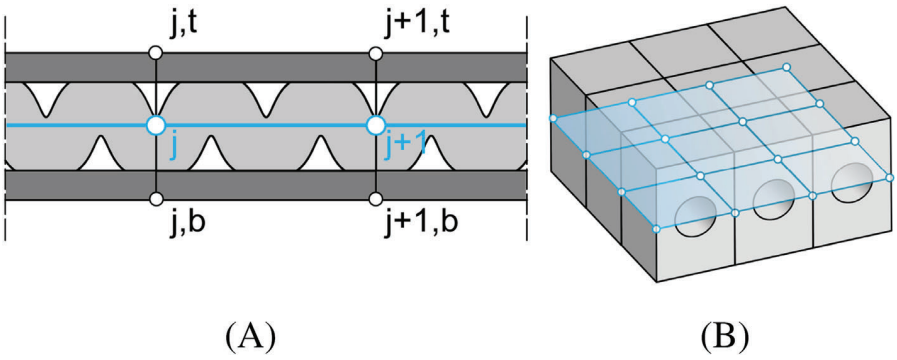

FIGURE 4 Beams (A) and plate (B) macroelements condensed to midplane

$$\text{for plates: } \boldsymbol{u}^H = \sum_{j=1}^{N_{\text{nodes}}} (\boldsymbol{\phi}_{j,bz} u_{j,bz} + \boldsymbol{\phi}_{j,bx} u_{j,bx} + \boldsymbol{\phi}_{j,by} u_{j,by} + \boldsymbol{\phi}_{j,tz} u_{j,tz} + \boldsymbol{\phi}_{j,tx} u_{j,tx} + \boldsymbol{\phi}_{j,ty} u_{j,ty}), \tag{21}$$

where N_{nodes} is a number of united edge nodes.

In order to improve the accuracy of the analysis and potentially increase the rate of convergence during the iterative correction of a multiscale solution, we expand the $\boldsymbol{V}^H$ space and include nonlinear basis functions of the hierarchical type. The approach is inspired by the higher-order FEM approach.[30] The very concept of the hierarchic base is to increase the order of approximation by adding new shape functions that do not alter the lower-order shape functions. In the case of MsFEM, it becomes a highly desirable property of this approach since no recalculation of the existing shape functions is needed in the case of refinements.

Hierarchical functions can be generated by using the integrated Legendre polynomials (see, e.g., Reference 31, eq. (8.61)), that in interval $[0, 1]$ are of the form:

$$\psi_{p+1}(\xi) = \frac{1}{(p-1)!2^{2(p-1)}} \frac{\mathrm{d}^{p-1}}{\mathrm{d}\xi^{p-1}} \left[\left((2\xi - 1)^2 - 1 \right)^p \right], \quad p \geq 2, \ 0 \leq \xi \leq 1, \tag{22}$$

where p is the order of approximation. In Appendix B, we recapitulate the procedure for the calculation of boundary conditions $\boldsymbol{d}_k$ for higher-order multiscale approximation.

It is worth mentioning that at the macroscale level the proposed first-order approximation meets the plane cross-section Euler's hypothesis at the vertical edges and faces of macroelements only. This is not the case neither at other cross-sections nor for higher-order approximation. Furthermore, the multiscale shape functions do not reflect material distribution along Γ_i^D boundary, thus, we introduce a correction procedure that is the topic of the next two sections.

2.2 | Corrector problem

Let us consider support of basis functions of a given united edge node j, $\widetilde{\Omega}_j$ (see Figure 5). We can rewrite boundary value problem (1)–(3) and use already calculated solution $\boldsymbol{u}_{ms}$ to complete the corresponding right-hand sides (r.h.s.):

$$-\bigtriangledown \cdot \left(\boldsymbol{C}(\boldsymbol{x}) \bigtriangledown_s \boldsymbol{u}_{ms} \right) = \boldsymbol{f}_{ms}, \text{ in } \widetilde{\Omega}_j, \tag{23}$$

$$\boldsymbol{u}_{ms} = \boldsymbol{u}_{ms}|_{\widetilde{\Gamma}_j^D}, \text{ on } \widetilde{\Gamma}_j^D, \tag{24}$$

$$\boldsymbol{t}_{ms} = \boldsymbol{t}_{ms}|_{\widetilde{\Gamma}_j^N}, \text{ on } \widetilde{\Gamma}_j^N. \tag{25}$$

Note that the r.h.s. are marked with ms index and typically differ from the original problem r.h.s.. The exact solution $\boldsymbol{u}$ is the sum of the multiscale solution and some unknown term $\boldsymbol{u}_c$, a local corrector:

$$\boldsymbol{u} = \boldsymbol{u}_{ms} + \boldsymbol{u}_c. \tag{26}$$

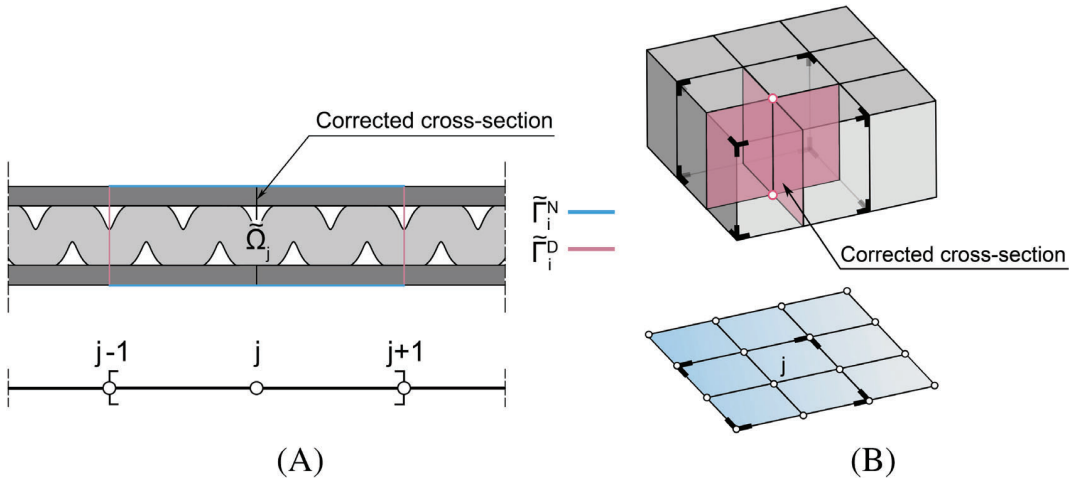

FIGURE 5 Corrected domains in beams (A) and plates (B) (bottom is a midplane representation of the conjugated nodes)

By linearity of the problem $\boldsymbol{u}_c$ satisfies the following equations:

$$-\nabla\cdot\left(\boldsymbol{C}(\boldsymbol{x})\nabla_s\boldsymbol{u}_c\right)=\boldsymbol{f}-\boldsymbol{f}_{ms},\ \text{in}\ \widetilde{\Omega}_j, \tag{27}$$

$$\boldsymbol{u}_c=\boldsymbol{u}-\boldsymbol{u}_{ms},\ \text{on}\ \widetilde{\Gamma}_j^D, \tag{28}$$

$$\boldsymbol{t}_c=\hat{\boldsymbol{t}}-\boldsymbol{t}_{ms},\ \text{on}\ \widetilde{\Gamma}_j^N. \tag{29}$$

Since we are correcting the solution in the support of the j node basis functions and we do not want to disturb the solution in the adjacent macroelements, we will assume that $\boldsymbol{u}_c=\boldsymbol{0}$ on the edge $\widetilde{\Gamma}_j^D$.

The weak formulation of the corrector problem is as follows:

Find displacement $\boldsymbol{u}_c\in\boldsymbol{V}(\widetilde{\Omega}_j)$, $\boldsymbol{u}_c=0|_{\widetilde{\Gamma}_j^D}$ *in domain* $\widetilde{\Omega}_j$ *such that:*

$$\int_{\widetilde{\Omega}_j}\nabla\boldsymbol{v}\cdot\left(\boldsymbol{C}(\boldsymbol{x})\nabla_s\boldsymbol{u}_c\right)\mathrm{d}\Omega=\left(\int_{\widetilde{\Omega}_j}\boldsymbol{v}\cdot\boldsymbol{f}\mathrm{d}\Omega+\int_{\widetilde{\Gamma}_j^N}\boldsymbol{v}\cdot\hat{\boldsymbol{t}}\mathrm{d}\Gamma\right)-\left(\int_{\widetilde{\Omega}_j}\boldsymbol{v}\cdot\boldsymbol{f}_{ms}\mathrm{d}\Omega+\int_{\widetilde{\Gamma}_j^N}\boldsymbol{v}\cdot\boldsymbol{t}_{ms}\mathrm{d}\Gamma\right),\quad\forall\boldsymbol{v}\in\boldsymbol{V}. \tag{30}$$

The r.h.s. represents the residuum of the problem that is driving the corrector problem. The problem is solved on the fine mesh and is the solution of the following system of algebraic equations:

$$\widetilde{\boldsymbol{K}}_j^h\boldsymbol{u}_j^c=\widetilde{\boldsymbol{f}}_j^h-\widetilde{\boldsymbol{f}}_j^{h,ms}=\widetilde{\boldsymbol{r}}_j, \tag{31}$$

where $\widetilde{\boldsymbol{K}}_j^h$ and $\widetilde{\boldsymbol{f}}_j^h$ matrices and vectors, respectively, assembled on $\widetilde{\Omega}_j$ and $\boldsymbol{f}_i^{h,ms}=\boldsymbol{K}_i^h\boldsymbol{u}_i^{ms}$ in a single macroelement Ω_i.

It is worth noting that the proposed domains $\widetilde{\Omega}_j$ of patches of macroelements are the only feasible choice due to fact that the residuum is not equal to zero only on the interfaces between macroelements. To prove this, lets us analyze residuum inside a single macroelement Ω_i:

$$\boldsymbol{r}=\boldsymbol{f}-\boldsymbol{f}_{ms}=\boldsymbol{f}+\nabla\cdot\left(\boldsymbol{C}(\boldsymbol{x})\nabla_s\boldsymbol{u}_{ms}\right)=\boldsymbol{f}+\nabla\cdot\left(\boldsymbol{C}(\boldsymbol{x})\nabla_s(\boldsymbol{u}^H+\boldsymbol{u}_b)\right). \tag{32}$$

The function $\boldsymbol{u}^H$ is a linear combination of multiscale shape functions generated by solving problem (12)–(14) with zero body forces and traction, hence it does not contribute to the residuum. The only contributor is the bubble part $\boldsymbol{u}_b$ that yields body forces equal to $\boldsymbol{f}$ from (9), thus the residuum is equal to zero. Analogously, residual traction forces along Γ_i^N are equal to zero. Therefore, the current $\boldsymbol{u}_{ms}$ multiscale solution satisfies (1) and (3) inside element domains Ω_i and Γ_i^N, but not on macroelement interfaces. Where the solution itself is continuous between macroelements, its gradient is not. Therefore, this residuum is a loading distributed along the coarse mesh vertical interfaces.

One can also notice that the presented corrector term is an approximation of the error and is computed similarly as in the implicit error estimation method,[32] particularly in the subdomain version. In MsFEM the subdomains are the macroelement patches.

2.3 | Iterative scheme

In order to reduce error due to the assumptions involved in choosing local kinematic boundary conditions when building multiscale basis function, the correction function $\boldsymbol{u}_c$ is added to the multiscale basis functions. This allows for recalculation of the coarse mesh problem and correction of the multiscale solution in an iterative manner. The basis of the corrector scheme[12] can be summarized as follows: (I) define local corrector domains, (II) compute a series of local corrector problems and update multiscale basis functions, (III) recalculate coarse mesh problem with the newly updated multiscale basis functions, and (IV) repeat the process until the residuum is small enough. The corrections may also be performed adaptively, that is, in regions with high residuum. The scheme was proven theoretically[12] to converge to the best possible fine-mesh solution and was shown to work on numerical examples.

In the beam and plate problems, no simple addition of $\boldsymbol{u}_c$ to a multiscale basis function can be performed because there are multiple multiscale basis functions in a single corrector region. Authors of the original scheme[12] proposed two strategies in this case: spreading the correction function between existing basis functions or introducing a new corrector degree of freedom for each corrector domain. The first approach involves the introduction of troublesome splitting rules that have a negative effect on the convergence of the method. An additional corrector degree of freedom at each coarse mesh node allows converging significantly faster as stated by the authors. We will adapt the second option of adding corrector dofs and tie it with the united edge nodes of the midplane that we will briefly cover here.

Before initiating the corrector scheme, a corrector basis function $\boldsymbol{\phi}_{j,c}$ and a coefficient $u_{j,c}$ are defined for every corrector domain of united edge node j (see Figure 6), and $\boldsymbol{\phi}_{j,c} = \mathbf{0}$ and $u_{j,c} = 1$. In plates, the choice of the corrector domains (patches of macroelements) may differ and influences the convergence rates. In this article, all numerical experiments were performed with the corrector domains associated with supports of basis functions of the united edge nodes. Thus, the global solution $\boldsymbol{u}^H$ for beams reads:

$$\boldsymbol{u}^H = \sum_{j=1}^{N_{\text{nodes}}} (\boldsymbol{\phi}_{j,bz} u_{j,bz} + \boldsymbol{\phi}_{j,bx} u_{j,bx} + \boldsymbol{\phi}_{j,tz} u_{j,tz} + \boldsymbol{\phi}_{j,tx} u_{j,tx} + \boldsymbol{\phi}_{j,c} u_{j,c}), \tag{33}$$

and for plates it can be written analogically.

The corrector scheme begins by updating the corrector basis functions in the following way:

$$\boldsymbol{\phi}_{j,c}^{\text{new}} = \boldsymbol{\phi}_{j,c} u_{j,c} + \boldsymbol{u}_c, \tag{34}$$

and setting a new coefficient $u_{j,c}^{\text{new}} = 1$.

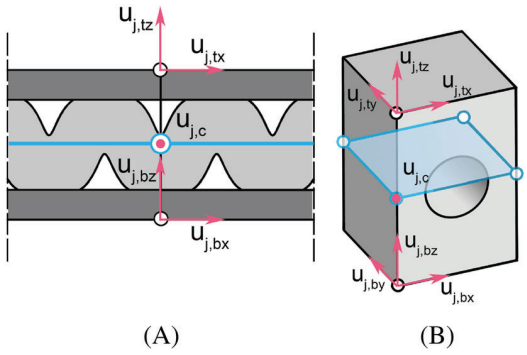

FIGURE 6 Corrector degrees of freedom in beams (A) and plates (B)

After the corrections to the basis functions are done, the coarse mesh problem is solved again starting from the prolongation of macroelement matrices in (16) including new corrector dofs and functions for every macroelement. Then after assembling the algebraic system of Equation (17), it is solved for vector $\boldsymbol{u}^H$, which includes new values of coefficients $u_{j,c}$. The new upscaled solution is obtained and the next iteration of the corrector scheme can be initiated.

Each corrector problem is driven by the current residual and therefore depends on the computation of the source term $\widetilde{\boldsymbol{f}}_i^{h,ms}$ of the current multiscale solution $\boldsymbol{u}_{ms}$. Update of $\boldsymbol{\phi}_{i,c}$ basis function depends on the sequence of corrections and therefore creates race conditions. In order to parallelize the process, patterns with nonoverlapping corrector regions can be easily adapted into the scheme. In the scope of this article, we did not thoroughly test the influence of a sequence of corrections on convergence that may be the subject of future work.

MsFEM with the iterative scheme presented here for the linear problem of elasticity can be extended to nonlinear problems as, for example, in Reference 21, where the method was applied in the framework of elastic-visco-plasticity. Moreover, the original residual-driven MsFEM corrector scheme was efficiently extended to nonlinear problems in Reference 33, in such a way that the iterative correction does not increase the overall computational cost of nonlinear MsFEM analysis. The main difficulty for our approach will be keeping orthogonality of the multiscale basis functions, the corrector basis functions, and the bubble solutions.

2.4 | Upscaling of the kinematic boundary conditions

The coarse-scale beam or plate supports, fixed or pinned, and pointwise loads have to be appropriately represented in the fine 2D or 3D domain. The loading has to be distributed on a small area and the displacement conditions have to be interpolated using multiscale basis functions, bubble part, and correction function.

In the case of the fixed or sliding support at the given coarse node, we simply set the corresponding entries of vector $\boldsymbol{u}^H$ as equal to zero.

For the pinned support, we assume that the coarse mesh fits the support location, the corresponding dofs, for example, $u_{j,bz}$ and $u_{j,bx}$ for beams as shown in Figure 7, equals to zero, and the zero displacement on a small segment is assumed in problems (12)–(14) and (9)–(11). This way the support condition is built into the multiscale shape functions. In an iterative scheme, the same boundary conditions in the corrector problem are imposed.

3 | NUMERICAL EXPERIMENTS

In this section, five examples of various beams and plates are presented. The objective of this study is to examine the capability of the modified MsFEM to model complex structural elements and show the efficiency of the iterative procedure. The examples include a simply supported homogeneous beam, a sandwich beam, a multispan beam with irregular structure, a concrete reinforced slab, and a sandwich panel with the dual corrugated high-density fiberboard (HDF) core.

The results obtained by the multiscale method $\boldsymbol{u}_{ms}$ are compared with these obtained using FEM and a very fine mesh called the reference solution $\boldsymbol{u}_{\mathrm{FEM}}$. The comparison of the FEM and MsFEM solutions enables computation of the additional modeling error $\boldsymbol{e}^m$ introduced by the multiscale method:

$$\boldsymbol{e}^m = \boldsymbol{u}_{\mathrm{FEM}} - \boldsymbol{u}_{ms}. \tag{35}$$

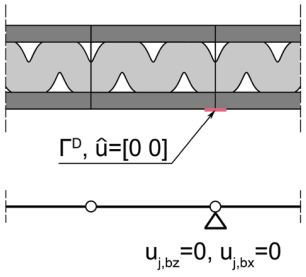

FIGURE 7 A pinned support in a beam and its two-dimensional representation (red segment)

This error is measured in the L_2 norm:

$$||\boldsymbol{e}^m|| = \left[\int_\Omega \boldsymbol{e}^m \cdot \boldsymbol{e}^m \mathrm{d}\Omega\right]^{\frac{1}{2}}. \tag{36}$$

Convergence diagrams shown in this section present the relative error, that is:

$$\eta = \frac{||\boldsymbol{e}^m||}{||\boldsymbol{u}_{\mathrm{FEM}}||}. \tag{37}$$

3.1 | Beam examples

Example 1. In the first simple example, we compare results of the MsFEM analysis and the analytic formula of deflection of a homogeneous simply supported beam carrying a uniformly distributed transverse load $t = -10\frac{\mathrm{kN}}{\mathrm{m}}$. The beam has length $L = 300$ mm and the rectangular cross-section with depth $h = 50$ mm and width $b = 10$ mm. We assumed Young's modulus $E = 210$ GPa and Poisson's ratio of 0.3. The closed formula of deflection of the neutral axis of a simply supported Timoshenko beam[34] is:

$$w_a(x) = \frac{tL^4}{24EI}\left[\left(\left(\frac{x}{L}\right)^4 - \frac{3}{2}\left(\frac{x}{L}\right)^2 + \frac{5}{16}\right) - \left(\frac{h}{L}\right)^2 \frac{2(1+\mu)}{k}\left(\left(\frac{x}{L}\right)^2 - \frac{1}{4}\right)\right], \quad -\frac{L}{2} \le x \le \frac{L}{2}, \tag{38}$$

where $k = \frac{5}{6}$, $\mu = 0$, and $I = \frac{bh^3}{12}$ for the rectangular cross-section. The plane stress state was assumed for the numerical analysis. The domain was discretized with six macroelements with fine meshes of 335 fine linear triangular elements and 386 dofs each. The pinned supports were modeled by 2 mm long segments with either zero displacement or symmetry boundary condition.

The comparison of the deflections obtained using MsFEM with linear multiscale functions, FEM on the fine mesh, and the theoretical formula are presented in Figure 8. The maximum deflection and general shape of the deflection of the homogeneous beam are predicted with a good accuracy by MsFEM adapted to a beam analysis. The observed discrepancies result from different mathematical models and the number of dofs in numerical models.

Example 2. In the second example, we study more thoroughly a convergence of the MsFEM results to the reference fine-mesh solution. We consider a cantilever sandwich beam shown in Figure 9, similar to the three-layer beam analyzed in Reference 29. The beam is 1 m long, with width and depth of 100 mm. The beam is made of two aluminum panels of

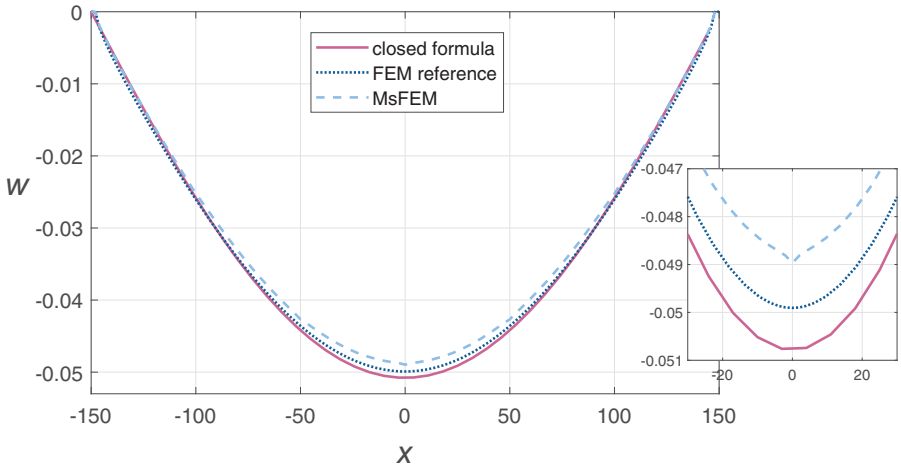

FIGURE 8 Comparison of the deflection obtained by the closed formula,[34] FEM, and MsFEM. MsFEM, multiscale finite element method

15 mm thickness with Young's modulus of 70, 000 MPa and Poisson's ratio of 0.33. The core with hollows is made of epoxy with Young's modulus of 4350 MPa and Poisson's ratio of 0.3679. The beam is subjected to constant distributed loading of 0.5 $\frac{\text{kN}}{\text{m}}$ applied on the top edge. The plane stress state was assumed for numerical analysis. The domain was discretized with 10 repeating macroelements refined with the auxiliary meshes of 968 fine linear triangular elements and with 1116 dofs each.

Figure 10 presents the convergence of the corrector scheme for various orders of approximation $p = 1 - 5$. In all cases, we observe that the iterative method converges the reference solution up to the machine precision. In the case of linear basis functions, this level of accuracy is achieved after six iterations. By enriching the space of multiscale basis functions we see that the rate of convergence increases significantly. When using the multiscale basis functions of order 5 the fine-mesh solution is achieved after only three iterations. We can see that after one iteration with linear functions we reduce error from 10^{-1} to 10^{-2}. However, using multiscale basis functions of $p = 5$ the error is reduced by up to four orders of magnitude in only one step of iteration (from 10^{-2} to 10^{-6}).

The increase of the order of approximation reduces the error even without the iterative scheme that is shown in Figure 11(A). In this example, the error drops significantly after adding basis functions of odd orders. This effect can be explained by examining the juxtaposition of shape function $\boldsymbol{\phi}_{2,3x}$ and the fine-mesh solution (see Figure 11B). The odd antisymmetric polynomials indeed fit the solution very well. That is not the case for even-order polynomials. We also compared these functions with corrector shape function $\boldsymbol{\phi}_{2,c}$ generated after six iterations of the MsFEM solution with linear basis functions.

Using this example we also studied the influence of the application of the Neumann boundary conditions during the generation of the multiscale shape functions. In the standard MsFEM analysis the Dirichlet boundary conditions

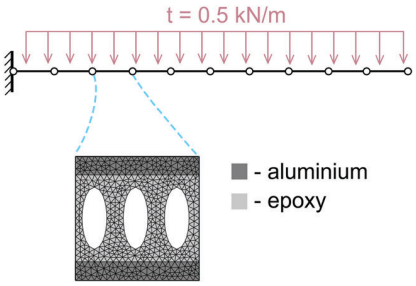

FIGURE 9 Cantilever beam, coarse element, and the fine mesh

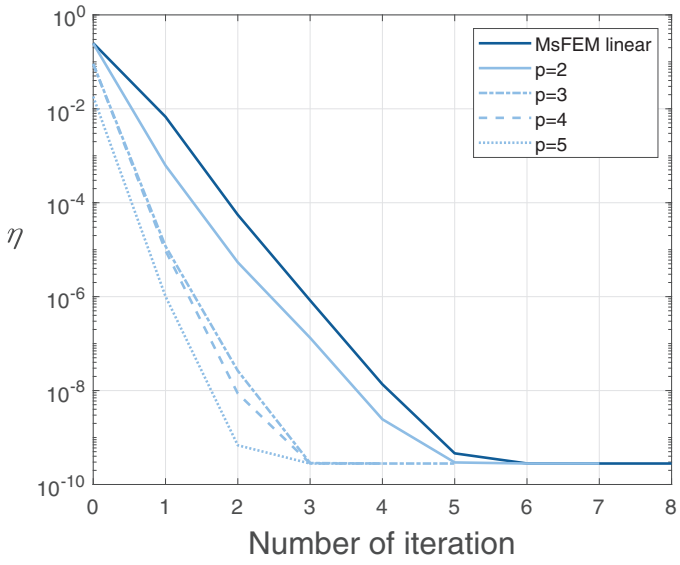

FIGURE 10 Cantilever beam. Convergence of the corrector scheme for different coarse scale approximation orders

defined by Equation (13) are assumed on the whole macroelement boundary Γ_i, as shown previously in section 2.1 in the example in Figure 3(A). Figure 12 presents a convergence of iterative scheme with multiscale functions either build using only the Dirichlet boundary conditions or both the Neumann and Dirichlet ones. The initial errors were 37% and 25%, respectively. Furthermore, six iterations instead of 16 are needed to reach the reference solution when the Neumann boundary conditions are built in.

Example 3. We examine a multispan beam with an irregular structure that can be manufactured in the computerized numerical control milling process (see Figure 13). The example is a showcase of unclear scale separation and missing periodicity assumption that can be a result of, for example, optimization procedures. The structure is composed of 17 cells of three types, with varied bracing. The dimensions of the cells are 100 mm × 100 mm with a depth of 50 mm. The whole beam has a length of 1.7 m and is fixed at the left end and roller supported at 0.8 and 1.4 m. We assume steel as the base material with Young's modulus of 210 GPa and Poisson's ratio of 0.3. Uniformly distributed load of 2 $\frac{\text{kN}}{\text{m}}$ is applied on the top edge. Each cell was a macroelement in MsFEM with individual fine meshes.

The results of the analysis of the beam are presented in the convergence plots in Figure 14. Similar observations can be made as in the previous example. With linear basis functions, we achieve the fine-mesh solution in the iterative process of 15 corrections starting from $\eta = 6.81\%$. As previously indicated, after enriching the basis space we reduce the initial error and increase the rate of convergence.

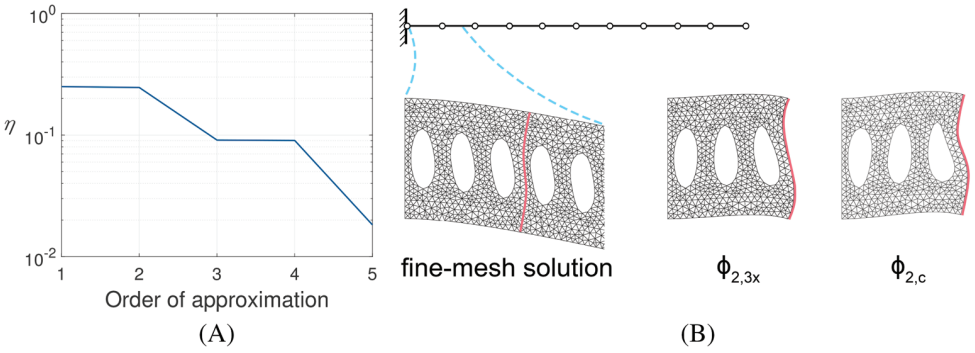

FIGURE 11 Convergence of the multiscale finite element method error for increasing order of approximation (A), juxtaposition of the fine-mesh solution, the shape function $\boldsymbol{\phi}_{2,3x}$, and the corrector shape function $\boldsymbol{\phi}_{2,c}$ (B)

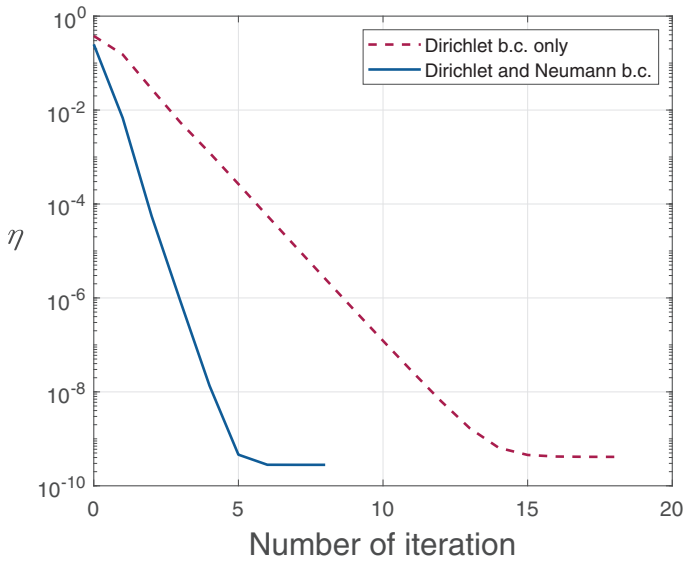

FIGURE 12 Convergence of relative error in analysis with the standard multiscale finite element method basis functions (Dirichlet boundary conditions) and basis functions proposed by us (Dirichlet and Neumann boundary conditions)

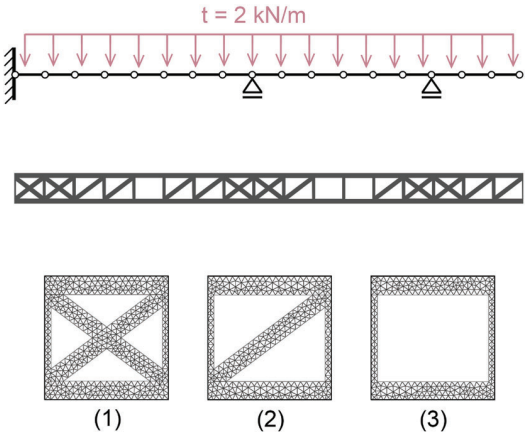

FIGURE 13 Multispan beam model and macroelement types with fine meshes. Beam arranged from macroelements in order: [1, 1, 2, 2, 3, 2, 2, 1, 1, 2, 3, 3, 2, 1, 1, 2, 2]

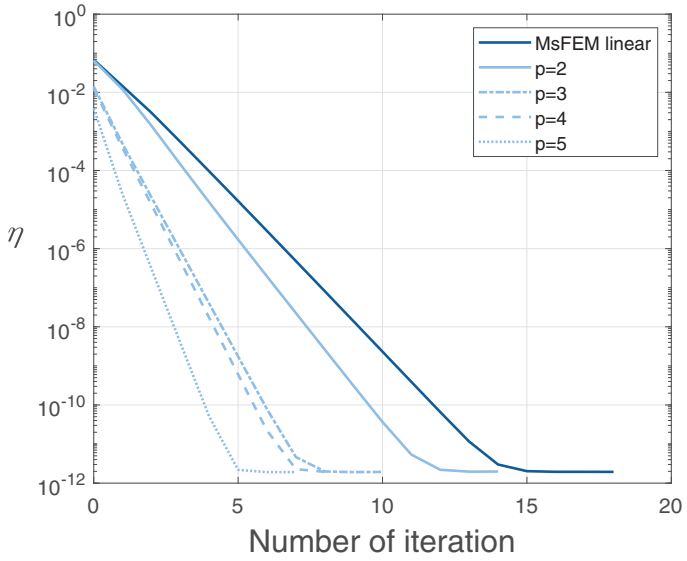

FIGURE 14 Multispan beam. Convergence of the corrector scheme for different coarse scale approximation orders

Figure 15 depicts the L_2 norm of the FEM approximation using the residuum entries as dofs of MsFEM solution with linear basis functions and the solution after first and second correction. As described in section 2.2 the residuum is not equal to zero only on Γ_i^D boundary of macroelements that correlates with the results shown here. In the initial solution, the norm of the residuum reaches a magnitude of 21 $\frac{\text{MN}}{\text{m}}$ with peaks at the junction of susceptible macroelements of type 2 and stiff macroelements of type 3. During the correction procedures, the residuum is significantly reduced, almost not visible after second correction in the initial limits.

3.2 | Plate examples

Example 4. In this example, we analyze a 6 m × 6 m rectangular concrete reinforced slab with a uniformly distributed load of $20\frac{\text{kN}}{\text{m}^2}$ on the top surface. The slab edges are fixed. Figure 16(A) depicts one section of the slab with top and bottom reinforcements (ϕ 10 mm bars) and hollow concrete filling. The material properties are as follows: concrete Young's modulus is 70 GPa and Poisson's ratio is 0.2, reinforcement Young's modulus is 210 GPa and Poisson's ratio is 0.3.

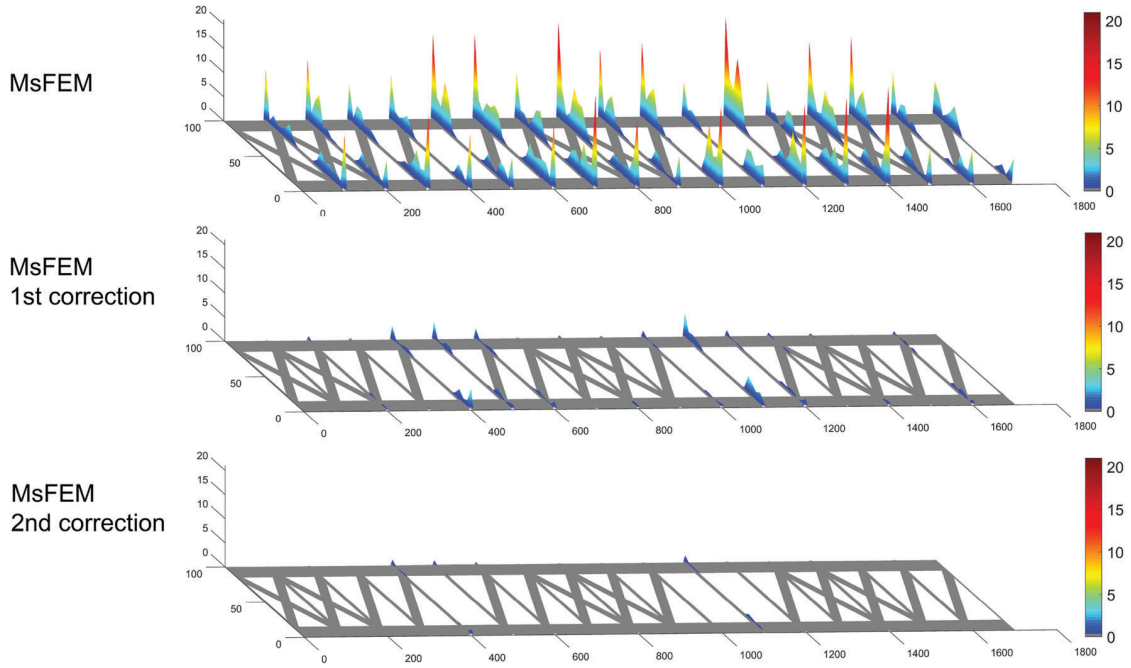

FIGURE 15 Norm of the residuum $\left(\frac{\mathrm{MN}}{\mathrm{m}}\right)$

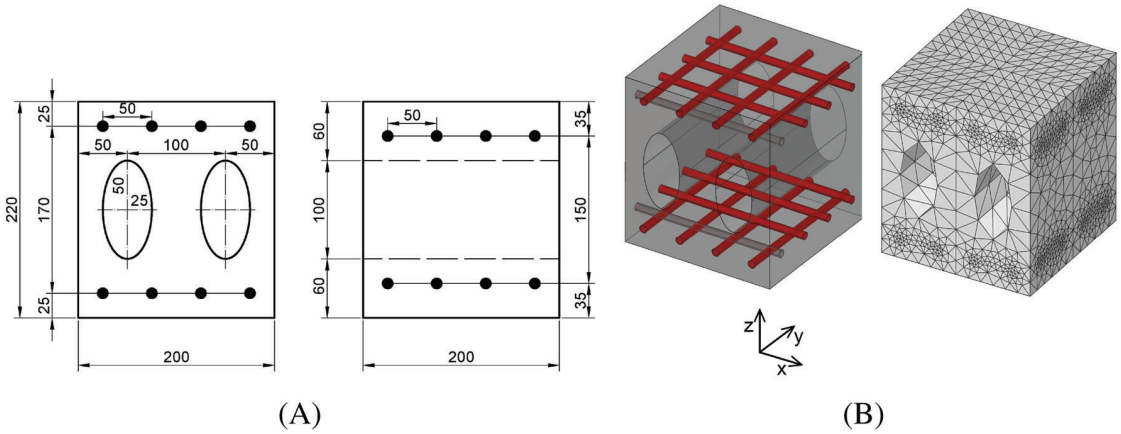

FIGURE 16 Dimensions of repeating section of the reinforced slab: (A) Side views, (B) 3D view and the fine mesh

By the symmetry of the problem, only one-quarter of the whole problem is analyzed. The coarse mesh consists of 15 × 15 square macroelements. Each macroelement was divided into 102,972 fine elements with 54,849 dofs (see Figure 16B). The number of dofs in the MsFEM analysis with linear basis functions and with corrector dofs is 1792, while in the reference model is about 19 million (19,045,800 exactly).

Figure 17 illustrates the convergence of the MsFEM solution with the increasing number of corrections for the different initial multiscale basis functions. Although changes in the rate of convergence are less prominent with the increase of the order of approximation than in the previous examples, the error is still reduced significantly for higher p. The number of dofs for $p = 2$ equals 6880 and for $p = 3$ equals 14,848. With respect to the reference fine mesh, this increase in dofs is still insignificant and compensated by the error reduction.

The stress distribution is shown in Figure 18. We can compare the reference von Mises stresses in the concrete and the top reinforcement with the results obtained by MsFEM with linear multiscale basis functions without correction and corrected one and three times. We observe a significant difference between the initial uncorrected solution and the fine-mesh

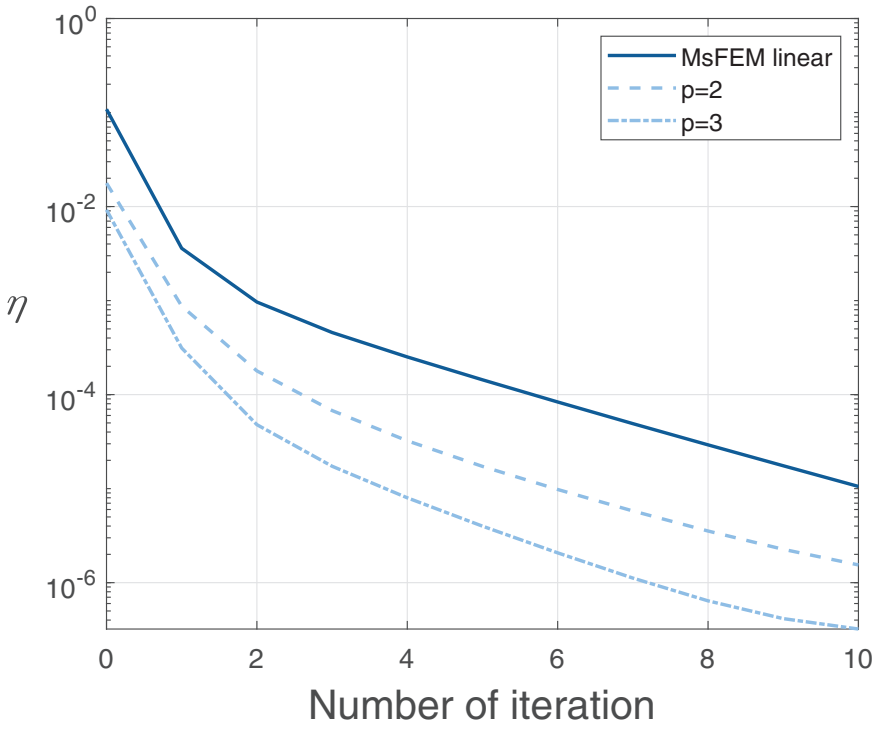

FIGURE 17 Concrete reinforced slab. Convergence of the corrector scheme for different coarse scale approximation orders

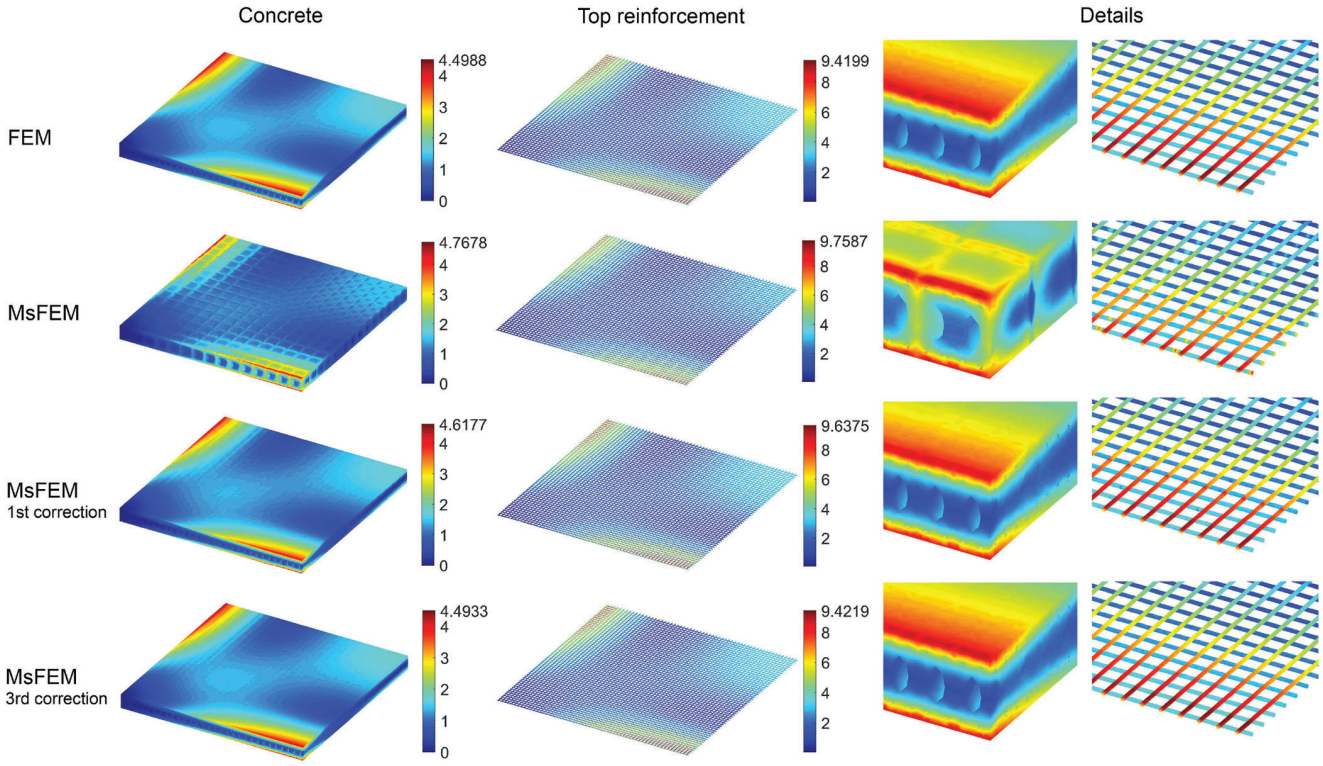

FIGURE 18 Example 4: The Von Mises stresses (MPa) calculated directly using the fine mesh (19 millions dofs), by MsFEM without correction, and with one and three corrections (1792 dofs). MsFEM, multiscale finite element method

solution. The MsFEM solution features artificial peaks of stresses between macroelements that can be explained by a large residuum. But, MsFEM with iterative correction leads to stresses distributions that are much closer to the reference one. This correlates with the L_2 norm error from the convergence plot. After the third correction, the stress plots are almost identical to the reference solution with the peak values of the stresses matching up to the third digit.

We have also compared the computational costs of direct FEM and proposed modified MsFEM solutions. The computations were done on a server with four Intel Xeon Gold 5120 (2,20 GHz, 14 cores) processors. The reference FEM solution was obtained with MATLAB Partial Differential Equation Toolbox and took 3644 s. The MsFEM solution with linear multiscale basis functions took only 22 s (166 times faster) and yielded 11% relative error. MsFEM with a single iteration of the correction performed for the whole domain took 485 s (7.5 times faster) and yielded 0.3% relative error. The multiscale shape functions, as well as the corrector problems in the iterative scheme, were computed in parallel. Such high efficiency of MsFEM without correction was possible due to the reuse of the stiffness matrix in repeating macroelement. Iterations of the corrector scheme are expensive, however, they can be carried out only in the regions with high residuum rather than in the whole domain.

Example 5. Our last example is the sandwich panel with a dual corrugated HDF core subjected to bending. Its complex geometry is presented in Figure 19. The panel was analyzed by the RVE based homogenization in Reference 8. The numerical results were compared with the experimental data. The experiment consisted of tensile tests to determine elastic properties of the facing and the core materials as well as series of one-point bending tests of assembled HDF sandwich panels. Elastic properties were determined for HDF facing panel: Young's modulus of 5457 MPa, Poisson's ratio of 0.33, and for core: Young's modulus of 5457 MPa, Poisson's ratio of 0.33. Samples for bending tests were cut out in a shape presented in Figure 20(A), whereas Figure 20(B) presents the setup of the bending test. The samples were subjected to a load applied with a constant velocity until failure. The force of $P = 307.66$ N was found to be the elastic limit with the corresponding deflection of the sample of 2.67 mm.

The MsFEM numerical analysis was conducted for half of the original problem due to the symmetry of the problem as shown in Figure 21. The model was divided into 2×7 macroelements of two types. The half to the force P was applied on the surface of the size of 1.2 mm $\times$ 50 mm (size of one element of the fine mesh in y direction). The roller support was modeled as a fixed boundary in x and z directions on the surface of size of 2.4 mm $\times$ 50 mm in the location between two macroelements on the bottom facing panel.

Figure 22 presents maximum deflection versus load graphs for the experiment, the MsFEM solution obtained with linear basis functions, and its first correction. The uncorrected MsFEM solution predicts a stiffer response to the load than the actual sample in the experiment exhibited. The relative difference of the computed and measured maximum deflections for MsFEM was 30.9%, while after performing one correction it was reduced to 1.2%. This was achieved with 165 dofs (including corrector dofs). The RVE based solution[8] yielded a solution discrepancy of 11.7% and it was obtained using 136,583 dofs.

Figure 23 presents the distribution of σ_{yy} stresses component for both the MsFEM analysis and after the first correction. As in the previous example, only one correction smooths the large incorrect stress between macroelements sufficiently allowing for investigation of stress concentration at the core-facing interfaces that may be crucial in the designing processes.

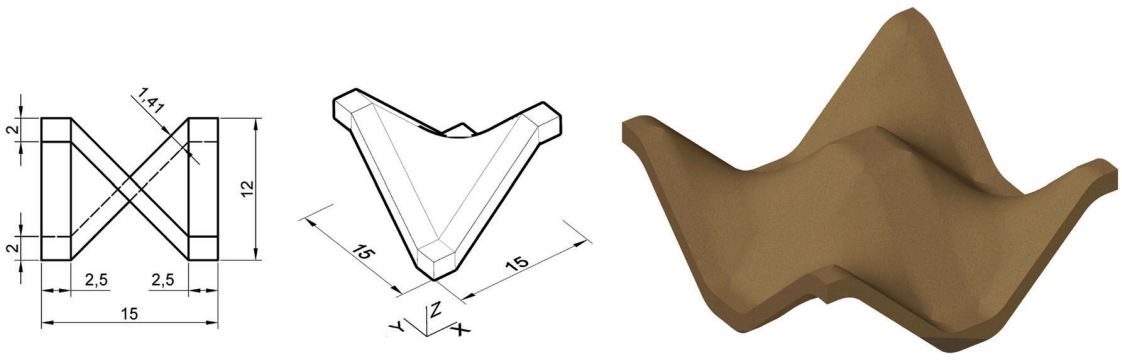

FIGURE 19 Dimensions and shape of a core of the high-density fiberboard sandwich panel

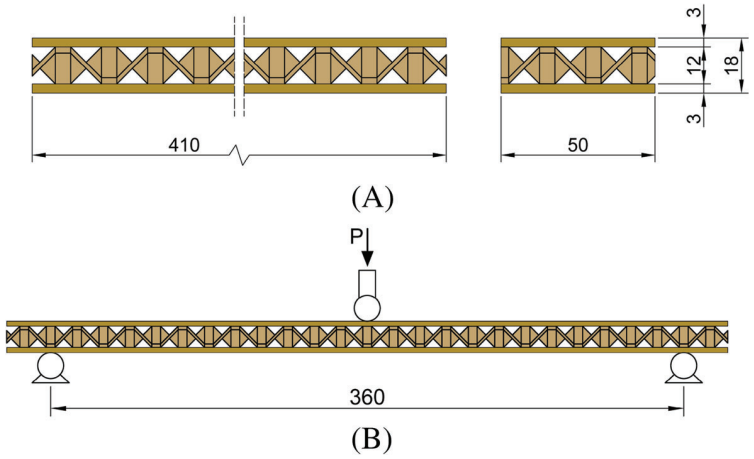

FIGURE 20 Sandwich panel specimen dimensions (A) and setup of the bending test (B)

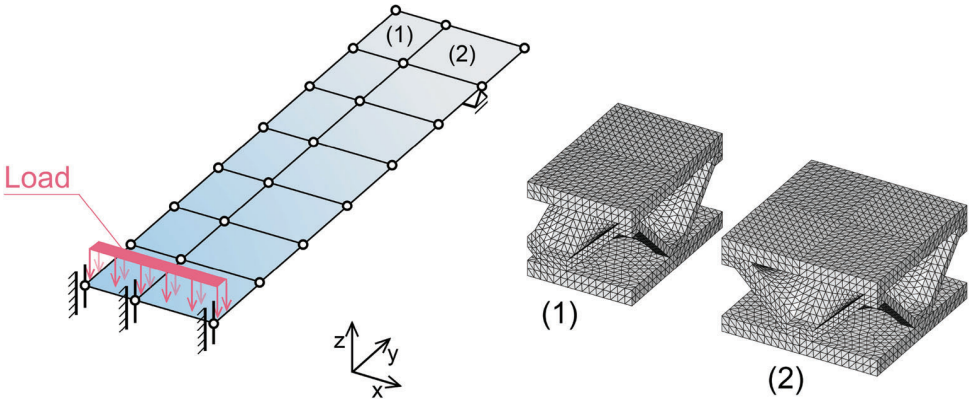

FIGURE 21 Multiscale finite element method discretization with the fine mesh of two macroelement types

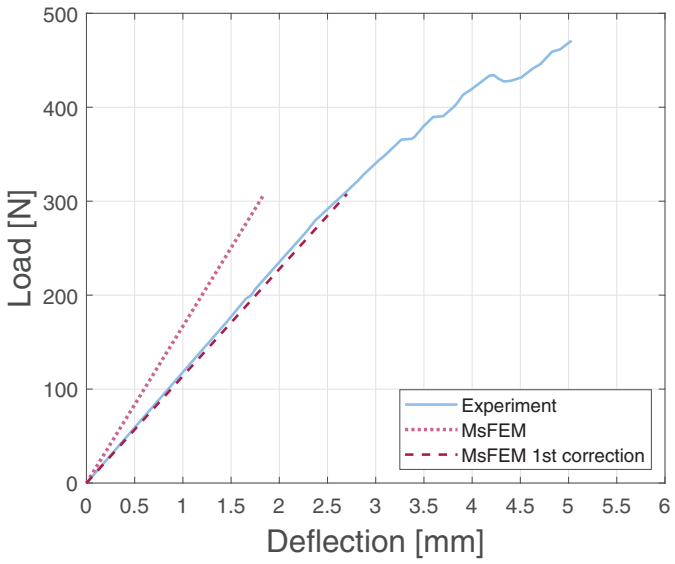

FIGURE 22 Load versus deflection curves

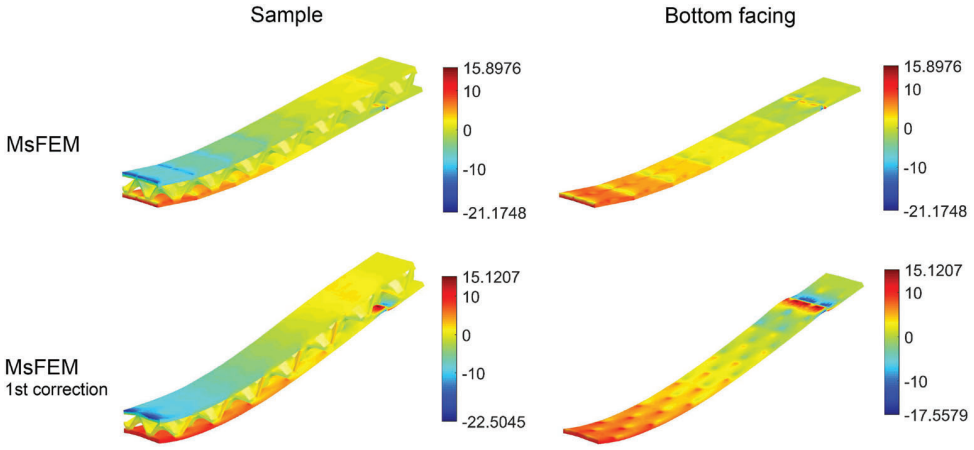

FIGURE 23 Example 5: σ_{yy} stresses component (MPa) and deflection obtained by MsFEM with linear shape functions and MsFEM after the first correction. Deflection scaled 30 times. MsFEM, multiscale finite element method

4 | CONCLUSIONS

An adaptation of the MsFEM to the analysis of sandwich beams and plates was addressed in this article. We incorporate the fine-scale boundary conditions of both kinematic and static types into the coarse-scale shape functions. The presented examples show a significant improvement of the MsFEM results, especially with the use of the corrector scheme[12] and the higher-order hierarchical multiscale functions in the analysis. Due to the higher-order approximation, only one layer of the coarse elements can be used reducing their number and simplifying the algorithm by using the united edge nodes.

The original iterative method[12] can be numerically expensive because it is necessary to downscale the solution and solve corrector problems for each patch of macroelements in each iteration, but the proposed approach with higher-order functions gives a new possibility of reaching desired accuracy faster with a large reduction of the necessary number of dofs (even by four orders). In the case of periodicity, this approach provides outstanding benefits, when the shape functions are reused in repeated macroelements.

ACKNOWLEDGMENT
This work was supported by the project nr 2017/25/B/ST8/02752 funded by National Science Centre.

DATA AVAILABILITY STATEMENT
The data that support the findings of this study are available from the corresponding author upon reasonable request.

ORCID
Mateusz Dryzek https://orcid.org/0000-0003-3148-5517
Witold Cecot https://orcid.org/0000-0002-3257-5226

REFERENCES

1. Hou T, Wu X. A multiscale finite element method for elliptic problems in composite materials and porous media. *J Comput Phys*. 1997;134(1):169-189. https://doi.org/10.1006/jcph.1997.5682
2. Papanicolau G, Bensoussan A, Lions J. *Asymptotic Analysis for Periodic Structures*. Studies in Mathematics and Its Applications. Elsevier Science; 1978.
3. Feyel F, Chaboche JL. FE2 multiscale approach for modelling the elastoviscoplastic behaviour of long fiber SiC/Ti composite materials. *Comput Methods Appl Mech Eng*. 2000;183:309-330.
4. Terada K, Hirayama N, Yamamoto K, Muramatsu M, Matsubara S, Nishi SN. Numerical plate testing for linear two-scale analyses of composite plates with in-plane periodicity. *Int J Numer Methods Eng*. 2016;105(2):111-137. https://doi.org/10.1002/nme.4970
5. Moyeda C, Fish J. Multiscale analysis of solid, waffle, ribbed and hollowcore reinforced concrete slabs. *Comput Methods Appl Mech Eng*. 2019;348:139-156. https://doi.org/10.1016/j.cma.2019.01.022
6. Helfen CE, Diebels S. Computational homogenisation of composite plates: Consideration of the thickness change with a modified projection strategy. *Comput Math Appl*. 2014;67(5):1116-1129. https://doi.org/10.1016/j.camwa.2013.12.017

7. Sciegaj A, Grassl P, Larsson F, Runesson K, Lundgren K. Upscaling of three-dimensional reinforced concrete representative volume elements to effective beam and plate models. *Int J Solids Struct*. 2020;202:835-853. https://doi.org/10.1016/j.ijsolstr.2020.07.006
8. Smardzewski J, Jasińska D. Mathematical models and experimental data for HDF based sandwich panels with dual corrugated lightweight core. *Holzforschung*. 2017;71(3):265-273. https://doi.org/10.1515/hf-2016-0146
9. Jenny P, Lee S, Tchelepi H. Multi-scale finite-volume method for elliptic problems in subsurface flow simulation. *J Comput Phys*. 2003;187(1):47-67. https://doi.org/10.1016/S0021-9991(03)00075-5
10. Hou TY, Wu XH, Cai Z. Convergence of a multiscale finite element method for elliptic problems with rapidly oscillating coefficients. *Math Comput*. 1999;68(227):913-943. https://doi.org/10.1090/S0025-5718-99-01077-7
11. Efendiev Y, Ginting V, Hou T, Ewing R. Accurate multiscale finite element methods for two-phase flow simulations. *J Comput Phys*. 2006;220(1):155-174. https://doi.org/10.1016/j.jcp.2006.05.015
12. Nguyen LH, Schillinger D. A residual-driven local iterative corrector scheme for the multiscale finite element method. *J Comput Phys*. 2019;377(1):60-88. https://doi.org/10.1016/j.jcp.2018.10.030
13. Gao K, Fu S, Chung ET. A high-order multiscale finite-element method for time-domain acoustic-wave modeling. *J Comput Phys*. 2018;360:120-136. https://doi.org/10.1016/j.jcp.2018.01.032
14. Cecot W, Oleksy M. High order FEM for multigrid homogenization. *Comput Math Appl*. 2015;70(7):1391-1400. https://doi.org/10.1016/j.camwa.2015.06.024
15. Liu H, Sun X, Xu Y, Chu X. A hierarchical multilevel finite element method for mechanical analyses of periodical composite structures. *Compos Struct*. 2015;131:115-127. https://doi.org/10.1016/j.compstruct.2015.05.001
16. Degond P, Lozinski A, Muljadi B, Narski J. Crouzeix-Raviart MsFEM with bubble functions for diffusion and advection-diffusion in perforated media. *Commun Comput Phys*. 2013;17(4):1-23. https://doi.org/10.4208/cicp.2014.m299
17. Dryzek M, Cecot W. A coupling of multiscale finite element method and isogeometric analysis. *Int J Multisc Comput Eng*. 2020;18:439-454. https://doi.org/10.1615/IntJMultCompEng.2020034287
18. Casadei F, Rimoli J, Ruzzene M. A geometric multiscale finite element method for the dynamic analysis of heterogeneous solids. *Comput Methods Appl Mech Eng*. 2013;263:56-70. https://doi.org/10.1016/j.cma.2013.05.009
19. Liu H, Zhang H. An equivalent multiscale method for 2D static and dynamic analyses of lattice truss materials. *Adv Eng Softw*. 2014;75:14-29. https://doi.org/10.1016/j.advengsoft.2014.04.006
20. Oleksy M, Cecot W. Application of hp-adaptive finite element method to two-scale computation. *Arch Comput Methods Eng*. 2015;22(1):105-134. https://doi.org/10.1007/s11831-014-9109-9
21. Klimczak M, Cecot W. An adaptive MsFEM for nonperiodic viscoelastic composites. *Int J Numer Methods Eng*. 2018;114(8):861-881. https://doi.org/10.1002/nme.5768
22. Liu H, Wang Y, Zong H, Wang MY. Efficient structure topology optimization by using the multiscale finite element method. *Struct Multidiscipl Optim*. 2018;58(4):1411-1430. https://doi.org/10.1007/s00158-018-1972-9
23. Cecot W, Oleksy M. The discontinuous Petrov–Galerkin methodology for the mixed multiscale finite element method. *Comput Math Appl*. 2020. https://doi.org/10.1016/j.camwa.2020.09.013
24. Krówczyński M, Cecot W. A fast three-level upscaling for short fiber reinforced composites. *Int J Multisc Comput Eng*. 2016;15(1):19-34. https://doi.org/10.1615/IntJMultCompEng.2016018563
25. Zhang HW, Wu JK, Lü J, Fu ZD. Extended multiscale finite element method for mechanical analysis of heterogeneous materials. *Acta Mech Sin*. 2010;26(6):899-920. https://doi.org/10.1007/s10409-010-0393-9
26. Klimczak M, Cecot W. Towards asphalt concrete modeling by the multiscale finite element method. *Finite Elem Anal Des*. 2020;171:103367. https://doi.org/10.1016/j.finel.2019.103367
27. Fu P, Liu H, Chu X. An efficient multiscale computational formulation for geometric nonlinear analysis of heterogeneous piezoelectric composite. *Compos Struct*. 2017;167:191-206. https://doi.org/10.1016/j.compstruct.2017.02.005
28. Ye S, Xue Y, Xie C. Application of the multiscale finite element method to flow in heterogeneous porous media. *Water Resour Res*. 2004;40(9):1-10.
29. Zhang S, Yin J, Zhang H, Chen B. A two-level method for static and dynamic analysis of multilayered composite beam and plate. *J Comput Phys*. 2016;111:1-18. https://doi.org/10.1016/j.finel.2015.12.001
30. Zienkiewicz O, Gago JDS, Kelly D. The hierarchical concept in finite element analysis. *Comput Struct*. 1983;16(1):53-65. https://doi.org/10.1016/0045-7949(83)90147-5
31. Zienkiewicz O, Taylor R, Zhu J. 'Standard' and 'hierarchical' element shape functions: Some general families of C_0 continuity. In: Zienkiewicz O, Taylor R, Zhu J, eds. *The Finite Element Method Set*. Vol 4. 6th ed. Butterworth-Heinemann; 2005:103-137.
32. Grätsch T, Bathe KJ. A posteriori error estimation techniques in practical finite element analysis. *Comput Struct*. 2005;83(4):235-265. https://doi.org/10.1016/j.compstruc.2004.08.011
33. Nguyen H, Schillinger D. The multiscale finite element method for nonlinear continuum localization problems at full fine-scale fidelity, illustrated through phase-field fracture and plasticity. *J Comput Phys*. 2019;396:129-160. https://doi.org/10.1016/j.jcp.2019.06.058
34. Ike C. Timoshenko beam theory for the flexural analysis of moderately thick beams – variational formulation, and closed form solution. *Tecnica Italiana-Italian J Eng Sci*. 2019;63:34-45. https://doi.org/10.18280/ti-ijes.630105

How to cite this article: Dryzek M, Cecot W. The iterative multiscale finite element method for sandwich beams and plates. *Int J Numer Methods Eng*. 2021;122:6714-6735. https://doi.org/10.1002/nme.6808

APPENDIX A. MULTISCALE SHAPE FUNCTIONS CALCULATION

Let us consider a macroelement of a beam shown in Figure A1(A) with coarse mesh nodes $A,\ b,\ A,\ t,\ B,\ b$, and $B,\ t$ and midplane nodes A and B with corresponding x-coordinates (x_A) and (x_B). For simplicity, let us assume that global coordinate system (x, z) is leveled with the bottom edge of the beam macroelement. The multiscale shape functions of node A are calculated by imposing Dirichlet boundary conditions on Γ_i^D boundary, and can be described by the following functions:

$$\begin{aligned}
&\text{for } \boldsymbol{\phi}_{A,bz}: \quad d_{A,bz}(x,z) = \left[0 \quad \left(1-\frac{z}{h}\right)\left(\frac{x-x_B}{x_A-x_B}\right)\right],\\
&\text{for } \boldsymbol{\phi}_{A,bx}: \quad d_{A,bx}(x,z) = \left[\left(1-\frac{z}{h}\right)\left(\frac{x-x_B}{x_A-x_B}\right) \quad 0\right],\\
&\text{for } \boldsymbol{\phi}_{A,tz}: \quad d_{A,tz}(x,z) = \left[0 \quad \frac{z}{h}\left(\frac{x-x_B}{x_A-x_B}\right)\right],\\
&\text{for } \boldsymbol{\phi}_{A,tx}: \quad d_{A,tx}(x,z) = \left[\frac{z}{h}\left(\frac{x-x_B}{x_A-x_B}\right) \quad 0\right],
\end{aligned} \tag{A1}$$

where h is the height of the beam. The formulas for shape function associated with node B are derived by swapping coordinates between nodes A and B.

For plate problems, consider a macroelement of a plate shown in Figure A1(B). For clarity, we only present formulas for boundary conditions of shape functions associated with midplane coarse mesh node A. We assume that the global coordinate system (x, y, z) is leveled with the bottom surface of the plate. Node A is directly connected to nodes B and C. The x- and y-coordinates of nodes A and B are (x_A, y_A) and (x_B, y_B), respectively. Nodal displacement functions of face Γ_{AB} read:

$$\text{for node } A,b: \quad N_{AB,b}(x,y,z) = \left(1-\frac{z}{h}\right)\left(\frac{\sqrt{(x-x_B)^2+(y-y_B)^2}}{l_{AB}}\right), \tag{A2}$$

$$\text{for node } A,t: \quad N_{AB,t}(x,y,z) = \frac{z}{h}\left(\frac{\sqrt{(x-x_B)^2+(y-y_B)^2}}{l_{AB}}\right), \tag{A3}$$

where $l_{AB} = \sqrt{(x_A-x_B)^2+(y_A-y_B)^2}$ is a distance between the nodes A and B, and h is the height of the plate. The same formulas can be derived for face Γ_{AC} by swapping coordinates between nodes B and C. Dirichlet boundary conditions read:

$$\begin{aligned}
&\text{for } \boldsymbol{\phi}_{A,bz}: \quad d_{A,bz}(x,y,z) = \left[0 \;\; 0 \;\; N_{\alpha,b}(x,y,z)\right],\\
&\text{for } \boldsymbol{\phi}_{A,bx}: \quad d_{A,bx}(x,y,z) = \left[N_{\alpha,b}(x,y,z) \;\; 0 \;\; 0\right],\\
&\text{for } \boldsymbol{\phi}_{A,by}: \quad d_{A,by}(x,y,z) = \left[0 \;\; N_{\alpha,b}(x,y,z) \;\; 0\right],
\end{aligned} \tag{A4}$$

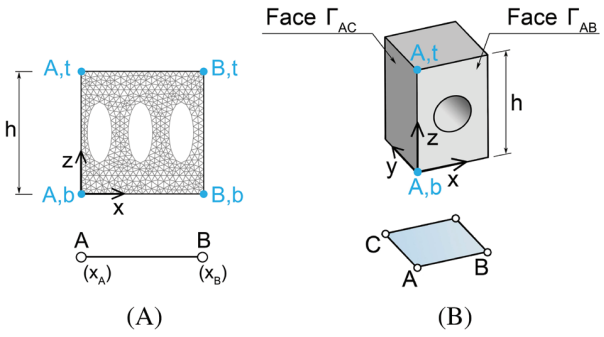

FIGURE A1 Macroelement of beam type (A) and plate type (B)

$$\begin{aligned}
&\text{for } \boldsymbol{\phi}_{A,tz}: \quad d_{A,tz}(x,y,z) = \left[0 \;\; 0 \;\; N_{\alpha,b}(x,y,z)\right],\\
&\text{for } \boldsymbol{\phi}_{A,tx}: \quad d_{A,tx}(x,y,z) = \left[N_{\alpha,b}(x,y,z) \;\; 0 \;\; 0\right],\\
&\text{for } \boldsymbol{\phi}_{A,ty}: \quad d_{A,ty}(x,y,z) = \left[0 \;\; N_{\alpha,b}(x,y,z) \;\; 0\right],
\end{aligned} \tag{A5}$$

where $\alpha = AB$ or AC, for faces Γ_{AB} or Γ_{AC}, respectively. For the remaining faces of Γ_i^D the Dirichlet boundary condition is equal to zero in all directions for these multiscale shape functions.

The presented approach is sufficient for the assumed geometry of macroelements with rectangular faces of Γ_i^D boundary. In the case where this assumption cannot be met, for instance, a plate with optimized height, a more general approach is required, which involves at least inversion of the bilinear interpolation. This problem will be addressed in future work.

APPENDIX B. HIGHER-ORDER MULTISCALE SHAPE FUNCTIONS CALCULATION

In beam example, higher-order hierarchic functions are associated with new coarse mesh edge nodes $A,\ p$ and $B,\ p$ as shown in Figure B1(A). Boundary conditions to generate higher-order multiscale shape functions for beam macroelements read:

$$\begin{aligned}
&\text{for } \boldsymbol{\phi}_{A,pz}: d_{A,pz}(x,z) = \left[0 \;\; \psi_{p+1}\left(\frac{z}{h}\right)\left(\frac{x-x_B}{x_A-x_B}\right)\right],\\
&\text{for } \boldsymbol{\phi}_{A,px}: d_{A,px}(x,z) = \left[\psi_{p+1}\left(\frac{z}{h}\right)\left(\frac{x-x_2}{x_1-x_2}\right) \;\; 0\right],
\end{aligned} \tag{B1}$$

where ψ is a higher-order hierarchical function in interval $[0, 1]$ (see Equation (22)) and p is the order of approximation. The reader can easily derive formulas for node B by swapping coordinates between nodes A and B.

To generate multiscale shape functions of higher-order in plate problems, nodes of edges and faces are added to the macroelement (see Figure B1B,C). New coarse mesh nodes $M,\ bp$, $M,\ pp$, and $M,\ tp$ are identified with the extra node M on the virtual mesh edge.

The multiscale shape functions of a higher-order associated with node A will be generated using the following edge displacement function:

$$\text{for node } A,p: \quad N_{AB,p}(x,y,z) = \psi_{p+1}\left(\frac{z}{h}\right)\left(\frac{\sqrt{(x-x_B)^2+(y-y_B)^2}}{l_{AB}}\right). \tag{B2}$$

The same formula can be derived for face Γ_{AC} by swapping coordinates between nodes B and C. Boundary conditions for corresponding functions are derived by applying the displacement in x, y, and z directions, as described previously, for example, in (A4).

The multiscale shape functions of higher-order associated with node M will be generated using the following edge and face displacement functions:

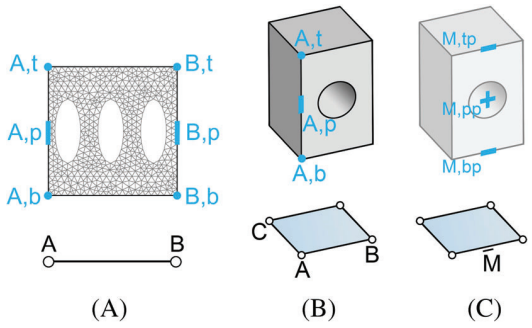

FIGURE B1 Higher-order macroelements of beam type (A), and plate type (B)–(C)

$$\text{for node } M, bp: \quad N_{AB,bp}(x,y,z) = \left(1-\frac{z}{h}\right)\psi_{p+1}\left(\frac{\sqrt{(x-x_B)^2+(y-y_B)^2}}{l_{AB}}\right), \tag{B3}$$

$$\text{for node } M, pp: \quad N_{AB,pp}(x,y,z) = \psi_{k+1}\left(1-\frac{z}{h}\right)\psi_{l+1}\left(\frac{\sqrt{(x-x_B)^2+(y-y_B)^2}}{l_{AB}}\right), \tag{B4}$$

$$\text{for node } M, tp: \quad N_{AB,tp}(x,y,z) = \frac{z}{h}\psi_{p+1}\left(\frac{\sqrt{(x-x_B)^2+(y-y_B)^2}}{l_{AB}}\right), \tag{B5}$$

for every combination of $k = l = 2, \ldots, p$. These functions are used to derive the corresponding shape function boundary conditions by applying the displacement in x, y, and z directions, as described previously, for example, in (A4) only on the face Γ_{AB}. For the remaining faces of Γ_i^D the Dirichlet boundary condition is equal to zero.

3.3 Article 3: Positron annihilation lifetime spectroscopy of ABS objects manufactured by fused deposition modelling

M. Dryzek and E. Dryzek. Positron annihilation lifetime spectroscopy of ABS objects manufactured by fused deposition modelling. *Acta Physica Polonica A*, 132(5):1506-1508, 2017. 40 points, IF = 0.577, https://doi.org/10.12693/APhysPolA.132.1506.

3.3.1 Short description of the positron annihilation lifetime spectroscopy and its applications

Positron annihilation has been widely used for the study of materials at the atomic level. A positron emitted from a radioactive source into matter loses its energy in a short time (less than 2 ps) in the thermalization process. Having thermal energy, he wanders randomly and annihilates with an encountered electron after a time longer than 100 ps. As a result of the annihilation of the electron-positron pair, their mass is converted into energy in the form of mainly two gamma rays. If there are defects in the crystalline structure of the material studied, such as vacancies, their clusters, or dislocations, positron can be trapped there. Due to a lower local electron density the probability of annihilation decreases and the positron lifetime increases. The lifetime of positrons is an indicator of defects in the crystal lattice allowing them to be identified as well as their concentration.

In the positron lifetime spectrometer there are two detectors with BaF2 crystals. One of them registers the gamma photon of energy of 1275 keV emitted from the ^{22}Na nucleus after an emission of the positron that starts the timer. The second detector registers one of the annihilation photons of energy 511 keV, that allows to determine the spectrum of the positron lifetime in the tested material.

It is worth mentioning that defects determine many properties of the materials. These are e.g. yield strength, tensile strength, ductility, creep, and fatigue, as well as thermal and electrical conductivity of metals and semiconductors. Only a few material properties do not depend on defects, or only depend on them to a small extent, e.g., melting point or modulus of elasticity. The study of defects is one of the main objectives of materials science and engineering, and positron annihilation spectroscopy is a useful tool to study these defects.

PALS is used mostly to study lattice defects in metals or semiconductors. However, in molecular materials, a bound state of electron and positron, analogous to the hydrogen atom, called positronium (Ps) can be formed. It is formed in regions with low electron density, e.g., local free volumes in polymers. Positronium can form in two spin states arising from the relative orientations of the spins of the electron and the positron: para-positronium (p-PS) with antiparallel spins and ortho-positronium (o-Ps) with parallel spins. The para-positronium annihilates into two gamma photons, while the ortho-positronium annihilates into three gamma photons. The lifetime of the para-positronium in vacuum is 125 ps, while the ortho-positronium lives in vacuum three orders of magnitude longer, i.e., 146 ns. The lifetime of o-Ps in matter is shortened to a few nanoseconds because the positron can annihilate with another electron with anti-parallel spin from the free volume walls rather than with the one it is bound to. This process called pick-off is the basis for using o-Ps as a probe of local free volumes. The free volume model used in PALS relates the lifetime of o-Ps with the size of the inter- and intra-molecular regions in molecular materials and allows to determine their size.

PALS can be used to study changes in molecular microstructure of polymers impacting the local free volumes which take place under influence a variety of factors such as temperature, pressure, chemical changes. Free volume plays an important role in processes such as glass transition, polymer blend mixing, plasticisation, stress relaxation, aging, stress flow, permeability, and diffusion. All this was a premise to attempt to use PALS in studies of the effect of fused deposition modeling parameters on the free volume microstructure of ABS (acrylonitrile butadiene styrene) objects produced using this method.

Vol. **132** (2017) *ACTA PHYSICA POLONICA A* No. 5

Proc. of 12th International Workshop on Positron and Positronium Chemistry, August 28–September 1, 2017, Lublin, Poland

Positron Annihilation Lifetime Spectroscopy of ABS Objects Manufactured by Fused Deposition Modelling

M. Dryzek[a] and E. Dryzek[b,*]

[a]Institute for Computational Civil Engineering, Cracow University of Technology, Kraków, Poland
[b]Institute of Nuclear Physics, Polish Academy of Sciences, PL-31342 Kraków, Poland

Positron annihilation lifetime spectroscopy was used to study acrylonitrile butadiene styrene (ABS) specimens manufactured using fused deposition modelling to explore possibilities of identifying differences in molecular structure. The set of specimens was prepared including square tiles and long rectangular tiles (100 mm and 200 mm long) with all filament roads parallel to the longer edge. All types of tiles were produced with various infill line distance parameter resulting in different overlapping of the roads in horizontal and vertical directions. The slight increase of the *ortho*-positronium lifetime indicating increase of the mean free volume radius was observed for the longest tiles for which influence of weld interface is expected to be most pronounced. No differences were observed for different infill line distance parameters.

DOI: 10.12693/APhysPolA.132.1506
PACS/topics: 78.70.Bj, 61.41.+e

1. Introduction

Additive manufacturing (AM) commonly referred to as 3D printing is a manufacturing process of producing parts by adding-layer-upon-layer of material. Traditionally, it has been used for singular rapid prototyping purposes including visualisation, design verification, and functionality testing. However, objects manufactured by AM are more frequently considered as potential end-use products. In recent years 3D printing has become more and more popular mostly because of the equipment price drop [1].

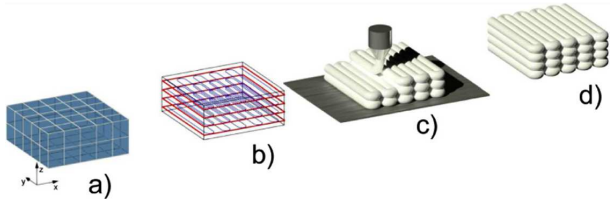

Fig. 1. Schematics of fused deposition modelling process: (a) CAD model, (b) slicing, (c) 3D printing, (d) post-processing.

Fused deposition modelling (FDM) is one of the most popular AM technologies. The process can be divided into four steps (see Fig. 1). First the 3D CAD model of a desired element is being prepared using a computer software. Then the software slices the model into layers, calculates the path of extruded material, called toolpath or raster, and adds model of support material if necessary. The path pattern usually is prepared in the way that material creates the solid outer surface called contour and lattice inner fill called infill. In the next step, the software convert the path to a code and sends commands to an automated machine called a 3D printer and the process of production begins. The main part of the 3D printer is the extruder. It can be precisely manoeuvred in $X-Y-Z$ print area by stepper motors and it can heat, melt, and deposit a thermoplastic filament through its nozzle in the wanted location. The extruder follows the toolpath prepared by the software and deposits roads of material. Due to the thermal fusion the road bonds with the layer beneath and roads beside and solidifies creating a solid fill, which then forms the chosen shape. Finally, the created part is being post-processed by removing any additional supports and smoothening the surface. The technology is simple to use. The products can have complex geometries and its contour and infill path can be varied depending on expected properties. However, the material is heterogeneous, filled with layers of fine roads, welds between and voids which creates anisotropy of the material properties. Also the outer surface is not smooth because of layered structure (stair-stepping).

Due to rapid invention in the field of 3D printing the technology found application in variety of disciplines from medicine [2], car industry [3], to even building industry [4]. Ease of using the tools, no need of producing expensive moulds and control over inner structure of the final product give AM advantage over conventional manufacturing methods especially in projects which require only one or a few copies of the same part. In many of these cases the produced parts are expected to have certain structural, mechanical or thermal properties. This creates a new subject for exploring by science testing and analysis.

Typical material used in small scale FDM process are thermoplastic polymers in a form of filament including

*corresponding author; e-mail: ewa.dryzek@ifj.edu.pl

polycarbonate and ABS. ABS is common thermoplastic characterised by its toughness and strength. Its properties are determined by composition of three monomers: acrylonitrile, butadiene, and styrene. Acrylonitrile and styrene polymers are responsible for strength and rigidity while butadiene rubbery phase for toughness. The average size of the butadiene particles is 200 nm, however, the size distribution is so large that particles 50 μm in diameter can be also found [5].

During manufacturing process the material must be heated to its melting point to form it through the nozzle and create sufficient bond with previously extruded layer. ABS is amorphous and therefore has no true melting point. The temperature in FDM process is kept above its glass transition temperature, which is *ca.* 105 °C. Usually higher temperature ($\approx$ 230 °C) is required to additionally heat already built material to create a form of weld with newly extruded bead. Exceeding this temperature may, however, spoil the material by breaking polymer chains [1].

It was reported that the weld interface tends to have other molecular structure then the road build and it varies between raster configuration in the same specimen shape [6]. The authors suggest that differences may result from variation of time of bonding of the neighbouring roads and because ABS is sensitive to thermal history. This observation casts a new light on a complex issue of mechanical properties of 3D printed objects. In the present investigation, we attempt to find out if the positron annihilation lifetime spectroscopy (PALS) can detect changes in the free volume microstructure connected to the presence of the weld interface in the 3D printed samples.

2. Experimental

Specimens were produced in FDM 3D printer 3D Kreator Motion. Material used in the process was ABS-FX in filament form manufactured by F3D Filament. The filament was heated to 230 °C. The speed of depositing was set to 60 mm/s. The nozzle diameter was equal to 0.4 mm. The specimens were chosen to be in the form of 5 mm thick tiles 10 mm in width. There were three length variants: 10 mm, 100 mm, 200 mm. The slicing software to create input file for the printer was Cura 2.5. The raster pattern was chosen to be lines without change in angle between the layers which resulted in unidirectional roads packing (see Fig. 2). Thus, raster orientation defined as the angle between the print direction and the long axis of the specimens was equal to 0°. The layer height was equal to 0.35 mm. Different infill line distance (see Fig. 3), i.e., 0.34, 0.37, and 0.4 mm was chosen to differentiate the weld interface range in the build. Infill line distance minus diameter is sometimes referred to as raster to raster air gap. If this value is negative roads are overlapping and this print configuration is reported to improve mechanical properties of an component as a whole [7].

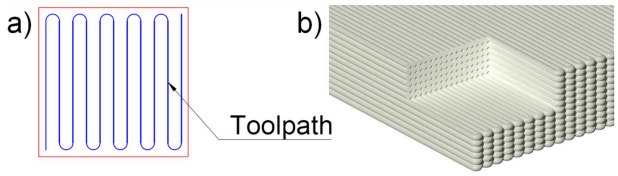

Fig. 2. (a) A toolpath example in one layer. (b) Visualisation with the cross-section trough.

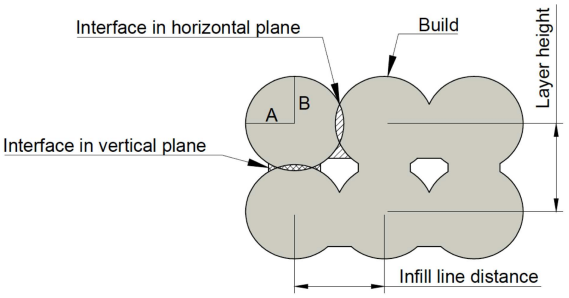

Fig. 3. A simplified cross-section of the unidirectional print proposed in [8].

For PALS measurements, a lifetime spectrometer with a time resolution (FWHM) of 280 ps was used. A positron source of ^{22}Na deposited on Kapton foil (7 mm thick) was sandwiched between two identical samples. The obtained PALS spectra with a total number of 1.5×10^6 counts were analysed using the LT code [9], taking into account three annihilation channels: i.e. *p*-Ps, free positrons, and *o*-Ps annihilation; as well as background subtraction and the source contribution allowed us to obtain χ^2 of the fit close to unity.

3. Results and discussion

The way the specimens were prepared, i.e., with the toolpath pattern being lines along the tile length without changing the build orientation between the layers was chosen to enhance the influence of the interface between builds. The weld interface between the roads was found to be depleted in the rubbery butadiene phase in comparison to the build surfaces [6]. It also exhibited an interfacial stiffening effect connected to increase in the indentation elastic modulus. This effect was more pronounced when the rasters were relatively long and it was explained by the shorter time in which the beads interacted with each other being still in the melt state during deposition [6]. Thus the samples prepared by 3D printing are not entirely homogeneous and this can affect positron annihilation including the size of local free volumes detected by *o*-Ps.

Considering three components, the analysis of the positron lifetime spectra gave the following values: τ_1 close to 0.19 ns with intensity I_1 equal to *ca.* 17%, τ_2 close to 0.45 ns with intensity I_2 equal to *ca.* 60% which

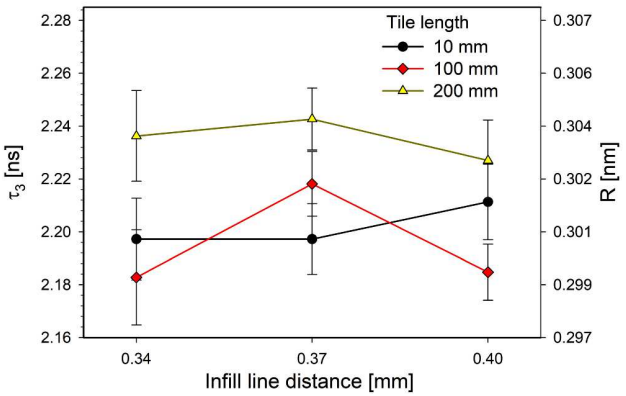

Fig. 4. The *o*-Ps lifetime as a function of the infill distance for specimens of different length.

are similar for all the samples. The values of the longest lifetime component, τ_3, as a function of the infill line distance for the 3D printed samples of different length are shown in Fig. 4. Assuming that *o*-Ps annihilates in the pick-off process, the right axis shows the average local free volume radius calculated according to the semi-empirical model [10, 11] from the formula

$$\tau_3 = \frac{1}{2}\left(1 - \frac{R}{R+\Delta R} + \frac{1}{2\pi}\sin\frac{2\pi R}{R+\Delta R}\right)^{-1}, \qquad (1)$$

where R is a radius of the hole and ΔR is an electron layer thickness. The value of ΔR was estimated as 0.166 nm. Because for polymers τ_3 is the most relevant quantity we will focus on its behaviour. For all the samples *o*-Ps intensity I_3 does not change significantly and is equal to *ca.* 23%.

It can be seen from Fig. 4 that for the shorter tiles, i.e., 10 mm and 100 mm long, τ_3 has the same value within the experimental error range and it is equal to *ca.* 2.20 ns which corresponds to the average free volume radius equal to 0.30 nm. It should be mentioned that the values reported in the literature for ABS are slightly lower, *ca.* 2.14 ns [12, 13]. It is worth noticing that for the 200 mm long tiles even higher values of τ_3, *ca.* 2.24 ns corresponding to the average free volume radius 0.31 nm are obtained. It can be expected that the differences in positron lifetime values caused by higher length of raster would be small. The change of the volume fraction of the weld interface caused by adjustments of infill line distance parameter in the samples is limited, thus its contribution to the positron lifetime spectrum is small. Additionally, in polymers the free volume holes are not uniform in size and the obtained values of τ_3 and subsequently values of the free volume radii are averaged over some distribution. It seems that the effect however small is observed for the samples with the longest raster. The effect of different infill distance for the measured samples is negligible.

The farther investigations require enhancement of the interface weld volume fraction by for example using smaller nozzle or/and increasing the sample length. Together with results from different mechanical test the PALS method may enrich knowledge about influence of microstructure on strength and durability of additive manufacturing elements.

4. Conclusions

In the paper, there were presented the results of the positron lifetime measurements of ABS specimens manufactured by FDM process. The specimens of unidirectional print configuration with different raster length and different overlapping of filament roads were chosen to highlight the presence of weld interface in the build. Results shows that the length of raster has some small influence on *o*-Ps lifetime value causing its increase from 2.20 ns to 2.24 ns for specimens with the longer raster. The differences are not observed when it comes to variations in the infill line distance parameter in the samples.

Acknowledgments

The authors wish to thank Ms. Aleksandra Gawron at 3D FLY S.C. for preparing the samples.

References

[1] B.N. Turner, R. Strong, S.A. Gold, *Rapid Prototyping J.* **20**, 192 (2015).

[2] U.K. Roopavath, D.M. Kalaskar, in: *3D Printing in Medicine*, Ed. D.M. Kalaskar, Woodhead Publ., 2017, p. 1.

[3] S. Curran, P. Chambon, R. Lind, L. Love, *SAE Technical Paper*, 2016-01-0328 (2016).

[4] F.P. Bos, R.J.M. Wolfs, Z.Y. Ahmed, T.A.M. Salet, *Virt. Phys. Prototyp.* **11**, 209 (2016).

[5] R. Marissen, D. Schudy, A.V.J.M. Kemp, S.M.H. Coolen, W.G. Duijzings, A. Van Der Pol, A.J. Van Gulick, *J. Mater. Sci.* **36**, 4167 (2001).

[6] D.P. Cole, J.C. Riddick, H.M. Iftekhar Jaim, K.E. Strawhecker, N.E. Zander, *Appl. Polym. Sci.* **133**, 30 (2016).

[7] M.S. Hossain, J. Ramos, D. Espalin, M. Perez, R. Wicker, in: *24th Int. SFF Symp. An Additive Manufacturing Conf. SFF 2013*, University of Texas at Austin, 2013, p. 380.

[8] L. Li, Q. Sun, C. Bellehumeur, P. Gu, *J. Manuf. Process.* **4**, 129 (2002).

[9] J. Kansy, *Nucl. Instrum. Methods A* **374**, 235 (1996).

[10] S.T. Tao, *J. Chem. Phys.* **56**, 5499 (1972).

[11] N. Eldrup, D. Lightbody, J.N. Sherwood, *Chem. Phys.* **63**, 51 (1981).

[12] G. Dlubek, M.A. Alam, M. Stolp, H.-J. Radusch, *J. Polym. Sci. B Polym. Phys.* **37**, 1749 (1999).

[13] B.E. Tiganis, L.S. Burn, P. Davis, A.J. Hill, *Polym. Degrad. Stabil.* **76**, 425 (2002).

3.4 Article 4: Experimental and multiscale computational static and dynamic study of 3D printed elements with mesostructure

M. Dryzek, W. Cecot, and M. Tekieli. Experimental and multiscale computational static and dynamic study of 3D printed elements with mesostructure. *Finite Elements in Analysis and Design*, 215:103876, 2023. 100 points, IF = 2.618, `https://doi.org/10.1016/j.finel.2022.103876`.

Finite Elements in Analysis and Design 215 (2023) 103876

Contents lists available at ScienceDirect

Finite Elements in Analysis & Design

journal homepage: www.elsevier.com/locate/finel

Experimental and multiscale computational static and dynamic study of 3D printed elements with mesostructure

Mateusz Dryzek *, Witold Cecot, Marcin Tekieli

Chair for Computational Engineering, Faculty of Civil Engineering, Cracow University of Technology, ul. Warszawska 24, Krakow, Poland

ARTICLE INFO

Keywords:
Multiscale finite element method
Higher-order shape functions
Extrusion 3D printing
Orthotropy
Free vibrations

ABSTRACT

Numerical and experimental studies were conducted to demonstrate the applicability of the multiscale finite element method (MsFEM) with the higher-order approximation to the prediction of mechanical behavior of 3D printed parts with complex mesostructure. Three scales are considered: the microscale, at which the filament paths are homogenized using an orthotropic material model with experimentally identified properties; the mesoscale with 3D printed structure that is upscaled by MsFEM; and the macroscale, at which the overall problem is effectively solved. To validate the approach that may be useful for designing 3D printed elements, the authors conducted experimental measurements of static bending and free vibrations of beams with four different mesostructures and two print orientations. The measurements were performed using digital image correlation and were compared with numerical modeling performed by the authors. Both results coincide very well for a number of examples. Moreover, the study revealed that the hierarchical higher-order shape functions can accurately represent free vibrations even for the high frequencies.

1. Introduction

In recent years, significant progress has been observed in the field of materials manufacturing. A substantial contribution to the progress can be assigned to additive manufacturing (AM), popularly known as 3D printing. The technology enables a combination of two or more constituent materials, as well as rearrangement of matter in the volume through the introduction of certain mesostructures that would hardly be possible to obtain using traditional manufacturing techniques (see Fig. 1). During the design process of 3D printed materials, digital simulation is often incorporated to reduce the cost of experimental testing. This is a challenging task for the direct numerical methods like the finite element method (FEM) because of the complexity of the multiscale nature of these materials. Therefore, the authors of this paper use and develop the multiscale finite element method (MsFEM), originally proposed by Hou and Wu [1], in order to enable effective analysis of 3D printed material fabricated using the material extrusion technique.

AM is a manufacturing process of producing parts by adding layer upon layer of material. Traditionally, it has been used for rapid prototyping purposes, including visualization, design verification, and functionality testing. However, objects manufactured by AM are more frequently considered as potential end-use products. Thus, these objects are expected to have certain structural, mechanical, or thermal properties. The technology found applications in a variety of disciplines, ranging from medicine [2] to automotive [3], and building industries [4]. AM has many advantages over conventional manufacturing methods, particularly when facing a project that requires only one or a few copies of the same part. In such a case, AM is easy to use, does not require the production of expensive molds, and provides control over the inner structure of the final product.

Material extrusion is one of the most popular forms of AM technology. The parts in this process are formed by laying down filament which bonds to the layer beneath through thermal or chemical fusion. This makes the material heterogeneous, filled with layers of often visible fine paths, welds and voids between them, yielding anisotropic material properties. Efficient computer modeling of elements manufactured with the material extrusion technique may be done by different multiscale methods, e.g. the asymptotic approach, presented by Rodríguez et al. [5] or numerical homogenization by representative volume element (RVE), described by Makowski and Kuś [6]. Similarly, the theory of laminate was utilized by Li et al. [7] in this problem, and it was also compared to solid orthotropic material simulation by Martínez et al. [8]. A more recent study by Liu and Shapiro [9] developed a new method that homogenized detailed microstructure through a solution of an integral equation formulated using Green's function. An investigation of the failure mechanisms was proposed using brute force modeling [10–12], where all the filament paths and voids were modeled using FEM.

* Corresponding author.
E-mail address: mateusz.dryzek@pk.edu.pl (M. Dryzek).

https://doi.org/10.1016/j.finel.2022.103876
Received 16 August 2022; Received in revised form 29 October 2022; Accepted 7 November 2022
Available online 6 December 2022
0168-874X/

Fig. 1. Example of sophisticated mesostructure achieved through additive manufacturing: a concrete 3D printed bridge in Madrid, Spain.

This article presents, after Cecot and Oleksy [13], the application of MsFEM with higher-order functions to modeling elements manufactured with the use of 3D printing extrusion-based technology. MsFEM is an upscaling method that captures the microscale heterogeneity by special basis functions and greatly reduces the number of degrees of freedom (DOFs) in contrary to direct solution. Neither the scale separation nor the periodicity of the mesostructure has to be assumed. Furthermore, the calculations of the basis functions can easily be parallelized. As 3D printed materials are characterized by two or more scales and often a large porosity (void to volume fraction), the MsFEM adaptation towards analyzing these problems could prove to be highly beneficial.

For modeling 3D printed material, a three-scale approach is proposed (see Fig. 2). In the microscale, the material built of filament paths is homogenized by assuming orthotropic constitutive equations with experimentally determined parameters. The mesoscale structure is depicted by the MsFEM shape functions. Finally, the problem is solved on the macroscale. For the validation purpose, experimental measurements of bending and free vibrations of beam-like elements were conducted, with four different mesostructures and two print orientations. The authors also originally applied and tested the higher-order MsFEM [13,14] for analysis of free vibrations. It is worth mentioning that MsFEM has already been used for a three-scale analysis in [15] but at the microscale level.

In this three-scale computation, two upscaling errors are made. The first one appears when the constitutive parameters and equations are assumed for the mesostructure, neglecting the microscale voids. The second upscaling error is added by MsFEM, which uses macroelements incorporating the mesoscale properties in an approximate way. Therefore, comparisons with experiments were proposed in order to validate such multiscale modeling. The accuracy of the direct numerical modeling, by the adaptive isogeometric analysis, was confirmed by experimental measurements conducted for 3D printed samples by Alaimo et al. [16]. Also, in another work by Carraturo et al. [17], 3D printed beams, were used to determine the modeling error introduced by the well-known asymptotic homogenization. The authors concluded that the additional modeling error is acceptable in this case, especially remembering that a significant reduction of computation time is observed due to homogenization.

In this study, an upscaling by the MsFEM method was used, that requires neither material periodicity nor scale separation. The higher order (up to $p = 5$) macro-scale approximation and the first order of approximation at the mesoscale were proposed. It was also experimentally confirmed that the MsFEM upscaling with such an approximation contributes slightly to the modeling error for both statics and dynamics with heterogeneous material. Moreover, it enables much faster numerical analysis than the direct numerical analysis.

The paper is divided into 6 sections. In Section 2, the orthotropic mechanical model of 3D printed material is discussed and the parameters for the given base material and print configuration are identified through tensile tests. Next, in Section 3, experiments on selected beams with various mesostructures are reviewed. In Section 4, a numerical model is discussed and MsFEM with linear and higher-order multiscale basis functions is briefly introduced. In Section 5, the experimental and numerical results are compared and the convergence of the method is studied. In Section 6, conclusions are presented.

2. 3D printed material

2.1. Elastic deformations

After Li et al. [7] and Alaimo et al. [18], extrusion-based 3D printed material is considered in this study as a composite made of orthotropic layers of filament rasters. Fig. 3 presents a cross-section through a sample, as well as the common terminology associated with filament-based processes.

The constitutive relations for a general linear elastic material can be written as:

$$\boldsymbol{\sigma} = \boldsymbol{C}\boldsymbol{\epsilon}, \tag{2.1}$$

where $\boldsymbol{\sigma}$ and $\boldsymbol{\epsilon}$ denote stress and strain tensors respectively, and $\boldsymbol{C}$ is the tensor of material parameters.

This study focuses on the effect of layer orientation on the mechanical behavior of printed parts in the plane stress state. It is assumed that the coordinate system $\{1, 2\}$ is right-handed, direction 1 is aligned to the lamina plane and direction 2 is perpendicular to it and represents the layer stacking direction (see Fig. 4).

Assuming the plane stress state, problem (2.1) can be expressed using the Voigt notation as follows:

$$\begin{bmatrix} \sigma_{11} \\ \sigma_{22} \\ \tau_{12} \end{bmatrix} = \begin{bmatrix} C_{11} & C_{12} & 0 \\ C_{12} & C_{22} & 0 \\ 0 & 0 & 2C_{33} \end{bmatrix} \begin{bmatrix} \epsilon_{11} \\ \epsilon_{22} \\ \epsilon_{12} \end{bmatrix}, \tag{2.2}$$

and ϵ_{33} can be computed by condition $\sigma_{33} = 0$. It is well known that the coefficients of the $\boldsymbol{C}$ tensor can be expressed as a function of the longitudinal Young's modulus E_1, transverse Young's modulus E_2, Poisson's ratio ν_{12}, and the shear modulus G_{12}:

$$C_{11} = \frac{E_1^2}{E_1 - \nu_{12}^2 E_2}, \quad C_{22} = \frac{E_1 E_2}{E_1 - \nu_{12}^2 E_2}, \quad C_{12} = \frac{\nu_{12} E_1 E_2}{E_1 - \nu_{12}^2 E_2}, \tag{2.3}$$
$$C_{33} = G_{12}.$$

The material parameters E_1, E_2, and ν_{12} can easily be identified using the standard tensile tests. However, identification of the shear modulus may be more troublesome. Thus, an additional tensile test was utilized for specimens with layers rotated by angle θ to the elongation direction, as proposed by Li et al. [7]. Hooke's law in this new coordinate system can be expressed as:

$$\hat{\boldsymbol{\sigma}} = \hat{\boldsymbol{C}}\hat{\boldsymbol{\epsilon}}. \tag{2.4}$$

Transformed stiffness matrix $\hat{\boldsymbol{C}}$ can be derived in the following way by tensor rotation in Voigt notation (refer to e.g. Gerdeen and Rorrer [19], Eq. 8.64–8.65):

$$\hat{\boldsymbol{C}} = \boldsymbol{T}^{-1}\boldsymbol{C}\boldsymbol{T}, \tag{2.5}$$

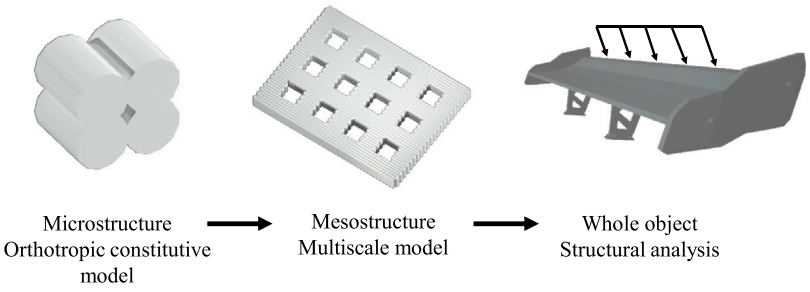

Fig. 2. Three-scale approach.

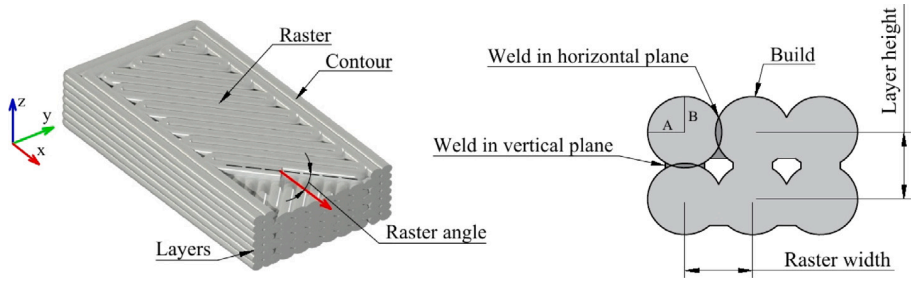

Fig. 3. Common terminology associated with extrusion-based 3D printing and a cross-section of a printed part.

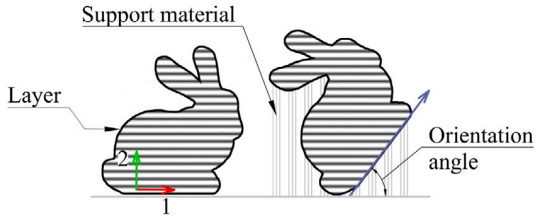

Fig. 4. Reference coordinate system $\{1,2\}$ aligned with layer plane and two parts printed in different orientations.

where $\boldsymbol{T}$ is the transformation matrix:

$$\boldsymbol{T} = \begin{bmatrix} \cos^2(\theta) & \sin^2(\theta) & 2\cos(\theta)\sin(\theta) \\ \sin^2(\theta) & \cos^2(\theta) & -2\cos(\theta)\sin(\theta) \\ -\cos(\theta)\sin(\theta) & \cos(\theta)\sin(\theta) & \cos^2(\theta) - \sin^2(\theta) \end{bmatrix}. \tag{2.6}$$

Relations (2.4) and (2.5) for uniaxial stress state imply the following formula for Young's modulus E_θ for the specimen having layers oriented at angle θ to the tested direction:

$$E_\theta = \left[\frac{\cos^4(\theta)}{E_1} + \frac{\sin^4(\theta)}{E_2} + \frac{\sin^2(2\theta)}{4} \left(\frac{1}{G} - \frac{2\nu_{12}}{E_1} \right) \right]^{-1}. \tag{2.7}$$

It is clear that $E_0 = E_1$ and $E_{90} = E_2$. Assuming that Young's modulus can be evaluated for another material orientation, e.g. $\theta = 45°$, Eq. (2.7) can be solved for G:

$$G = \left[\frac{4}{E_{45}} - \frac{1}{E_0} - \frac{1}{E_{90}} + \frac{2\nu_{12}}{E_0} \right]^{-1}. \tag{2.8}$$

2.2. Base material and printer

The 3D printer used in this study was the closed-chamber Stratasys Uprint. It is equipped with two extruders capable of printing model material and support material. The base material for the model was chosen to be Stratasys P4300XL ABS. The model material tip used was T16 (0.178 mm diameter). The print configuration was set to *Solid* with default settings: 0.254 mm layer height, 0.508 mm raster width, and one contour line. Raster angle was set to $\{45°, -45°\}$, meaning that angles between filament paths in two adjacent layers differ by 90°. This configuration ensures the same mechanical behavior of the part within the layer plane. The default temperature of the liquefier is 310 °C and the chamber interior one is 77 °C.

2.3. Material testing

Tensile tests were performed in order to determine elastic constants: E_0, E_{45}, E_{90}, and ν_{12}. As reported by Popescu et al. [20], there are no commonly agreed standards for material extrusion specimens testing. The initial tests with dumbbell-shaped specimens recommended in the ASTM D638 standard showed that such specimens fail consistently at the fillet due to the stress concentrations observed therein. Thus, after previous studies by Alaimo et al. [18], the ASTM D3039 standard that is designed to test polymer type anisotropic materials was considered. It recommends a specimen have a constant rectangular cross-section with additional tabs at a grip area that omit the troublesome fillets. Fig. 5 depicts the shape of the specimens, as well as the orientation at which they are printed.

Three types of specimens (T0, T45, and T90) were considered, and 10 samples were prepared for each type. The dimensions of the specimens are presented in Table 1. To prevent gripping damage and introduce load into the specimens more gradually during the test, tabs were glued to the specimen ends (two on each end) using a cyanoacrylate adhesive. The tabs were 3D printed with the same configuration as the specimens. In order to conduct the optical measurements, specimens were prepared with speckle patterns of black dots over a white background spray-painted on one side of the specimens.

The specimens were tested under displacement control on a universal testing machine Zwick Roell Zmart Pro with pincer grips type 8322. A head displacement rate of 2 $^{mm}/_{min}$ was set to achieve specimen failure within 1 to 10 min. Stress–strain response was recorded with longstroke extensometer of a 50 mm gauge length. Additionally, the strain field was measured using the Digital Image Correlation (DIC) technique to evaluate Poisson's ratio. During the tests, photos of the samples were taken at a 2 s interval and then processed in order to determine the material parameters. Photos were obtained using a digital single-lens camera with a matrix resolution of 6000 × 4000 pixels. The camera was equipped with a Sigma 17–50 mm f/2.8 AF

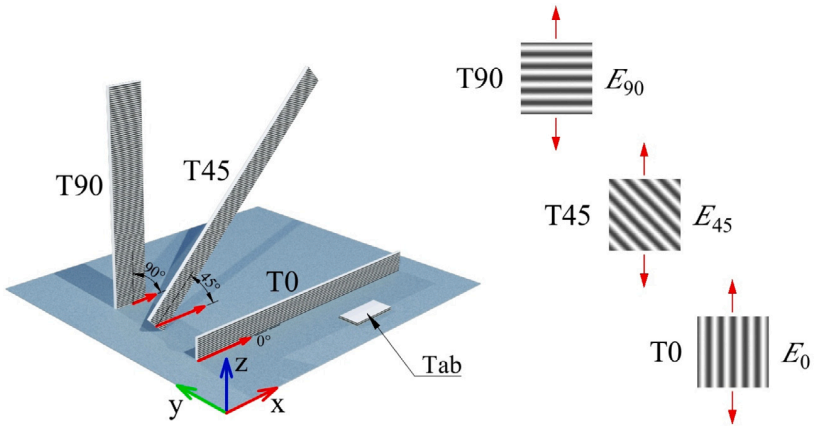

Fig. 5. Orientation of specimens for tensile tests. The layers were stacked in the Z direction.

Table 1
Specimen dimensions assumed after ASTM D3039.

Name	Layer orientation	Specimen length [mm]	Specimen & tabs width [mm]	Specimen thickness [mm]	Tabs length [mm]	Tabs thickness [mm]
T0	0°	200	15	2	36	1.6
T45	45°	200	15	3	25	1.6
T90	90°	150	25	3	36	1.6

Table 2
Test results for different print orientations.

Name	Layer orientation	Young's modulus [MPa]	Poisson's ratio	Ultimate strength [MPa]
T0	0°	2239 ± 13	0.41 ± 0.04	31.6 ± 0.3
T45	45°	1956 ± 10	–	25.2 ± 1.4
T90	90°	1920 ± 20	0.35 ± 0.05	19.7 ± 1.5

EX DC OS HSM zoom lens with a focal length set at about 24 mm to cover the entire surface of the samples. The surface of the specimen was additionally illuminated with a white LED light source with a neutral hue of about 6000 K. The collected images were iteratively processed using the CivEng Vision software developed at the Cracow University of Technology (for more details, refer to e.g. Tekieli et al. [21]; Słoński and Tekieli [22]). Two virtual strain gauges (virtual tensometers) were placed on the surface of the sample to measure the longitudinal and transverse deformation.

2.4. Material parameters

The tests for all three orientations revealed a pronounced linear elastic region (see Fig. 6(a)). Young's moduli were evaluated using linear regression within the strain range from 0.1% to 1%. The results are summarized in Table 2 and have error ranging from 0.5% to 1%. The table also contains Poisson's ratio evaluated for T0 and T90 specimens and average ultimate strengths for all the specimen types.

Poisson's ratio was calculated as a ratio between longitudinal and transverse strains measured optically beginning from the longitudinal strain of 0.1%. The final value of the ratio was calculated as the mean value of a series of measurements for the longitudinal strain range of 0.5% to 1% (see Fig. 6(b)) for a single sample and then averaged for five samples.

In the assumed orthotropic material model, ν_{21} is a dependent variable and can be calculated as a form of verification using the following relation:

$$\frac{\nu_{12}}{E_1} = \frac{\nu_{21}}{E_2}. \tag{2.9}$$

Solving for ν_{21} and using the measured values of the remaining constants yields $\nu_{21} = 0.35$, which with an accuracy of ± 0.05, is equal to the measured value.

The density of the material, computed as the arithmetic average of nine (3 for each specimen type) volume and mass measurements, equals 0.973 g/cm^3.

The results clearly display that the print orientation is an important parameter influencing the mechanical behavior of 3D printed parts. The relative difference in Young's modulus between longitudinal (T0) and transverse (T90) orientations is equal to about 15%. Fig. 6(c) depicts a curve that predicts Young's modulus in the uniaxial test for all layer orientations using Eq. (2.7). The elasticity tensor for the studied 3D printed material in the $\{1,2\}$ coordinate system reads:

$$\boldsymbol{C} = \begin{bmatrix} 2616 & 920 & 0 \\ 920 & 2243 & 0 \\ 0 & 0 & 1386 \end{bmatrix} \text{MPa} \tag{2.10}$$

Although it is outside of the scope of this paper, it has to be pointed out that layer orientation plays a significant role beyond the elastic region as well. It was observed that longitudinal specimens T0 exhibit more ductile behavior, with the prominent plastic region. Transverse specimens T90, on the other hand, show brittle behavior without any plastic deformation and with a failure mode of delamination that strongly influences the ultimate strength. The inclusion of these observations in the numerical model will be the subject of future work.

3. Experimental program

A series of static and free vibration tests with the cantilever beams of four types (B1–B4) was conducted to explore the mechanical behavior of 3D printed parts with mesostructure and validate the multiscale model. Beams of 11 cm span plus a 4 cm grip were designed as 2×11 grids of repeating cells. The dimensions of the beams and mesostructure cells are presented in Fig. 7. Each beam was printed with two layer orientations: 0° and 90°. In total, 8 beams were tested.

Static bending tests were performed with flexure test accessories: screw grips as fixed support and an upper anvil with a rocking mounting which applies the load to the specimen 10 cm from the support (see Fig. 8(a)). Constant rate of displacement of the anvil was set to

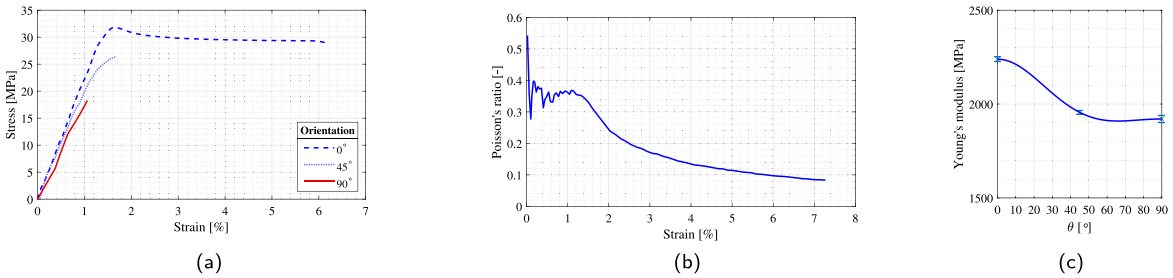

Fig. 6. Typical stress–strain curves for tested specimens after offset to compensate for alignment of the specimen (a). Typical Poisson's ratio-strain curve for T0 specimens (b). Young's modulus against layer orientation (c) (note that graph y-axis limits range from 1500 MPa to 2500 MPa).

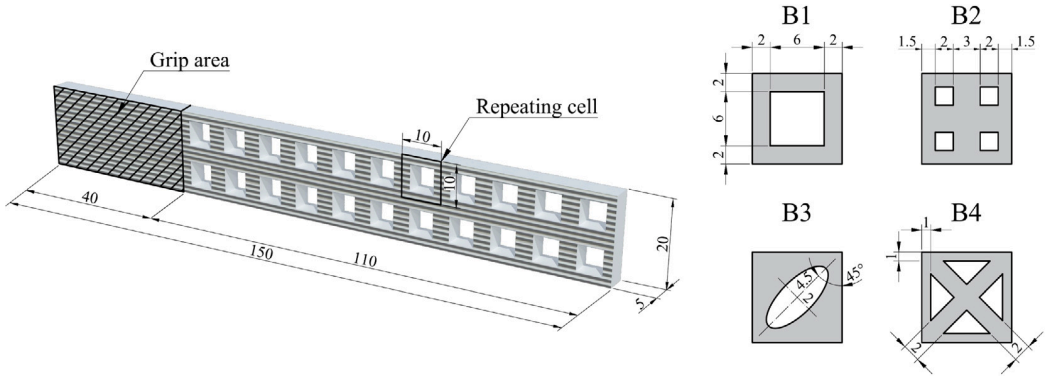

Fig. 7. Dimensions of tested beams and mesostructures [mm].

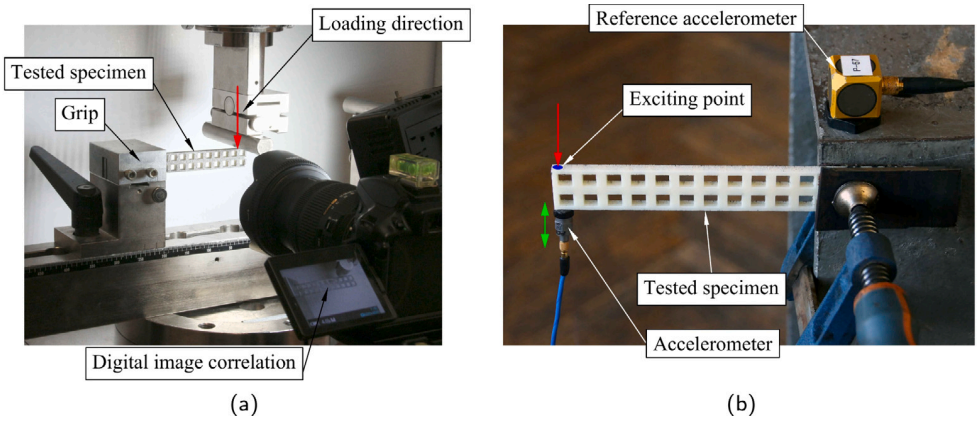

Fig. 8. Experimental setup of static and dynamic tests.

2 $^{mm}/_{min}$. Force versus displacement response was recorded with the machine measuring the force and travel of the anvil. The tests were accompanied by optical documentation with a camera for DIC analysis.

Vibration tests were performed by exciting beams into free vibrations. The beams were hit with an impulse hammer (PCB 086D05) with a force sensor at the tip. Acceleration was derived from the measurements made by a mono-axial accelerometer (PCB 352C66) attached to the end of the beam (see Fig. 8(b)). Measurements were recorded with a 4096 Hz frequency. Data was recorded through a portable data acquisition station LMS SCADAS MOBILE. 10 series of measurements were made per single specimen beam. The weight of the accelerometer with wire attached to the specimen was measured before and after the experiment. The average is equal to 6.1 g. A reference triaxial accelerometer was attached to the test stand in order to record stand vibrations, which turned out to be negligible.

3.1. Experimental results

The summary of the bending tests' results is shown in Fig. 9 on force versus displacement curves. Additional measurements obtained with DIC were used to validate numerical results and are presented in Section 5.1. The tests confirmed the finding from the previous section that 3D printed parts with ABS exhibit linear response at the first loading stage and that the print orientation influences the response. Beams printed in 90° orientation are less stiff in the tests. The beams of type B2 are the stiffest of the tested beams. Orientation also plays a role in the ultimate strength of the objects. Beams printed with 0° orientation withstand a force more than 2 times greater than beams printed in 90° orientation, which failed by delamination.

Fig. 10 presents a graph of a typical series of measurements in dynamic tests. The dominant frequency was determined by the fast

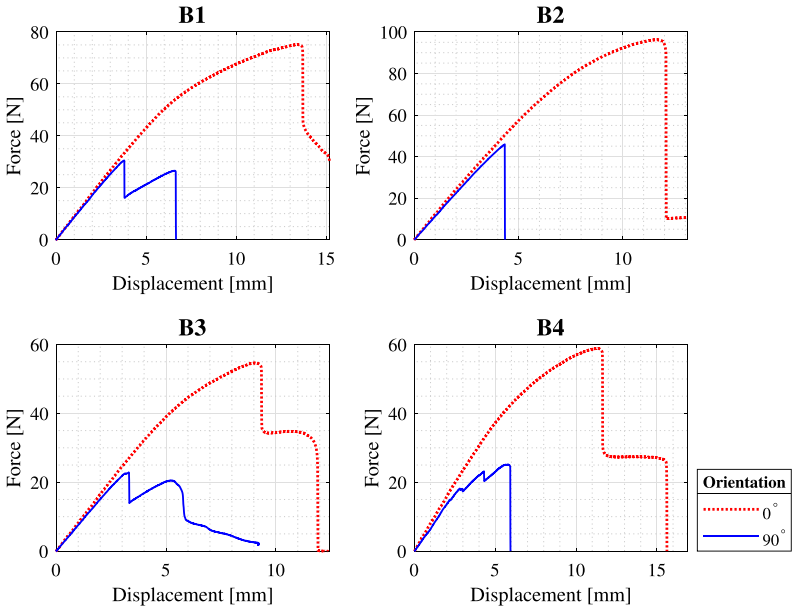

Fig. 9. Force–displacement curves of beams in bending tests.

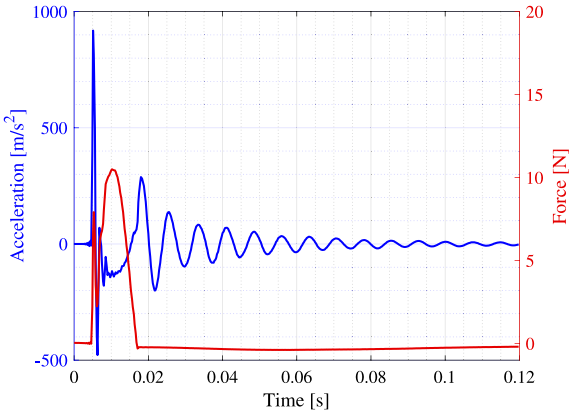

Fig. 10. Typical dynamic response graph.

Fourier transform and it is presented in Table 3 after averaging a few measurements. The effect of damping was taken into account in computing the natural frequencies by calculating decrements of acceleration; however, its impact was negligible (below 1%). The influence of the print orientation on the frequencies is measurable. Beams printed with a 90° orientation vibrated with lower frequencies than beams of the same geometry printed with a 0° orientation. The beams of type B2 vibrated with the highest frequencies, again indicating that their mesostructure is the stiffest one. Later, during numerical studies, it was revealed that the mass of the accelerometer and cable connecting the sensor added to the vibrating system was significant and lessened the effects of orthotropy on the results.

4. Numerical model

At the beginning, a 3D printed sample occupying domain Ω with boundary Γ is considered. The problem of linear elasticity reads:
Find displacement $\boldsymbol{u}$ *in domain* $\Omega \subset \mathbb{R}^n (n = 2 \text{ or } 3)$ *such that:*

$$\rho\ddot{\boldsymbol{u}} - \nabla \cdot \left(\boldsymbol{C}\nabla_s \boldsymbol{u}\right) = \boldsymbol{f}, \quad \text{in } \Omega, \tag{4.1}$$

$$\boldsymbol{u} = \hat{\boldsymbol{u}}, \quad \text{on } \Gamma^D, \tag{4.2}$$

Table 3
Natural frequencies measured in dynamic tests.

Beam type	Layer orientation	Frequency [Hz]
B1	0°	169.4 ± 2.2
B1	90°	163.2 ± 2.6
B2	0°	184.7 ± 7.6
B2	90°	187.1 ± 1.0
B3	0°	157.8 ± 1.7
B3	90°	152.5 ± 3.6
B4	0°	164.1 ± 2.0
B4	90°	153.8 ± 1.1

$$\boldsymbol{t} = \hat{\boldsymbol{t}}, \quad \text{on } \Gamma^N, \tag{4.3}$$

where Γ^D and Γ^N denote boundary parts with the Dirichlet and Neumann conditions, $\Gamma^D \cup \Gamma^N = \partial\Omega$, and $\Gamma^D \cap \Gamma^N = \varnothing$. $\hat{\boldsymbol{u}}$ and $\hat{\boldsymbol{t}}$ denote known displacement and loading, $\boldsymbol{t} = \left(\boldsymbol{C}\nabla_s \boldsymbol{u}\right) \cdot \boldsymbol{n}$, ∇_s is the symmetric part of the gradient operator, i.e. $\nabla_s(\bullet) = ((\bullet) \otimes \nabla + \nabla \otimes (\bullet))/2$, and ρ stands for the material density.

The corresponding weak form of (4.1)–(4.3) reads:
Find displacement $\boldsymbol{u} \in \boldsymbol{H}_1^0(\Omega) + \hat{\boldsymbol{u}}$ *such that:*

$$\int_\Omega \boldsymbol{v} \cdot \rho\ddot{\boldsymbol{u}} \mathrm{d}\Omega + \int_\Omega \nabla\boldsymbol{v} \cdot \left(\boldsymbol{C}\nabla_s \boldsymbol{u}\right) \mathrm{d}\Omega = \int_\Omega \boldsymbol{v} \cdot \boldsymbol{f} \mathrm{d}\Omega + \int_{\Gamma^N} \boldsymbol{v} \cdot \hat{\boldsymbol{t}} \mathrm{d}\Gamma, \forall \boldsymbol{v} \in \boldsymbol{H}_1^0(\Omega), \forall t \in \left[0, t_f\right], \tag{4.4}$$

where $\boldsymbol{H}_1^0(\Omega) = \{\boldsymbol{v} \in \boldsymbol{H}_1(\Omega) : \boldsymbol{v} = 0|_{\Gamma^D}\}$, $\boldsymbol{H}_1(\Omega)$ is the Sobolev space of square-integrable functions.

In the scope of this paper, the authors intend to focus on two time-independent cases that – after discretization with a fine mesh of size h, capturing mesoscale details of a 3D printed part – read:

$$\text{statics: } \boldsymbol{K}^h \boldsymbol{u}^h = \boldsymbol{f}^h, \tag{4.5}$$

$$\text{free vibrations: } \boldsymbol{K}^h \boldsymbol{u}_j^h = \omega_j^2 \boldsymbol{M}^h \boldsymbol{u}_j^h, \tag{4.6}$$

where $\boldsymbol{K}^h$ and $\boldsymbol{M}^h$ denote the stiffness and mass matrices, $\boldsymbol{f}^h$ denotes the load vector, and $\boldsymbol{u}_j^h$ and ω_j represent the jth vibration mode and the corresponding angular frequency.

4.1. MsFEM idea

In MsFEM two meshes are utilized. A coarse grid of macroelements K_i $(i = 1, 2 \dots N_{el})$ of size H is generated to capture the mesoscale details. Each macroelement is then refined with a mesh of a much shorter characteristic size h.

The MsFEM algorithm consists of three steps: computation of the multiscale basis functions by solving auxiliary local boundary value problems in each macroelement using fine meshes, which enables evaluation of the equivalent coarse element stiffness matrices; the macro-scale computation, in which the finite element analysis of the coarse meshes is carried out using the macroelement equivalent stiffness matrices; and finally, the downscaling operation performed in order to reproduce the solution on the fine mesh in each macroelement separately.

In this analysis, two types of multiscale functions are introduced: the skeleton and the bubble basis functions. The first will be responsible for capturing global solutions, while the second will represent local solutions inside macroelements.

4.1.1. Skeleton multiscale basis functions

The classic multiscale basis functions are defined by the following boundary value problem:

$$-\nabla \cdot \left(\boldsymbol{C} \nabla_s \boldsymbol{\phi}_k^s\right) = \boldsymbol{0}, \text{ in } K_i, \tag{4.7}$$

$$\boldsymbol{\phi}_k^s = \boldsymbol{\psi}_k, \text{ on } \Gamma_i, \tag{4.8}$$

where $\boldsymbol{\psi}_k$ denotes a shape function associated with the kth degree of freedom of the coarse mesh. Only traces of $\boldsymbol{\psi}_k$ functions on Γ_i are needed to construct multiscale shape functions as depicted in the example in Fig. 11.

In this work, a hierarchical base will be adopted as a source term. The concept is inspired by the higher-order FEM approach introduced by Babuška et al. [23] and Zienkiewicz et al. [24]. The very idea of the hierarchical base is to increase the order of approximation by adding new shape functions that do not alter the lower-order shape functions. This property is beneficial in MsFEM, since no costly recalculations of the existing shape functions are needed in case of approximation enrichment.

The problem (4.7)–(4.8) can be solved directly on a macroelement fine mesh using FEM or by eliminating interior DOFs using static condensation (see Cecot and Oleksy [25]). It is intuitive that if as many linear independent multiscale shape functions are used to construct the solution as there are fine-mesh DOFs on the edges of the macroelement, the global fine-mesh solution achieved by the static condensation will be reproduced. However, for the dynamic problems, the static condensation may lose details inside macroelements, thus the bubble multiscale basis functions are reintroduced after Soghrati and Stanciulescu [26], as well as Cecot and Oleksy [13].

4.1.2. Bubble multiscale basis functions

In order to represent a local solution inside K_i, the authors adopt a strategy of constructing multiscale basis functions using polynomials of appropriate order to define the right-hand sides:

$$-\nabla \cdot \left(\boldsymbol{C} \nabla_s \boldsymbol{\phi}_k^b\right) = \nabla \cdot (\nabla \boldsymbol{\psi}_k), \text{ in } K_i, \tag{4.9}$$

$$\boldsymbol{\phi}_k^b = \boldsymbol{0}, \text{ on } \Gamma_i, \tag{4.10}$$

where $\boldsymbol{\psi}_k$ are hierarchical bubble functions mapped on K_i that are equal to zero on Γ_i. Fig. 12 depicts a hierarchical bubble function for $p = 2$, a source function, and resulting multiscale shape functions.

It should be noted that $\boldsymbol{\phi}^s$ and $\boldsymbol{\phi}^b$ are $\boldsymbol{C}(\boldsymbol{x})$-orthogonal, i.e. $\int_{K_i} \nabla \boldsymbol{\phi}^s \cdot \left(\boldsymbol{C} \nabla_s \boldsymbol{\phi}^b\right) \mathrm{d}\Omega = \boldsymbol{0}$.

4.1.3. MsFEM workflow

Problems (4.7)–(4.8) and (4.9)–(4.10) are solved numerically on the fine mesh. The obtained DOFs of the fine mesh of a single macroelement comprise a column of prolongation matrix $P_{N \times M}$, where M denotes the number of shape functions in macroelement K_i and N denotes the number of DOFs of the fine mesh. These DOFs also determine the fine-mesh approximation of coarse-scale shape functions that incorporate the fine-scale heterogeneity. The prolongation matrix is used to transform coarse DOFs into fine DOFs. It is calculated for each macroelement locally, which allows for parallelization of the process. For the periodic materials, the matrix is calculated only once and is reused for the repeating macroelements.

Macroelement stiffness matrices $\boldsymbol{K}_i^H$, mass matrices $\boldsymbol{M}_i^H$ and vectors $\boldsymbol{f}_i^H$ are calculated by simple algebraic operations using prolongation matrices, without the need for the integration on the coarse level:

$$\boldsymbol{K}_i^H = \boldsymbol{P}_i^T \boldsymbol{K}_i^h \boldsymbol{P}_i, \quad \boldsymbol{M}_i^H = \boldsymbol{P}_i^T \boldsymbol{M}_i^h \boldsymbol{P}_i, \quad \boldsymbol{f}_i^H = \boldsymbol{P}_i^T \boldsymbol{f}_i^h, \tag{4.11}$$

where matrices $\boldsymbol{K}_i^h$, $\boldsymbol{M}_i^h$ and vectors $\boldsymbol{f}_i^h$ are assembled only in macroelements K_i. Note that $\boldsymbol{K}_i^h$ was already computed when solving problems (4.7)–(4.8) and (4.9)–(4.10).

After assembling on the coarse level, the following system of algebraic linear equations or the eigenvalue problem is solved:

$$\text{statics: } \boldsymbol{K}^H \boldsymbol{u}^H = \boldsymbol{f}^H, \tag{4.12}$$

$$\text{free vibrations: } \boldsymbol{K}^H \boldsymbol{u}_j^H = \omega_j^2 \boldsymbol{M}^H \boldsymbol{u}_j^H. \tag{4.13}$$

After obtaining $\boldsymbol{u}^H$, fine-mesh DOFs can be calculated and the solution on the fine-mesh level can be reproduced using this downscale operation in each macroelement:

$$\boldsymbol{u}_i^h = \boldsymbol{P}_i \boldsymbol{u}_i^H. \tag{4.14}$$

5. Numerical model validation

The numerical multiscale model is presented in Fig. 13. The domain is discretized with 2D plane stress state macroelements in such a way that each cell of the mesostructure is treated as a single macroelement. Periodicity of the mesostructures enables the construction of a multiscale model using only one macroelement for each beam type. For each macroelement, the auxiliary triangular mesh with size $h < 0.7$ mm is introduced, which results in the following numbers of fine-scale elements: B1 — 408, B2 — 616, B3 — 498, B4 — 490. Material parameters are determined on the basis of the results presented in Section 2.4.

The static bending tests are modeled with constant distributed loading applied on the top edge of $2h$ length with a resultant force equal to F and located 10 cm from the fixed support, as in the experiments.

An extra mass is added in the dynamic tests to simulate the accelerometer and the wire which was attached to the specimens during the experiments. The mass is distributed on the bottom of the last macroelement and is spread on the area of 1 mm × 10 mm.

The multiscale analysis is accompanied by reference fine-mesh models solved directly with FEM. The global meshes are constructed by gluing together meshes of macroelement and have the following total numbers of DOFs: B1 — 10 230, B2 — 15 202, B3 — 12 078, B4 — 12 782.

5.1. Bending tests

Fig. 14 presents the deflection lines of the beams in the numerical simulations and in the experiments recorded for selected forces. The forces were chosen from diagram 9 so that specimens stayed within the linear range.

The experimental deflection lines were generated by the DIC method. From the documented photos of the experiments, it was observed that the fixed support actually allowed some slight rotation. The angles of this rotation were measured by the DIC analysis and

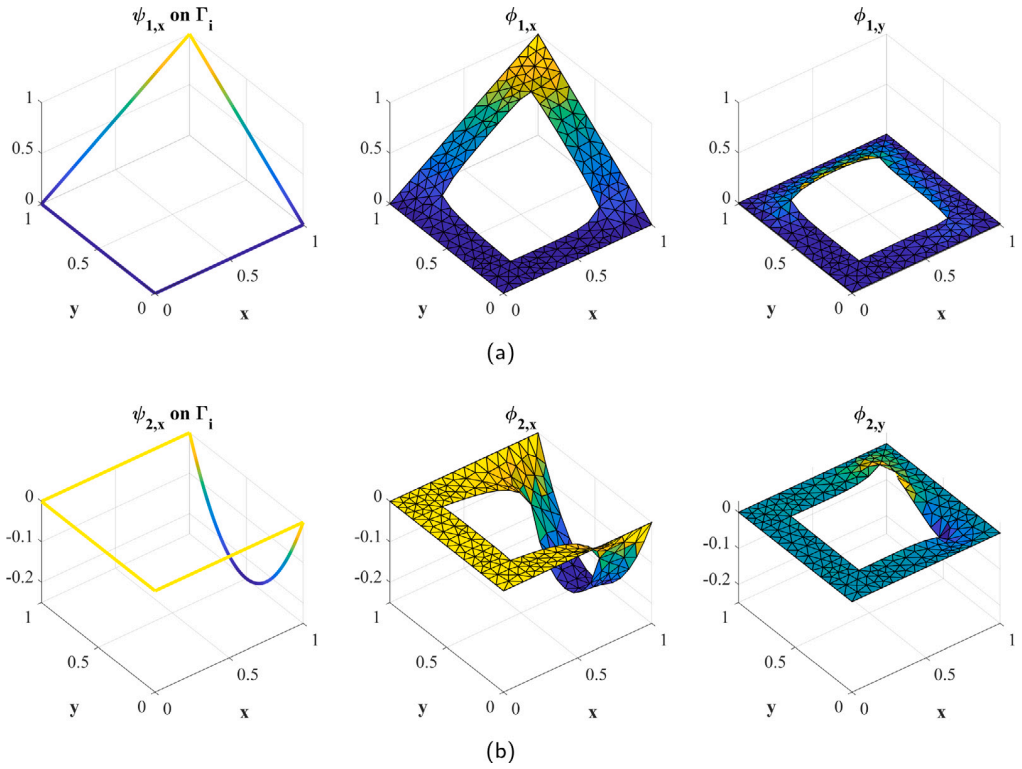

Fig. 11. Juxtaposition of input functions ψ on Γ_i and resulting multiscale shape functions of vertex (a) and higher-order mid-edge (b).

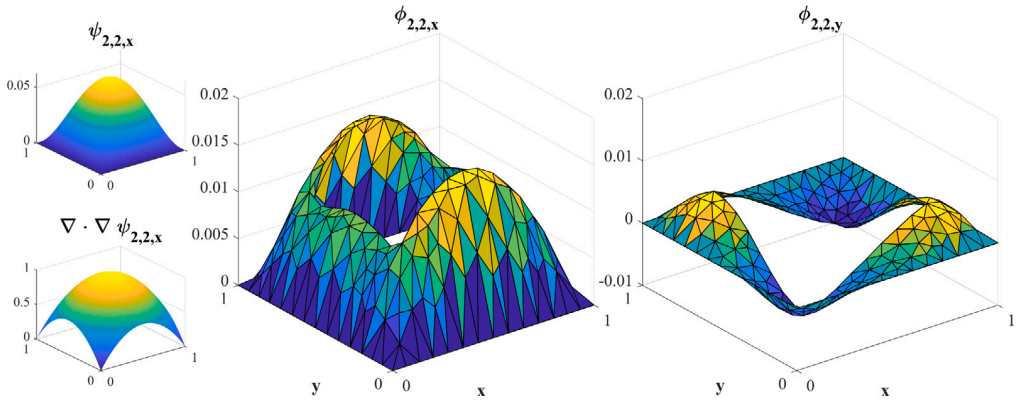

Fig. 12. Juxtaposition of hierarchical bubble function for $p = 2$, source term functions $\nabla \cdot \nabla \psi$, and resulting bubble multiscale shape function.

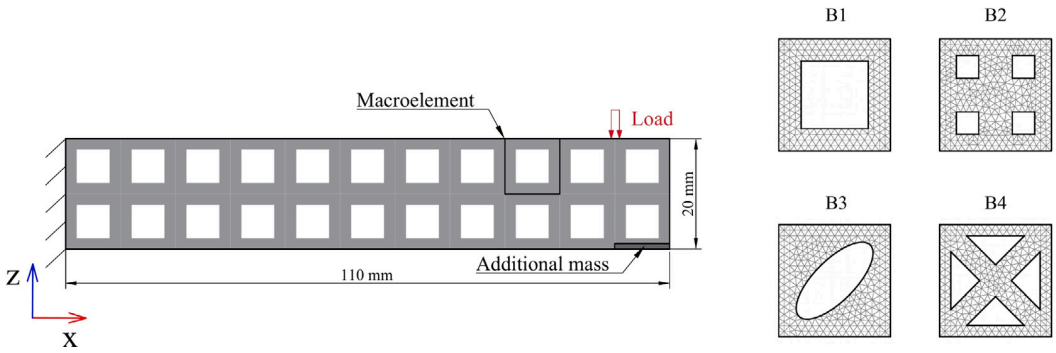

Fig. 13. Beam MsFEM model (on the left) and fine-mesh discretization of macroelements (on the right).

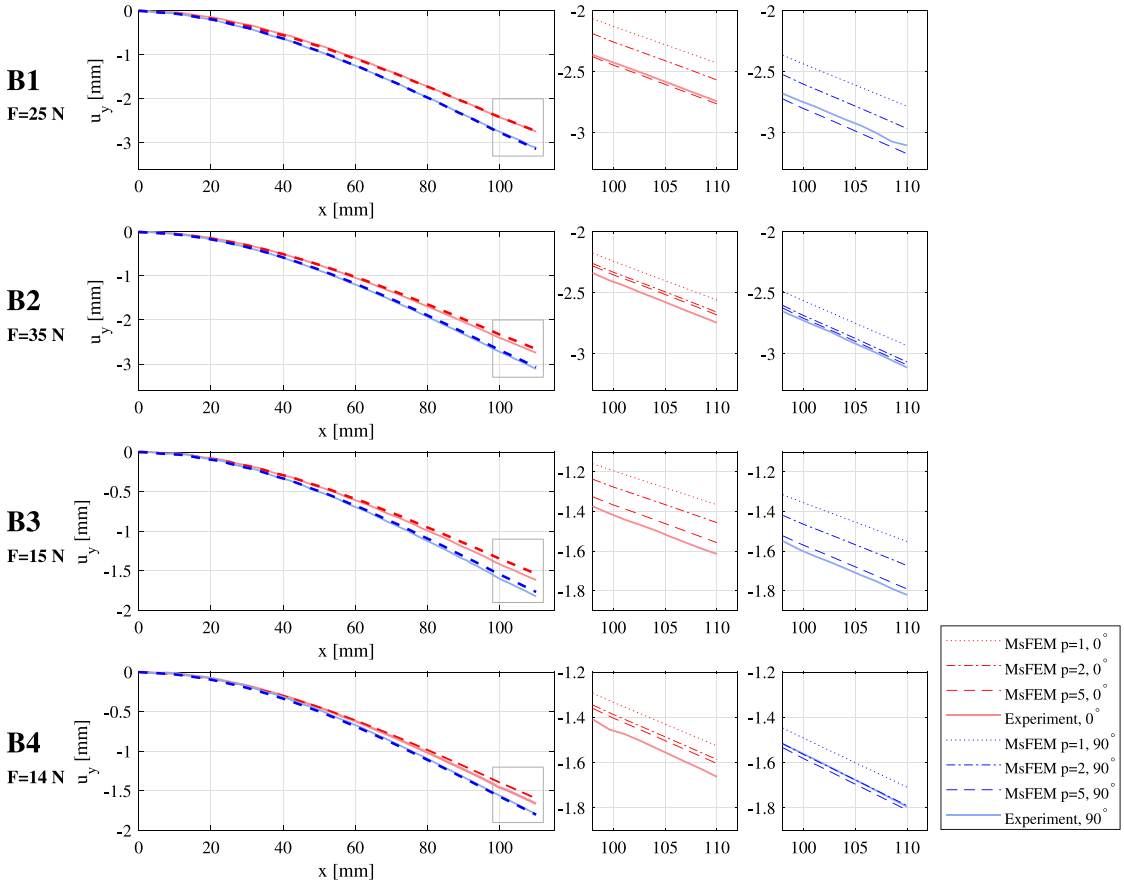

Fig. 14. Deflection line measured on the top edge of the beams obtained through DIC analysis (experiment) and the numerical simulations with MsFEM ($p = 1, 2, 5$).

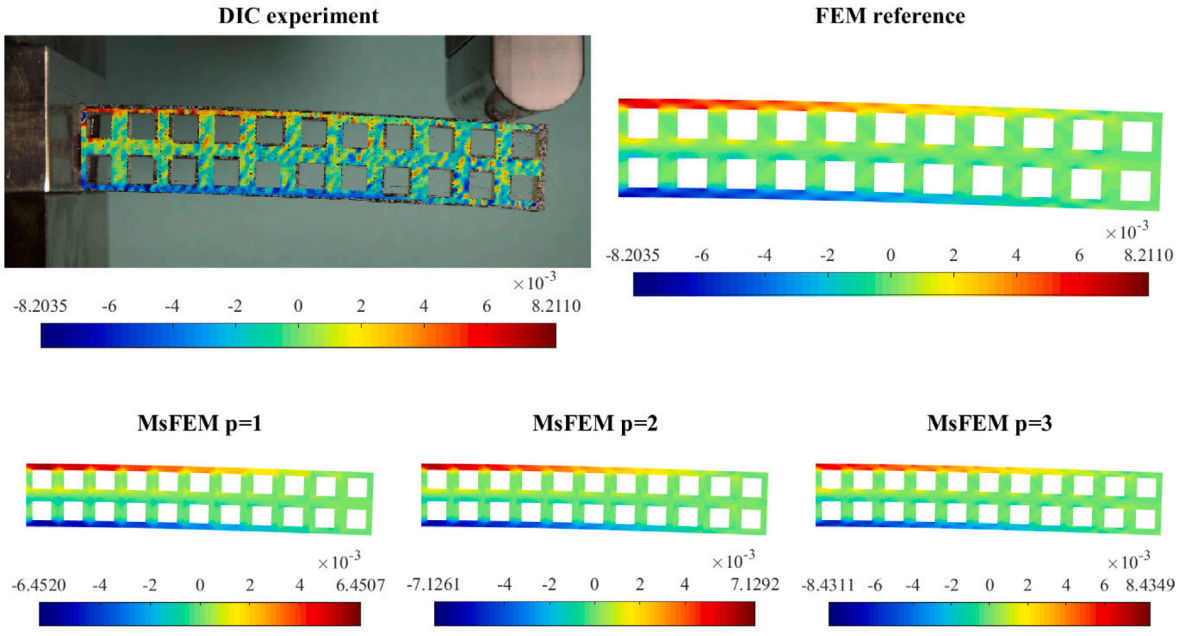

Fig. 15. ϵ_{xx} strain distribution maps of beam $B1_0$ obtained from the DIC analysis, the numerical simulation with the FEM reference model, and the MsFEM models for different p.

accommodated in the deflection lines in order to compensate for the non-ideal gripping.

To keep the diagrams legible, only deflection lines computed by MsFEM with $p = 5$ were shown. As can be seen, the proposed multiscale

Table 4
Maximum deflection measured in mm.

Beam type	Layer orientation	MsFEM $p = 1$ (nDOFs = 72)	MsFEM $p = 2$ (nDOFs = 186)	MsFEM $p = 3$ (nDOFs = 300)	MsFEM $p = 4$ (nDOFs = 414)	MsFEM $p = 5$ (nDOFs = 528)	FEM	Exp.
B1	0°	−2.4281	−2.5673	−2.7332	−2.7514	−2.7636	−2.7663	−2.7
B1	90°	−2.7834	−2.9663	−3.1383	−3.1593	−3.1728	−3.1756	−3.1
B2	0°	−2.5594	−2.6582	−2.6604	−2.6689	−2.6806	−2.6967	−2.7
B2	90°	−2.9329	−3.0672	−3.0695	−3.0795	−3.0913	−3.1109	−3.1
B3	0°	−1.3663	−1.4569	−1.5370	−1.5447	−1.5577	−1.5636	−1.6
B3	90°	−1.5518	−1.6734	−1.7661	−1.7746	−1.7915	−1.7994	−1.8
B3	0°	−1.5261	−1.5865	−1.5950	−1.6027	−1.6040	−1.6083	−1.7
B4	90°	−1.7085	−1.7901	−1.8006	−1.8084	−1.8099	−1.8147	−1.8

model with higher-order shape functions successfully captured the deflection line observed in the experiment. Indeed, the effects of the orthotropic properties of the 3D printed material were measurable in the experiment and were reproduced through the proposed multiscale approach.

In the enlarged sections of the diagrams, deflection lines of $p = 1$ and $p = 2$ MsFEM models were shown. It can be observed that for a lower p the multiscale model predicts a stiffer response of the beams under load.

In order to make quantitative judgments, a summary of maximum deflections of MsFEM $p = 1 - 5$ models, FEM reference models, and the experiment as well as the number of DOFs for multiscale models, are presented in Table 4. It can be observed that the results of multiscale models converge with the results of FEM reference models, which correlate well with the experiment. One should also note that the results for $p = 5$ were obtained with 20 times fewer DOFs than the number used in the FEM reference model, and faster.

Finally, in Fig. 15, maps of dominating strain component ϵ_{xx} for beam $B1_0$ obtained with the DIC technique, FEM, and MsFEM are compared. The DIC map was generated using a grid of virtual markers that are used to measure the displacement field. The markers of size 30×30 pixels were distributed evenly over the entire surface of the beams, excluding openings, which were masked during mesh generation. The actual size of the markers was close to 0.75×0.75 mm, which is about twice the diameter of the nozzle used for printing specimens. In order to compare the numerical and experimental results, the DIC map was plotted in the same range as the map of the FEM model.

The corresponding maps are qualitatively similar. The primary difference is observed in the maximum and minimum values. For a low p, the extreme values are smaller than in the reference solution that correlates with the predicted deflection lines. When p is increased, these values converge with the reference solution.

5.2. Dynamic tests

A comparison between the experimental and numerical results for dynamic tests is shown in Fig. 16 and in Table 5. The diagram depicts the first natural frequencies obtained in the experiment and by MsFEM and FEM.

The FEM reference results are within 5% of relative error with respect to the experiment. The closest one was observed for beam $B4_{90}$. The orthotropic properties influenced the results that were obtained by the numerical model and correlate well with the experimental results for B1, B3, and B4 beams. All the results obtained by MsFEM predict higher frequency responses than the FEM reference models. The maximum error of MsFEM models for $p = 1$ is equal to 7% in comparison with the reference results. However, when the order of the multiscale approximation is increased, the natural frequency converges to the reference solution and it is almost equal to FEM results for $p = 5$ for all the beam types.

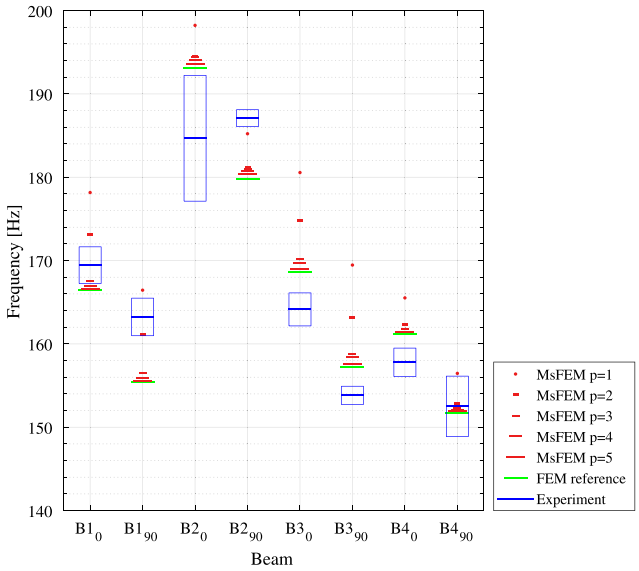

Fig. 16. Comparison of the natural frequency of 3D printed beams measured throughout the experiment, and calculated by MsFEM and FEM.

5.2.1. Influence of bubble multiscale shape functions

The aim of this numerical test was to examine the influence of the inclusion of the bubble multiscale shape functions in MsFEM models on the results. Fig. 17 depicts converges of the natural frequencies of modes 1, 5 and 20 to the reference solution with the increase of p.

As expected, the error of natural frequencies of higher modes predicted by MsFEM with linear shape functions is significant and equals even up to 50% for the 20th mode of vibration. This error, however, can be reduced by increasing the number of multiscale basis functions of higher order. It can also be observed that the use of the bubble multiscale functions reduces further error, especially for the higher modes.

6. Conclusions

An application of MsFEM to mechanical analysis and therefore to the reliable design of 3D printed elements was addressed in the paper. A three-scale approach was presented: on the microlevel, the orthotropic material parameters are experimentally homogenized, then the mesostructure that may be the effect of design optimization is built into the MsFEM shape functions, and the mechanical analysis is finally performed at the macroscale. The presented concept was validated by comparison of numerical modeling with experiments conducted on 3D printed ABS beams with various layer orientations and mesostructures. High-order hierarchical approximations of order up to 5 showed the potential of modified MsFEM. The maximum deflection error in the static bending tests for $p = 1$ was 10%–15% and for $p = 5$ it was

Table 5
Natural frequency measured in Hz.

Beam type	Layer orientation	MsFEM $p = 1$	MsFEM $p = 2$	MsFEM $p = 3$	MsFEM $p = 4$	MsFEM $p = 5$	FEM	Exp.
B1	0°	178.2	173.2	167.6	167.0	166.6	166.5	169.4 ± 2.2
B1	90°	166.4	161.2	156.5	155.9	155.6	155.5	163.2 ± 2.3
B2	0°	198.2	194.5	194.4	194.1	193.6	193.1	184.7 ± 7.6
B2	90°	185.2	181.1	181.0	180.7	180.4	179.8	187.1 ± 1.0
B3	0°	180.6	174.8	170.1	169.7	169.0	168.7	164.1 ± 2.0
B3	90°	169.5	163.2	158.8	158.4	157.6	157.2	153.8 ± 1.1
B3	0°	165.5	162.3	161.8	161.4	161.4	161.1	157.8 ± 1.7
B4	90°	156.5	152.8	152.4	152.0	152.0	151.7	152.5 ± 3.6

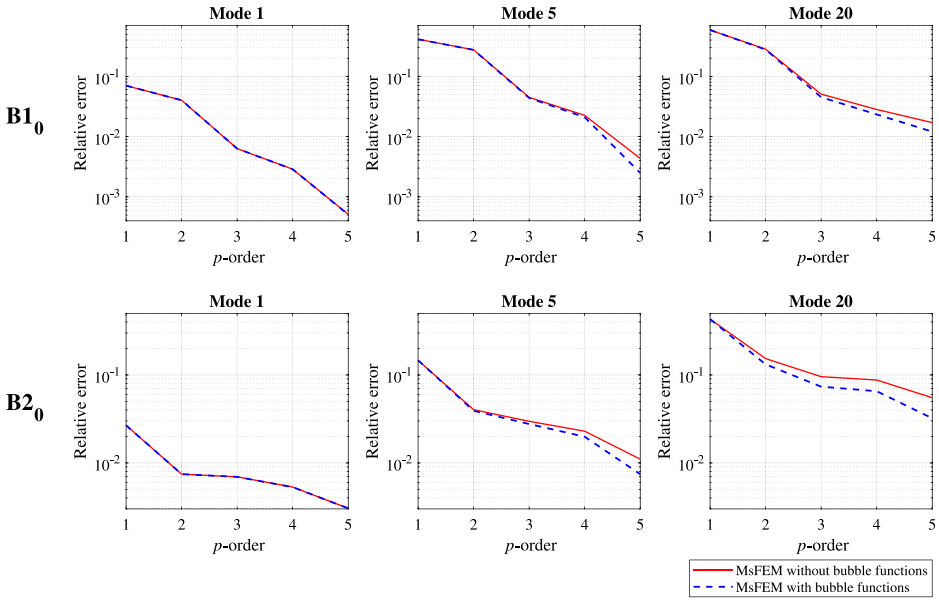

Fig. 17. p-convergence to reference FEM solutions of the natural frequency of modes 1, 5, and 20, of MsFEM solutions and the difference when using multiscale bubble functions.

reduced to 5%–2%. These errors, besides the typical numerical error, include the error of the assumed model (e.g. the plane stress state or the elastic range) and the upscaling error, since the mesoscale details are incorporated into the macroscale by the MsFEM approach. The numerical results converge to the FEM reference solution. Moreover, the application of the higher-order MsFEM was extended to the free vibration simulation. In the dynamic tests, the natural frequency of the beams was captured by the FEM reference solution and MsFEM $p = 5$ within 5% error in relation to the experimental results. The numerical tests revealed that higher-order functions can accurately represent free vibration even for higher modes of vibrations due to the application of inner (bubble) shape functions, e.g. for the 20th mode the error was less than 2% in relation to the reference FEM solution.

In conclusion, the experimental validation confirmed that MsFEM upscaling can be successfully used for efficient static and dynamic modeling of 3D printed parts with mesostructure.

CRediT authorship contribution statement

Mateusz Dryzek: Conceptualization, Methodology, Resources, Investigation, Data curation, Formal analysis, Software, Visualization, Writing – original draft. **Witold Cecot:** Conceptualization, Methodology, Formal analysis, Writing – review & editing, Supervision, Project administration, Funding acquisition. **Marcin Tekieli:** Data curation, Visualization, Writing – original draft, Writing – review & editing.

Declaration of competing interest

The authors declare that they have no known competing financial interests or personal relationships that could have appeared to influence the work reported in this paper.

Data availability

Data will be made available on request.

Acknowledgments

The authors would like to thank Professor Arkadiusz Kwiecień and Jarosław Chełmecki of the Cracow University of Technology for their very helpful assistance with the experiments. This work was supported by Grant No. 2017/25/B/ST8/02752, funded by National Science Centre, Poland.

References

[1] T. Hou, X. Wu, A multiscale finite element method for elliptic problems in composite materials and porous media, J. Comput. Phys. 134 (1) (1997) 169–189, URL http://www.sciencedirect.com/science/article/pii/S0021999197956825.

[2] U.K. Roopavath, D.M. Kalaskar, 1 - Introduction to 3D printing in medicine, in: D.M. Kalaskar (Ed.), 3D Printing in Medicine, Woodhead Publishing, Cambridge, 2017, pp. 1–20, URL http://www.sciencedirect.com/science/article/pii/B9780081007174000016.

[3] S. Curran, P. Chambon, R. Lind, L. Love, R. Wagner, S. Whitted, D. Smith, B. Post, R. Graves, C. Blue, J. Green, M. Keller, Big area additive manufacturing and hardware-in-the-loop for rapid vehicle powertrain prototyping: A case study on the development of a 3-D-printed Shelby Cobra, in: SAE Technical Paper, SAE International, 2016, URL https://doi.org/10.4271/2016-01-0328.

[4] F. Bos, R. Wolfs, Z. Ahmed, T. Salet, Additive manufacturing of concrete in construction: potentials and challenges of 3D concrete printing, Virtual Phys. Prototyp. 11 (3) (2016) 209–225, URL https://doi.org/10.1080/17452759.2016.1209867.

[5] J.F. Rodríguez, J.P. Thomas, J.E. Renaud, Mechanical behavior of acrylonitrile butadiene styrene fused deposition materials modeling, Rapid Protot. J. 9 (4) (2003) 219–230, URL https://doi.org/10.1108/13552540310489604.

[6] P. Makowski, W. Kuś, Wieloskalowe modelowanie struktur wytworzonych z użyciem metody fused deposition modeling (FDM) do zastosowań w medycynie (in Polish), Zesz. Nauk. WSInf 13 (2014) 132–138.

[7] L. Li, Q. Sun, C. Bellehumeur, P. Gu, Composite modeling and analysis for fabrication of FDM prototypes with locally controlled properties, J. Manuf. Process. 4 (2) (2002) 129–141, URL http://www.sciencedirect.com/science/article/pii/S1526612502701394.

[8] J. Martínez, J. Diéguez, E. Ares, A. Pereira, P. Hernández, J. Pérez, Comparative between FEM models for FDM parts and their approach to a real mechanical behaviour, Proc. Eng. 63 (2013) 878–884, URL http://www.sciencedirect.com/science/article/pii/S1877705813014434.

[9] X. Liu, V. Shapiro, Homogenization of material properties in additively manufactured structures, Comput.-Aided Des. 78 (2016) 71–82, URL http://www.sciencedirect.com/science/article/pii/S0010448516300379.

[10] A. Garg, A. Bhattacharya, An insight to the failure of FDM parts under tensile loading: finite element analysis and experimental study, Int. J. Mech. Sci. 120 (2017) 225–236, URL http://www.sciencedirect.com/science/article/pii/S0020740316309596.

[11] J. Xiao, H. Liu, T. Ding, Finite element analysis on the anisotropic behavior of 3D printed concrete under compression and flexure, Addit. Manuf. 39 (2021) 101712, URL https://www.sciencedirect.com/science/article/pii/S2214860420310848.

[12] A.A. Soufivand, N. Abolfathi, S.A. Hashemi, S.J. Lee, Prediction of mechanical behavior of 3D bioprinted tissue-engineered scaffolds using finite element method (FEM) analysis, Addit. Manuf. 33 (2020) 101181, URL https://www.sciencedirect.com/science/article/pii/S2214860420305534.

[13] W. Cecot, M. Oleksy, High order FEM for multigrid homogenization, Comput. Math. Appl. 70 (7) (2015) 1391–1400, URL http://www.sciencedirect.com/science/article/pii/S0898122115003107.

[14] M. Dryzek, W. Cecot, The iterative multiscale finite element method for sandwich beams and plates, Internat. J. Numer. Methods Engrg. 122 (22) (2021) 6714–6735, URL https://onlinelibrary.wiley.com/doi/abs/10.1002/nme.6808.

[15] M. Krówczyński, W. Cecot, A fast three-level upscaling for short fiber reinforced composites, Int. J. Multiscale Comput. Eng. 15 (2016).

[16] G. Alaimo, M. Carraturo, E. Rocca, A. Reali, F. Auricchio, Functionally graded material design for plane stress structures using phase field method, in: Sim-AM 2019 : II International Conference on Simulation for Additive Manufacturing, CIMNE, 2019, pp. 162–173, URL http://hdl.handle.net/2117/334601.

[17] M. Carraturo, P. Hennig, G. Alaimo, L. Heindel, F. Auricchio, M. Kästner, A. Reali, Additive manufacturing applications of phase-field-based topology optimization using adaptive isogeometric analysis, GAMM-Mitt. 44 (3) (2021) e202100013, URL https://onlinelibrary.wiley.com/doi/abs/10.1002/gamm.202100013.

[18] G. Alaimo, S. Marconi, L. Costato, F. Auricchio, Influence of meso-structure and chemical composition on FDM 3D-printed parts, Composites B 113 (2017) 371–380, URL https://www.sciencedirect.com/science/article/pii/S1359836816330037.

[19] J.C. Gerdeen, R.A.L. Rorrer, Engineering Design with Polymers and Composites, CRC Press, Taylor & Francis Group, Boca Raton, 2012, p. 420.

[20] D. Popescu, A. Zapciu, C. Amza, F. Baciu, R. Marinescu, FDM process parameters influence over the mechanical properties of polymer specimens: A review, Polym. Test. 69 (2018) 157–166, URL https://www.sciencedirect.com/science/article/pii/S0142941818306093.

[21] M. Tekieli, S. De Santis, G. de Felice, A. Kwiecień, F. Roscini, Application of Digital Image Correlation to composite reinforcements testing, Compos. Struct. 160 (2017) 670–688, URL https://www.sciencedirect.com/science/article/pii/S0263822316313915.

[22] M. Słoński, M. Tekieli, 2D digital image correlation and region-based convolutional neural network in monitoring and evaluation of surface cracks in concrete structural elements, Materials 13 (16) (2020) URL https://www.mdpi.com/1996-1944/13/16/3527.

[23] I. Babuška, B.A. Szabo, I.N. Katz, The p-version of the finite element method, SIAM J. Numer. Anal. 18 (3) (1981) 515–545, URL https://doi.org/10.1137/0718033.

[24] O. Zienkiewicz, J.D.S. Gago, D. Kelly, The hierarchical concept in finite element analysis, Comput. Struct. 16 (1) (1983) 53–65, URL http://www.sciencedirect.com/science/article/pii/0045794983901475.

[25] W. Cecot, M. Oleksy, The discontinuous Petrov–Galerkin methodology for the mixed multiscale finite element method, Comput. Math. Appl. 95 (2021) 28–40, URL https://www.sciencedirect.com/science/article/pii/S0898122120303692.

[26] S. Soghrati, I. Stanciulescu, Systematic construction of higher order bases for the finite element analysis of multiscale elliptic problems, Mech. Res. Commun. 52 (2013) 11–18, URL http://www.sciencedirect.com/science/article/pii/S0093641313000888.

Chapter 4

Additional experimental validation

Certain detail of experiments depicted in the papers as well as experimental measurements that have not been published are reported in this chapter. Similarly as the other laboratory tests they also have been used for validation of MsFEM based numerical models.

4.1 Tensile and bending tests

The photos of all the specimens used in tests described in Article 4 are presented in this section. Figs. 4.1, 4.2 and 4.3 present photos of specimens used in tensile test with close-ups of the failure zone: T0, T90, T45, respectively. The results of this tests were used to measure the parameters of extrusion-based 3D printed material. Fig. 4.4 presents tested beams with different mesostructures used in static and dynamic tests, as well as close-ups of the failure zones of the B3 beams.

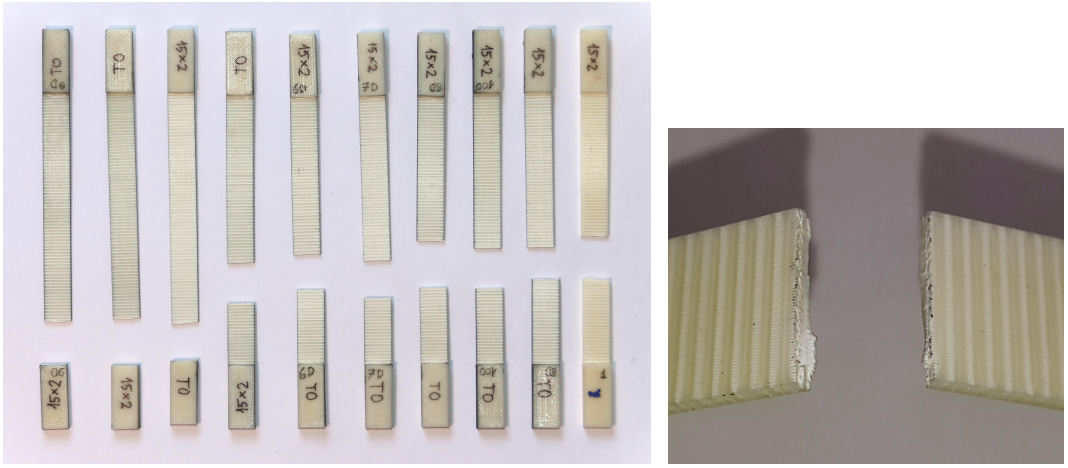

(a) (b)

Figure 4.1: T0 specimens after tensile tests (a). Close-up of a failure zone (b).

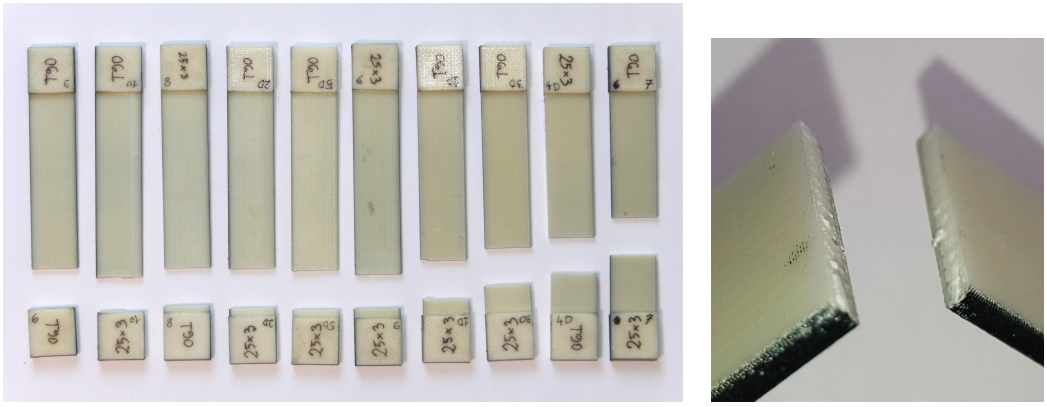

(a) (b)

Figure 4.2: T90 specimens after tensile tests (a). Close-up of a failure zone (b).

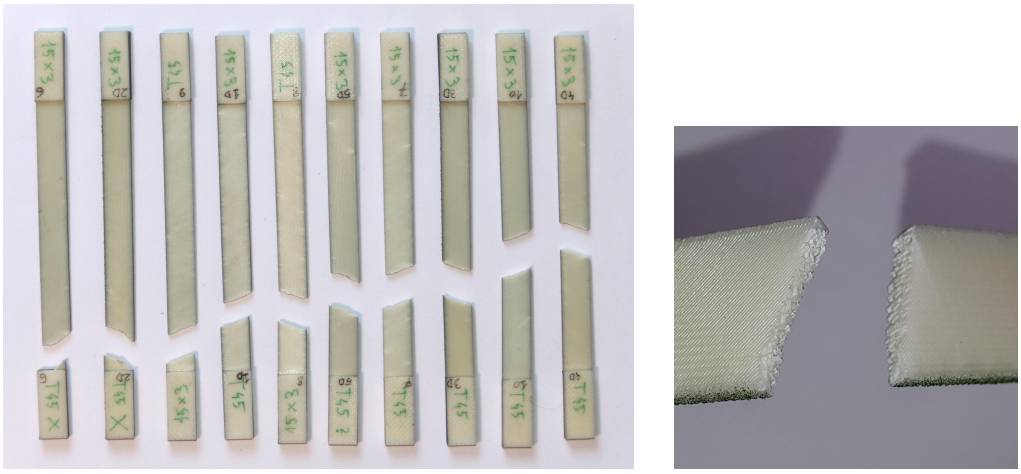

(a) (b)

Figure 4.3: T45 specimens after tensile tests (a). Close-up of a failure zone (b).

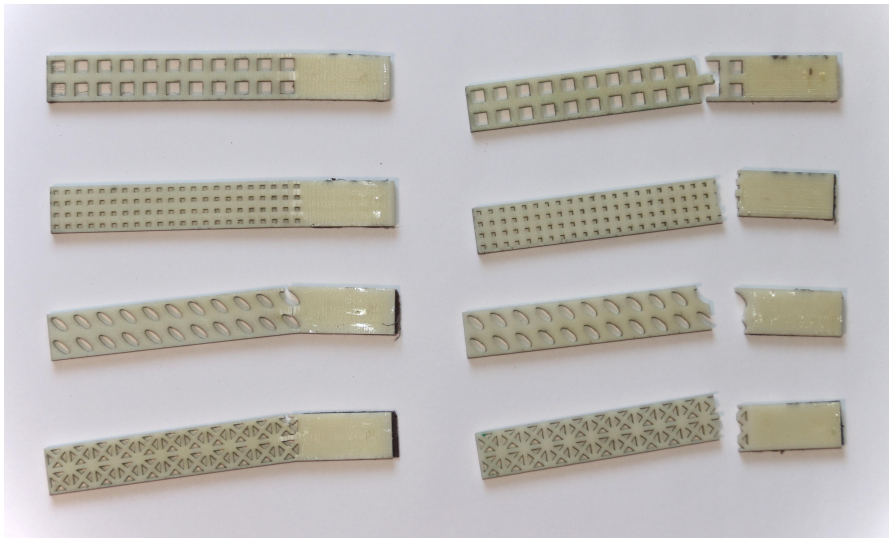

(a)

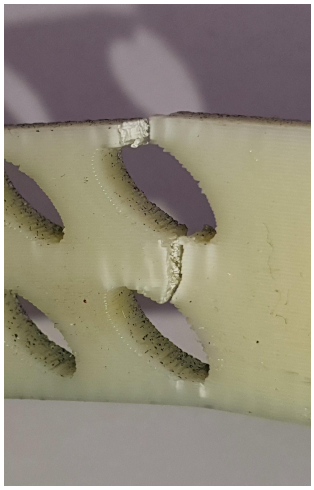

(b)

(c)

Figure 4.4: Beams of types B1-B4 (rows) printed with layer orientations 0° and 90° (columns) after bending tests (a). Close-ups of a failure zone of beam B3 printed with layer orientations 0° (b) and 90° (c).

4.2 Metamaterial of negative Poisson's ratio

The following results were presented at the *41st Solid Mechanics Conference SOLMECH* in Warsaw, 2018, in the talk *Development of the Multiscale Finite Element Method for the Analysis of Advanced Materials*, by M. Dryzek and W. Cecot.

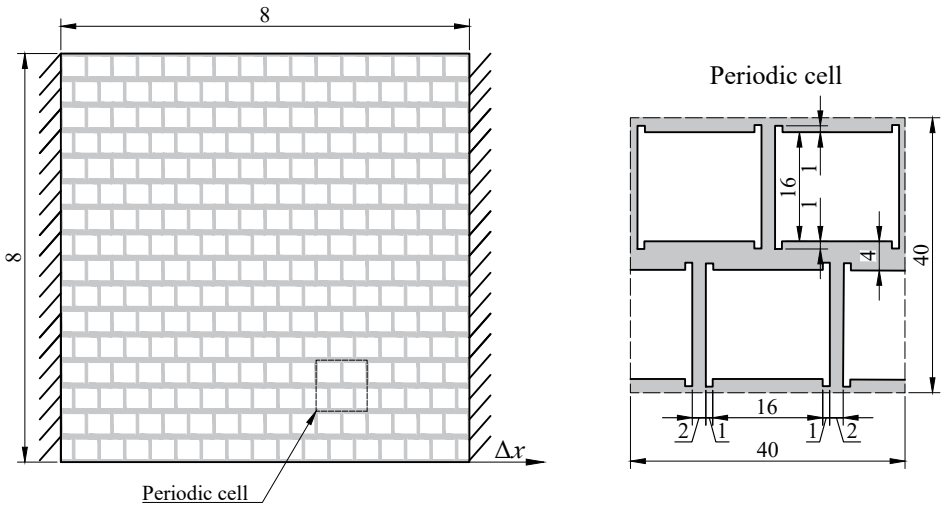

Figure 4.5: Metamaterial model and dimensions of a periodic cell (module 1).

A metamaterial of negative Poisson's ratio was chosen to validate application of MsFEM with higher-order approximation in modeling of its overall global mechanical properties. The value of Poisson's ratio is the negative of the ratio of transverse strain to axial one observed e.g. in the tensile test. If the resulting value is negative, the material increases its cross-section when stretched. Such behavior is mostly attributed to periodic mesoscopic lattice structures that rotate inside when material is stretched. In this test, the chosen mesostructure was proposed and studied in [34]. The considered problem is a plane-stress tensile test of a square domain of 8×8 periodic cells of the mesostructure illustrated in Fig. 4.5. Base material was chosen to have Young's modulus $E = 2$ GPa and Poisson's ratio $\nu = 0.4$. The elongation was set to $\Delta x = 0.1$.

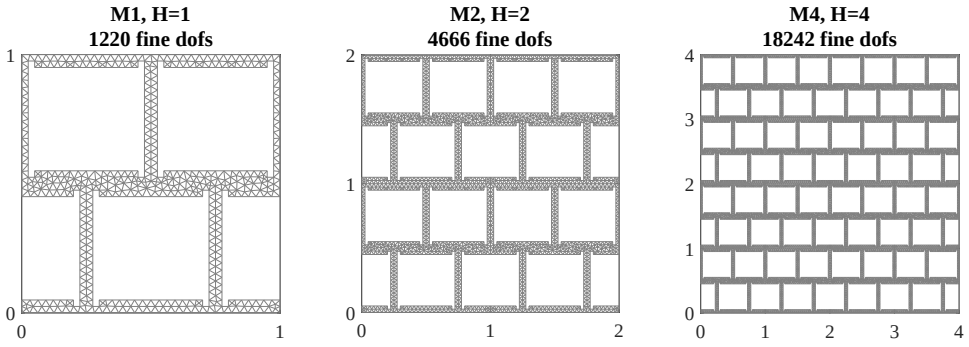

Figure 4.6: Fine mesh of macroelements in multiscale models M1, M2, and M3.

Three multiscale models, M1, M2, and M4, with varying coarse grid size were considered: $H = 1$, $H = 2$, and $H = 4$, respectively. Fig. 4.6 shows fine meshes of macroelements in each model. Note that in the M1 model macroelement is the smallest periodic

cell. The multiscale analysis is accompanied by a reference direct fine-mesh FEM solution. The global mesh is constructed by gluing together meshes of macroelement and have the total of 72130 DoFs.

In the multiscale analysis, multiscale basis functions were constructed using higher-order hierarchical polynomials of order $p = 1 - 5$ with the method described in details in Article 4. The multiscale basis functions were only of nodal and edge type, since no internal load is considered in this problem.

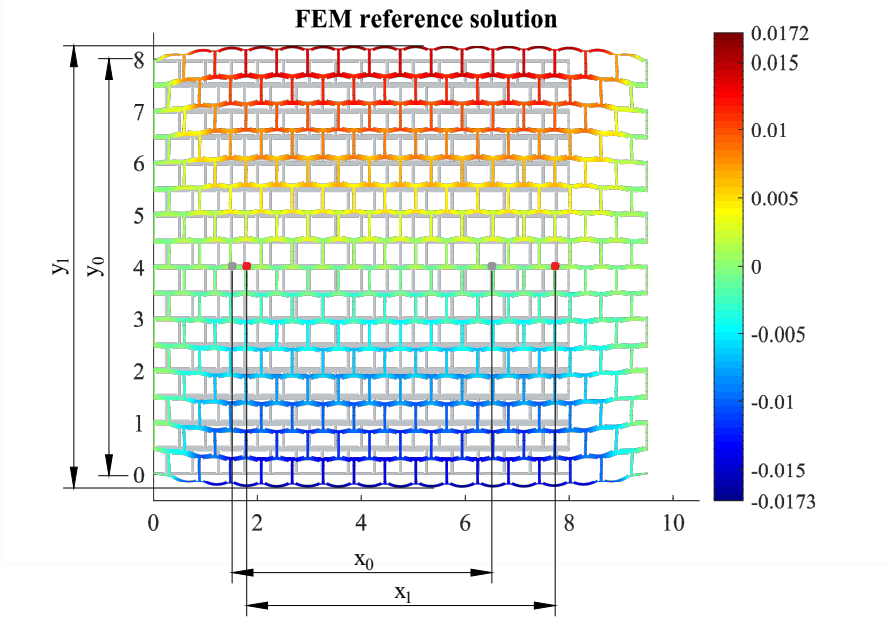

Figure 4.7: The FEM reference solution: Deformed and undeformed mesh. The color indicate displacement u_y in the direction perpendicular to the tensile direction (deformation scaled 15 times, the undeformed structure is presented in the background).

Fig. 4.7 depicts results of the reference model. It can be observed that in the reference model both dimensions of the structure after deformation (x_1 and y_1) are greater than in the initial configuration (x_0 and y_0). Poisson's ratio is calculated using formula:

$$\nu = -\frac{\Delta\varepsilon_y}{\Delta\varepsilon_y}, \tag{4.1}$$

where $\Delta\varepsilon_x = \frac{x_1 - x_0}{x_0}$ is strain in the axial direction and $\Delta\varepsilon_y = \frac{y_1 - y_0}{y_0}$ is strain in the transverse direction. Calculated from the reference model, Poisson's ratio equals -0.35, which correlates very well with the numerical, -0.34, and the experimental results, -0.28 (extrapolated), from [34].

Figs. 4.8-4.10 depict the results of the M1, M2, and M4 models for $p = 1$ and $p = 5$. For the M1 model with linear functions, the deformation in the transverse direction is small and negative resulting in positive Poisson's ratio $\nu = 0.0028$. Asymmetrical displacement u_y can be explained by the asymmetry of mesostructure in the macroelements. For M1 model with $p = 5$ order, it can be observed that Poisson's ratio is negative, $\nu = -0.11$, and the downscaled solution more closely resembles the reference solution. For the M2 and M4 models, they predict negative Poisson's ratio as well.

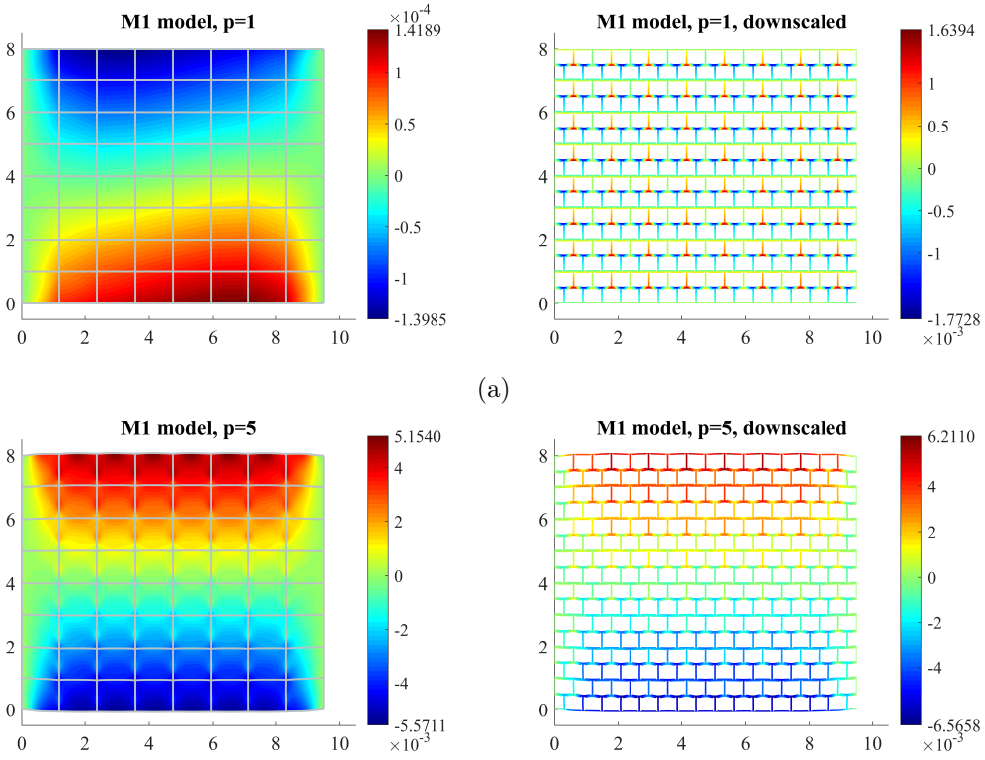

Figure 4.8: M1 model: Displacement u_y on to deformed coarse grid and solution downscaled on fine mesh, for $p = 1$ (a) and $p = 5$ (b)(deformation scaled 15 times).

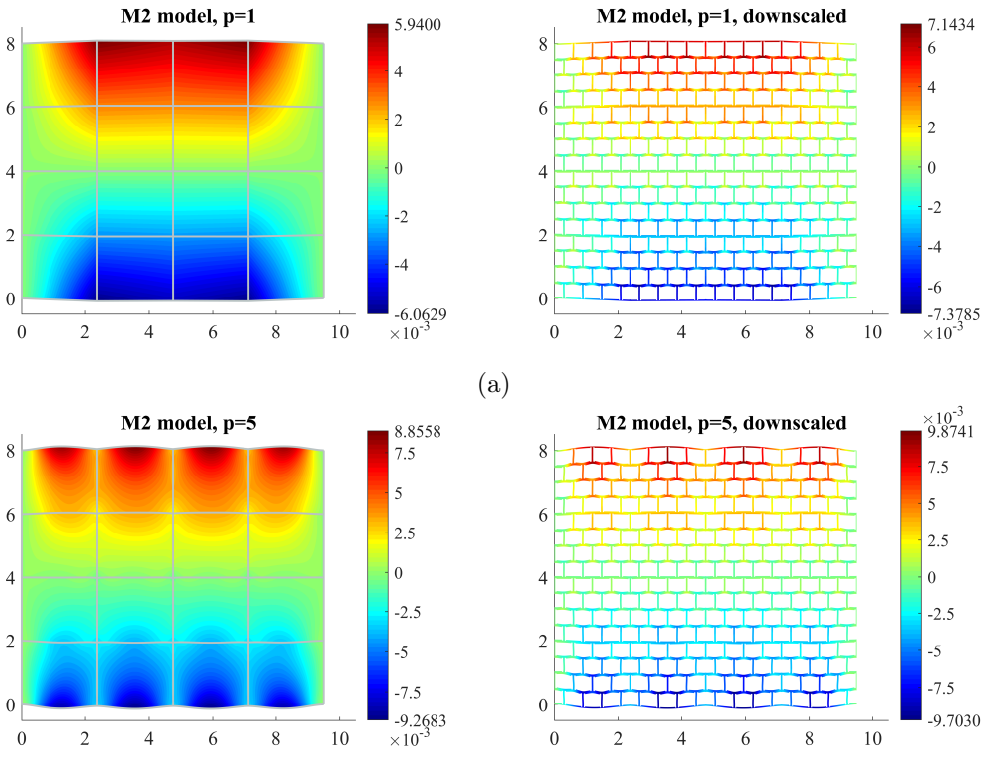

Figure 4.9: M2 model: Displacement u_y on to deformed coarse grid and solution downscaled on fine mesh, for $p = 1$ (a) and $p = 5$ (b) (deformation scaled 15 times).

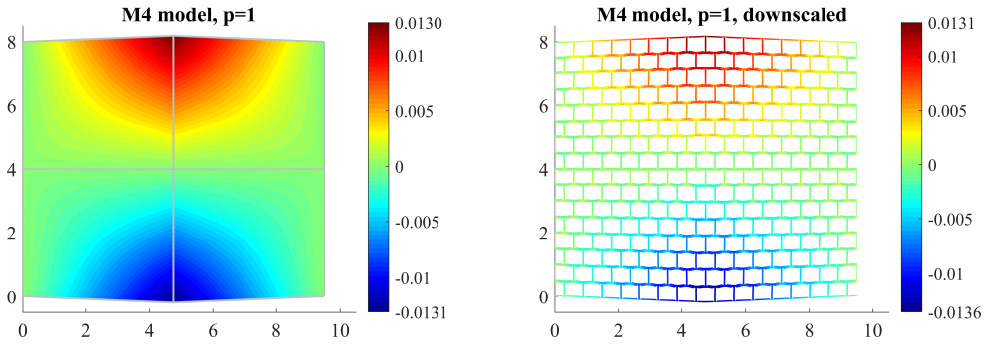

(a)

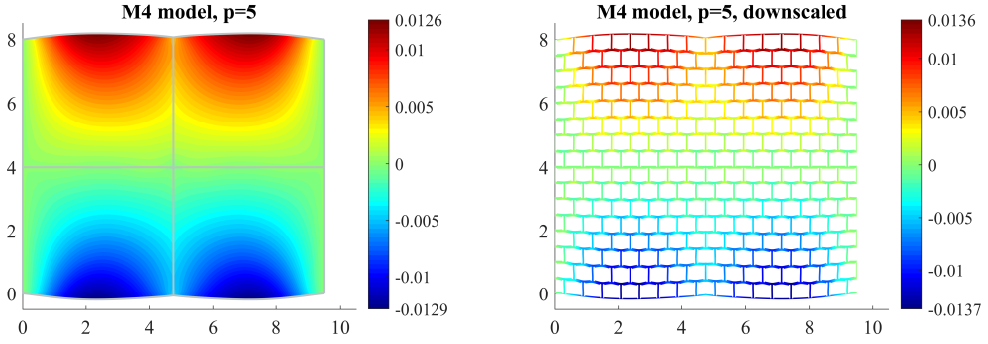

(b)

Figure 4.10: M4 model: Displacement u_y on to deformed coarse grid and solution downscaled on fine mesh, for $p = 1$ (a) and $p = 5$ (b) (deformation scaled 15 times, the coarse elements are visible in the left hand side figure).

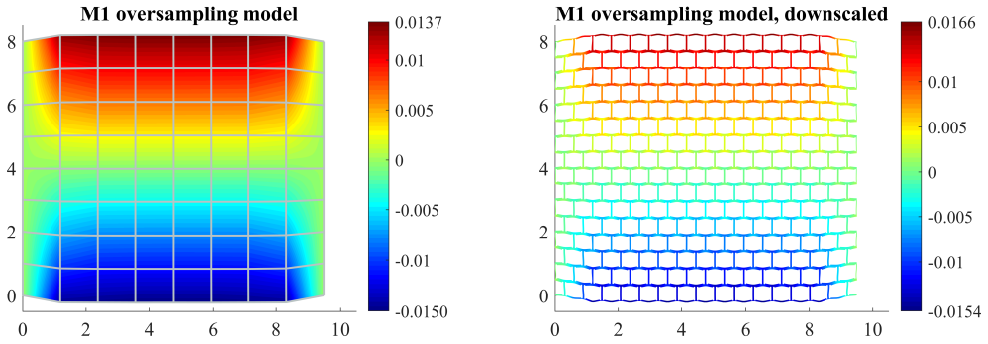

Figure 4.11: M1 model with oversampling technique ($p = 1$): Displacement u_y on to deformed coarse grid and solution downscaled on fine mesh (deformation scaled 15 times, the coarse elements are visible in the left hand side figure).

A strong resonance effect is observed. It can occur in multiscale analysis of challenging structures such as the one studied here. The next Fig. 4.11 presents results of model M1 achieved with the oversampling technique (see Sect. 2.3.1). The oversampling domain was chosen to be $3H \times 3H$. In the results of the displacements u_y no interference with the coarse grid is visible.

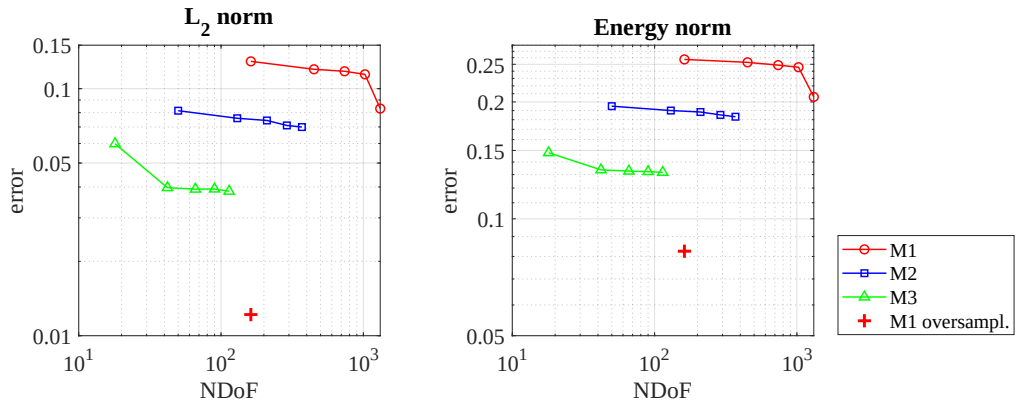

Figure 4.12: Relative error measured in L_2 and energy norms of the multiscale solution obtained by models M1, M2, and M4 with increasing number of DoFs (NDoFs) implied by increasing order of approximation p.

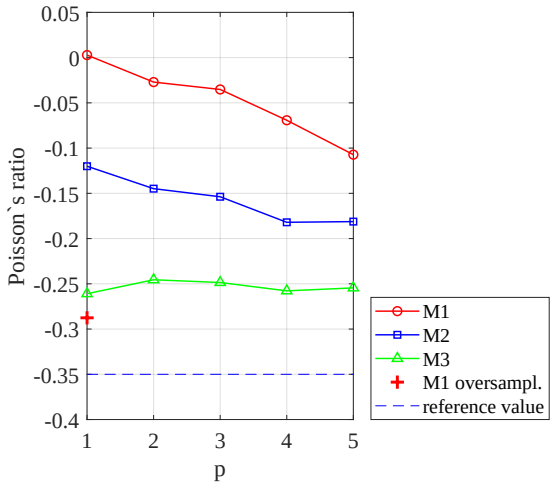

Figure 4.13: Poisson's ratio versus order of approximation (reference value is from the FEM reference model.

Next, the convergence of the multiscale solution with respect to the reference solution is studied. The diagrams in Fig. 4.12 show the relative error measured in L_2 and energy norms, relative to the reference solution, versus number of DoFs in the multiscale model. It can be observed that the increasing order of approximation p decreases the error for all the models e.g. for the M1 model , from 13% to 8% in L_2 norm. However, with decreasing macroelement size from $H = 4$ to $H = 1$ the error increases, e.g. for $p = 1$, the L_2 norm error of model M4 is 6.0% and of model M1 is 13%. It confirms the resonance effect i.e. proportionality of the error to ε/H ratio, where ε is the characteristic small-scale length. Therefore, the M1 model with the oversampling technique delivers the best results with an error of about 1% in L_2 norm and 8% in energy norm.

Finally, Fig. 4.13 depicts the values of computed Poisson's ratios in all the conducted numerical experiments. These results correlate with previous convergence plots. The closest value of Poisson's ratio to the reference solution -0.35 was achieved with the M1 model with the oversampling technique, $\nu = -0.28$.

Chapter 5

Conclusions and discussion

Detailed testing and validation of upscaling techniques are essential for reliable modeling of complex materials. The objectives of the dissertation were development and testing of the multiscale finite element method in the context of advanced materials. The work presents a recent overview of the method and its original modifications, numerical tests, and experimental validation.

The applicability of MsFEM was demonstrated on linear problems of steady-state flow in heterogeneous media and elastic deformation of heterogeneous, anisotropic material with mesostructure. The reduction of number of DoFs, even by four orders of magnitude, was possible without introducing a significant additional approximation error. Three possible types of modification to MsFEM were tested to deal with this additional error: oscillation of boundary conditions, introduction of new multiscale basis functions, and iterative correction of the multiscale solution. In some cases, i.e. iterative schemes, it is even possible to resolve the problem with fine-mesh accuracy.

One of the objectives of this research was to test hierarchical multiscale basis functions. It was shown through numerous tests and experimental validations that the error of the multiscale solution can be reduced by increasing the number of DoFs even in the extreme example of negative Poisson's ratio material. This way of constructing functions was also considered in beam and plate problems creating an anisotropic approximation. When it was combined with the iterative corrector scheme, it was possible to increase the rate of convergence of the method, giving a new possibility of reaching the desired accuracy. Moreover, a new way of building multiscale basis functions and increasing the number of DoFs was proposed by using B-splines. It was shown that this approach outperforms MsFEM with the oversampling technique. However, a strong resonance effect was observed with this approach. The effect can be reduced by increasing the order of the B-spline used.

The MsFEM approach was validated using experimental tests of 3D printed material. A three-scale approach was proposed: on the microlevel the orthotropic material parameters were experimentally homogenized, then the designed mesostructure was built into the MsFEM shape functions, and the mechanical analysis was finally performed at the macroscale. The multiscale solution correlated well for a static test, yielding a 2-5% difference with the experiment for higher-order multiscale functions. In the dynamic tests, the measured natural frequencies of the tested specimens were captured by the MsFEM model within 5% of error.

Experimental testing included vision-based measurements to obtain deformation and strain fields. The dynamic test with the use of accelerometer contributed to the field of experimental testing of 3D printed material. In addition, a novel material testing of 3D

printed ABS material using positron annihilation lifetime spectroscopy was proposed.

The following original contributions are associated with this dissertation:

1. Application of B-spline functions in the MsFEM framework, including implementation of the idea and its numerical examination for steady-state flow problems in heterogeneous media.

2. Adaptation of MsFEM to the analysis of sandwich beams and plates using higher-order hierarchical multiscale functions and the iterative corrector scheme. Implementation and numerical examination of the idea on examples of 2D and 3D structures and validation by experimental data was performed.

3. Novel experimental testing of 3D printed ABS material and samples made of it using digital image correlation, accelerometers, and positron annihilation lifetime spectroscopy.

4. Application of MsFEM to mechanical analysis of 3D printed elements and validation by comparison of numerical modeling with experiments.

5. Testing MsFEM for the problem of metamaterial of negative Poisson's ratio.

There is a wide range of disciplines that the application of advanced materials concerns, highlighting particularly important ones for society, including medicine, building engineering, and military and defense. The author believes that the study of digital representation, modeling of composite materials, and development of MsFEM may be beneficial to the process of designing future materials, accelerating the progress in some of the aforementioned disciplines. Further research on the development of the method may include implementation and testing of other constitutive laws in the multiscale framework, e.g., to predict whole mechanical response of the 3D printed elements including nonlinear range. Another idea for future research may concern technical difficulties in preparing the MsFEM model mentioned by many authors, i.e. the difficulty of meshing the fine-scale details in particular close to the boundary of macroelements that may lead to very irregular meshes and approximation spaces with poor properties. This could be potentially improved by decoupling fine mesh from coarse grid using geometrically unfitted finite element methods [3]. In this methods the problems are solved using the standard FEM, but the variational formulation is modified so that interfaces and boundaries are integrated in a fine mesh that is not fitted to the geometry. This may ease the process of building the multiscale model and stimulate application of MsFEM in commercially available software based on the standard finite element algorithms.

Bibliography

[1] I. Babuška, G. Caloz, and J. Osborn. Special finite element method for a class of second order elliptic problems with rough coefficients. *SIAM Journal on Numerical Analysis*, 31:945–981, 1994. 18

[2] A. Bensoussan, J. Lions, and G. Papanicolaou. *Asymptotic Analysis for Periodic Structures*. Contributions to Economic Analysis. North-Holland Publishing Company, 1978. 14

[3] S. Bordas, E. Burman, M. Larson, and M. Olshanskii. *Geometrically Unfitted Finite Element Methods and Applications: Proceedings of the UCL Workshop 2016*. Springer, 01 2017. 94

[4] F. Casadei, J. Rimoli, and M. Ruzzene. A geometric multiscale finite element method for the dynamic analysis of heterogeneous solids. *Computer Methods in Applied Mechanics and Engineering*, 263:56 – 70, 2013. 20, 21, 101

[5] F. Casadei, J. Rimoli, and M. Ruzzene. Multiscale finite element analysis of wave propagation in periodic solids. *Finite Elements in Analysis and Design*, 108:81–95, 2016. 20

[6] W. Cecot and M. Oleksy. High order FEM for multigrid homogenization. *Computers & Mathematics with Applications*, 70(7):1391 – 1400, 2015. High-Order Finite Element and Isogeometric Methods. 19, 21, 101, 104

[7] P. Degond, A. Lozinski, B. Muljadi, and J. Narski. Crouzeix-raviart MsFEM with bubble functions for diffusion and advection-diffusion in perforated media. *Communications in Computational Physics*, 17, 09 2013. 20

[8] L. Durlofsky, Y. Efendiev, and V. Ginting. An adaptive local–global multiscale finite volume element method for two-phase flow simulations. *Advances in Water Resources*, 30(3):576–588, 2007. 22

[9] Y. Efendiev, V. Ginting, T. Hou, and R. Ewing. Accurate multiscale finite element methods for two-phase flow simulations. *Journal of Computational Physics*, 220(1):155 – 174, 2006. 22

[10] Y. Efendiev, V. Ginting, and T. Y. Hou. Multiscale Finite Element Methods for Nonlinear Problems and Their Applications. *Communications in Mathematical Sciences*, 2(4):553 – 589, 2004. 18

[11] Y. Efendiev and T. Hou. *Multiscale Finite Element Methods: Theory and Applications*. Surveys and Tutorials in the Applied Mathematical Sciences. Springer New York, 2009. 13

[12] Y. R. Efendiev, T. Y. Hou, and X.-H. Wu. Convergence of a nonconforming multiscale finite element method. *SIAM Journal on Numerical Analysis*, 37(3):888–910, 2000. 20

[13] O. Egeland and P. O. Araldsen. SESAM-69 — a general purpose finite element method program. *Computers & Structures*, 4(1):41–68, 1974. 22

[14] F. Feyel and J. L. Chaboche. FE^2 multiscale approach for modelling the elastoviscoplastic behaviour of long fiber SiC/Ti composite materials. *Computer Methods in Applied Mechanics and Engineering*, 183:309–330, 2000. 13

[15] J. Fish. *Practical Multiscaling*. Wiley, 2013. 13, 18

[16] J. Fish and V. Belsky. Multigrid method for periodic heterogeneous media part 1: Convergence studies for one-dimensional case. *Computer Methods in Applied Mechanics and Engineering*, 126(1):1–16, 1995. 18

[17] J. Fish and V. Belsky. Multigrid method for periodic heterogeneous media part 2: Multiscale modeling and quality control in multidimensional case. *Computer Methods in Applied Mechanics and Engineering*, 126(1):17–38, 1995. 18

[18] P. Fu, H. Liu, and X. Chu. An efficient multiscale computational formulation for geometric nonlinear analysis of heterogeneous piezoelectric composite. *Composite Structures*, 167:191 – 206, 2017. 18, 104

[19] K. Gao, S. Fu, and E. T. Chung. A high-order multiscale finite-element method for time-domain acoustic-wave modeling. *Journal of Computational Physics*, 360:120 – 136, 2018. 20, 21, 101, 104

[20] M. G. D. Geers, V. G. Kouznetsova, and W. A. M. Brekelmans. Multi-scale computational homogenization. *International Journal for Numerical Methods in Engineering*, 54:1235–1260, 2002. 13, 16, 104

[21] M. A. Gockel. *MSC Nastran handbook for superelement analysis: MSC Nastran version 61*. MacNeal-Schwendler Corporation, Los Angeles, 1982. 22

[22] T. Grätsch and K.-J. Bathe. A posteriori error estimation techniques in practical finite element analysis. *Computers & Structures*, 83(4):235 – 265, 2005. 22

[23] R. J. Guyan. Reduction of stiffness and mass matrices. *AIAA Journal*, 3(2):380–380, 1965. 22

[24] H. Hajibeygi, G. Bonfigli, M. A. Hesse, and P. Jenny. Iterative multiscale finite-volume method. *Journal of Computational Physics*, 227(19):8604–8621, 2008. 22, 104

[25] T. Hou and X. Wu. A multiscale finite element method for elliptic problems in composite materials and porous media. *Journal of Computational Physics*, 134(1):169–189, 1997. 18, 19, 104

[26] T. Y. Hou, F.-N. Hwang, P. Liu, and C.-C. Yao. An iteratively adaptive multiscale finite element method for elliptic PDEs with rough coefficients. *Journal of Computational Physics*, 336:375–400, 2017. 22

[27] T. Y. Hou and P. Liu. Optimal local multi-scale basis functions for linear elliptic equations with rough coefficients. *Discrete & Continuous Dynamical Systems*, 36(8):4451–4476, 2016. 17, 20

[28] T. Y. Hou, X.-H. Wu, and Z. Cai. Convergence of a multiscale finite element method for elliptic problems with rapidly oscillating coefficients. *Mathematics of Computation*, 68(227):913–943, July 1999. 19, 104

[29] T. J. Hughes. Multiscale phenomena: Green's functions, the dirichlet-to-neumann formulation, subgrid scale models, bubbles and the origins of stabilized methods. *Computer Methods in Applied Mechanics and Engineering*, 127(1):387–401, 1995. 18

[30] T. J. Hughes, G. R. Feijóo, L. Mazzei, and J.-B. Quincy. The variational multiscale method—a paradigm for computational mechanics. *Computer Methods in Applied Mechanics and Engineering*, 166(1):3–24, 1998. Advances in Stabilized Methods in Computational Mechanics. 18

[31] M. Klimczak and W. Cecot. An adaptive MsFEM for nonperiodic viscoelastic composites. *International Journal for Numerical Methods in Engineering*, 114(8):861–881, 2018. 18, 21, 104

[32] M. Klimczak and W. Cecot. Modeling of heterogeneous elastic materials by the multiscale hp-adaptive finite element method. volume 1922, 01 2018. 19

[33] M. Klimczak and W. Cecot. Towards asphalt concrete modeling by the multiscale finite element method. *Finite Elements in Analysis and Design*, 171:103367, 2020. 18, 104

[34] D. Li, J. Ma, L. Dong, and R. S. Lakes. Stiff square structure with a negative poisson's ratio. *Materials Letters*, 188:149 – 151, 2017. 88, 89, 106

[35] S. Li and E. Sitnikova. *Representative Volume Elements and Unit Cells: Concepts, Theory, Applications and Implementation.* Woodhead Publishing Series in Composites Science and Engineering. Elsevier Science, 2019. 16, 104

[36] H. Liu, X. Sun, Y. Xu, and X. Chu. A hierarchical multilevel finite element method for mechanical analyses of periodical composite structures. *Composite Structures*, 131:115–127, 2015. 20, 104

[37] H. Liu, Y. Wang, H. Zong, and M. Y. Wang. Efficient structure topology optimization by using the multiscale finite element method. *Structural and Multidisciplinary Optimization*, 58(4):1411–1430, Oct 2018. 21, 104

[38] H. Liu and H. Zhang. An equivalent multiscale method for 2D static and dynamic analyses of lattice truss materials. *Advances in Engineering Software*, 75:14 – 29, 2014. 21

[39] L. Madej, P. D. Hodgson, and M. Pietrzyk. Multi-scale rheological model for discontinuous phenomena in materials under deformation conditions. *Computational Materials Science*, 38:685–691, 2007. 13

[40] L. Madej, L. Sieradzki, M. Sitko, K. Perzynski, K. Radwanski, and R. Kuziak. Multi scale cellular automata and finite element based model for cold deformation and annealing of a ferritic–pearlitic microstructure. *Computational Materials Science*, 77:172–181, 2013. 13

[41] L. H. Nguyen and D. Schillinger. The multiscale finite element method for nonlinear continuum localization problems at full fine-scale fidelity, illustrated through phase-field fracture and plasticity. *Journal of Computational Physics*, 396:129–160, 2019. 22

[42] L. H. Nguyen and D. Schillinger. A residual-driven local iterative corrector scheme for the multiscale finite element method. *Journal of Computational Physics*, 377:60 – 88, 2019. 16, 22, 104, 105

[43] M. Oleksy and W. Cecot. Application of hp-adaptive finite element method to two-scale computation. *Archives of Computational Methods in Engineering*, 22(1):105–134, Jan 2015. 21, 104

[44] M. Oleksy, W. Cecot, W. Rachowicz, and M. Nessel. An improved multiscale FEM for the free vibrations of heterogeneous solids. *Computers & Mathematics with Applications*, 110:110–122, 2022. 18

[45] R. Penta and A. Gerisch. An introduction to asymptotic homogenization. In A. Gerisch, R. Penta, and J. Lang, editors, *Multiscale Models in Mechano and Tumor Biology*, pages 1–26, Cham, 2017. Springer International Publishing. 14, 104

[46] K. Raju, T. Tay, and V. B. C. Tan. A review of the FE^2 method for composites. *Multiscale and Multidisciplinary Modeling, Experiments and Design*, 4, 03 2021. 13

[47] S. Soghrati and I. Stanciulescu. Systematic construction of higher order bases for the finite element analysis of multiscale elliptic problems. *Mechanics Research Communications*, 52:11 – 18, 2013. 21

[48] P. M. Suquet. Elements of homogenization theory for inelastic solid mechanics. In E. Sanchez-Palencia and A. Zaoui, editors, *Homogenization Techniques for Composite Media*, Berlin, Heidelberg, 1987. Springer Berlin Heidelberg. 16

[49] H. A. Tchelepi, P. Jenny, S. H. Lee, and C. Wolfsteiner. Adaptive Multiscale Finite-Volume Framework for Reservoir Simulation. *SPE Journal*, 12(02):188–195, 06 2007. 18, 104

[50] K. Terada, N. Hirayama, K. Yamamoto, J. Kato, T. Kyoya, S. Matsubara, Y. Arakawa, Y. Ueno, and N. Miyanaga. Applicability of micro–macro decoupling scheme to two-scale analysis of fiber-reinforced plastics. *Advanced Composite Materials*, 23(5-6):421–450, 2014. 16

[51] K. Terada, M. Hori, T. Kyoya, and N. Kikuchi. Simulation of the multi-scale convergence in computational homogenization approaches. *International Journal of Solids and Structures*, 37(16):2285–2311, 2000. 15, 16, 101

[52] S. Ye, Y. Xue, and C. Xie. Application of the multiscale finite element method to flow in heterogeneous porous media. *Water Resources Research*, 40, 09 2004. 18

[53] H. Zhang, H. Liu, and J. Wu. A uniform multiscale method for 2D static and dynamic analyses of heterogeneous materials. *International Journal for Numerical Methods in Engineering*, 93(7):714–746, 2013. 20

[54] H. Zhang, J. K. Wu, and Z. Fu. Extended multiscale finite element method for mechanical analysis of periodic lattice truss materials. *International Journal for Multiscale Computational Engineering*, 8(6):597–613, 2010. 20

[55] H. W. Zhang, Y. Liu, S. Zhang, J. Tao, J. Wu, and B. Chen. Extended multiscale finite element method: Its basis and applications for mechanical analysis of heterogeneous materials. *Computational Mechanics*, 53:659–685, 04 2014. 18, 20

[56] H.-W. Zhang, J.-K. Wu, J. Lü, and Z.-D. Fu. Extended multiscale finite element method for mechanical analysis of heterogeneous materials. *Acta Mechanica Sinica*, 26(6):899–920, Dec 2010. 18, 104

[57] S. Zhang, J. Yin, H. Zhang, and B. Chen. A two-level method for static and dynamic analysis of multilayered composite beam and plate. *Finite Elements in Analysis and Design*, 111:1 – 18, 2016. 18, 104

List of Figures

Streszczenie

„Modelowanie właściwości mechanicznych wybranych zaawansowanych materiałów za pomocą wieloskalowych elementów skończonych”

Rozdział 1: Wprowadzenie

W ostatnich latach można zaobserwować znaczący postęp w dziedzinie nowych materiałów i technologii ich wytwarzania. Najlepszym tego przykładem są kompozyty, metamateriały, i elementy wytwarzane w technologii druku 3D. Ich nowe właściwości są uzyskiwane poprzez łączenie kilku materiałów bazowych (kompozyty) lub poprzez układanie materiału w przestrzeni tak, aby uzyskać specyficzną mikrostrukturę (metamateriały, druk 3D). Naukowcy znajdują zastosowanie tych materiałów w kluczowych gałęziach nauki i przemysłu, takich jak astronautyka, medycyna, przemysł samochodowy, czy budownictwo. Zasadniczą częścią procesu projektowania nowego materiału są kosztowne i czasochłonne eksperymenty laboratoryjne. Wspomagane są one również obliczeniami numerycznymi, które pozwalają znacząco skrócić czas i koszt projektowania.

Wieloskalowa struktura zaawansowanych materiałów wymaga uwzględnienia skali mikro w symulacjach komputerowych. Zadanie to, opisywane przez równania różniczkowe z oscylującym współczynnikiem, jest trudne do bezpośredniego rozwiązania za pomocą standardowych metod numerycznych takich jak np. metoda elementów skończonych (MES) ze względu na rozmiar problemu (liczbę stopni swobody) i czas obliczeń. Dlatego rozwijane są wieloskalowe metody numeryczne, które poprzez stworzenie relacji pomiędzy skalą makro i mikro, pozwalają na przeprowadzanie obliczeń w skali makro jednocześnie uwzględniając w obliczeniach skalę mikrostruktury materiału. Jedną z takich metod jest wieloskalowa metoda elementów skończonych (MsFEM).

W niniejszej pracy podjęto próbę zastosowania MsFEM w modelowaniu numerycznym mechaniki zaawansowanych materiałów. Zaproponowano oryginalne modyfikacje metody oraz przeprowadzono szereg numerycznych testów sprawdzających dokładność i skuteczność metody. Ponadto zaproponowano adaptację MsFEM do modelowania elementów wytwarzanych w technologii druku 3D. Numerycznym testom towarzyszyły nowatorskie pomiary eksperymentalne na próbkach wykonanych za pomocą druku 3D przeprowadzone w celu walidacji metody.

Rozdział 2: Przegląd literatury

W literaturze można znaleźć wiele metod, które dedykowane są problemom wieloskalowym i rozwiązują podjęte zadanie w różny sposób m.in. metoda homogenizacji asymptotycznej [45] lub metoda wykorzystująca reprezentatywny element objętości (RVE) [35], czy dwupoziomowa metoda elementów skończonych (FE^2) [20].

Metoda MsFEM zaproponowana przez Hou i Wu [25] zakłada utworzenie rzadkiej siatki makroelementów, z reguły nie uwzględniającej mikrostruktury. Ideą metody jest obliczanie funkcji bazowych siatki rzadkiej rozwiązując zagadnienie brzegowe z tym samym równaniem różniczkowym co oryginalny problem. W praktyce obliczane są funkcje kształtu w każdym makroelemencie używając siatki gęstej, która jest dopasowana do mikrostruktury. Następnie przeprowadzane są globalne obliczenia jak w klasycznej metodzie elementów skończonych na siatce rzadkiej. Umożliwia to znaczne zmniejszenie liczby stopni swobody przy jednoczesnym uwzględnieniu informacji o złożonej mikrostrukturze, która jest wbudowana w funkcje bazowe. Zaletą metody jest fakt, iż obliczenia dla poszczególnych makroelementów odbywają się w sposób całkowicie niezależny. Umożliwia to zrównoleglenie algorytmu, co dodatkowo skraca czas obliczeń.

Obliczania wieloskalowe wiążą się z wprowadzeniem dodatkowych błędów numerycznych. Autorzy oryginalnej metody zauważyli, że jakość otrzymanego rozwiązania zależy w dużej mierze od warunków brzegowych w zagadnieniu obliczania funkcji kształtu (efekt rezonansu). Aby zniwelować ten efekt zaproponowana została technika „oversampling" [25, 28], w której problem funkcji kształtu jest rozwiązywany w większym obszarze niż jeden makroelement, a z jego wyników generowane są oscylujące funkcje kształtu na brzegu danego makroelementu. Stosowano również periodyczne warunki brzegowe, podobne jak w metodzie RVE [56].

Innym podejściem poprawiającym rozwiązanie metody MsFEM jest zwiększanie liczby stopni swobody analogiczne do zwiększania stopnia aproksymacji w MES. Nowe funkcje kształtu wyższego rzędu w MsFEM zostały wprowadzone na bazie wielomianów Lagrange'a [19] oraz funkcji hierarchicznych [36, 6]. To podejście zostało wykorzystane w algorytmie adaptacji [43, 31] oraz w zadaniu optymalizacji topologii [37].

Zastosowanie siatki rzadkiej i siatki gęstej umożliwia w łatwy sposób wykorzystanie iteracyjnego podejścia korekcji rozwiązania. Ponadto, zaadaptowano w MsFEM podejście z metody multigrid [24] oraz lokalną korekcję w nośnikach funkcji bazowych [42]. Dla tego ostatniego przykładu metoda zbiega się do rozwiązania z siatki gęstej.

Oryginalnie MsFEM został opracowany w celu skutecznego rozwiązywania problemów przepływu w niejednorodnych ośrodkach porowatych wykorzystywanych w symulacjach złóż ropy naftowej i gazu ziemnego [49]. Metoda została później zaadaptowana do problemów sprężystości kompozytów i metamateriałów w [56]. Przy użyciu MsFEM modelowano m. in. problem zginania belek i płyt [57], lepkosprężysty beton asfaltowy [31, 33], czy kompozyty piezoelektryczne [18].

Rozdział 3: Pełne teksty artykułów stanowiących rozprawę doktorską

W tym rozdziale pracy zamieszczono pełne teksty artykułów stanowiących rozprawę doktorską. Poniżej znajduje się lista z danymi bibliograficznymi artykułów wraz z punktacją zgodną z wykazem czasopism naukowych Ministerstwa Edukacji i Nauki oraz współczynnik wpływu czasopism (Impact Factor, IF):

Artykuł 1 M. Dryzek i W. Cecot. A coupling of multiscale finite element method and isogeometric analysis. *International Journal for Multiscale Computational Engineering*, 18(4):439–454, 2020. 40 punktów, IF = 1.591.

Artykuł 2 M. Dryzek i W. Cecot. The iterative multiscale finite element method for sandwich beams and plates. *International Journal for Numerical Methods in Engineering*, 122:6714–6735, 2021. 200 punktów, IF = 3.477.

Artykuł 3 M. Dryzek i E. Dryzek. Positron annihilation lifetime spectroscopy of ABS objects manufactured by fused deposition modelling. *Acta Physica Polonica A*, 132(5):1506-1508 , 2017. 40 punktów, IF = 0.577.

Artykuł 4 M. Dryzek, W. Cecot, i M. Tekieli. Experimental and multiscale computational static and dynamic study of 3D printed elements with mesostructure. *Finite Elements in Analysis and Design*, 215:103876, 2023. 100 punktów, IF = 2.618.

W następnych podrozdziałach zamieszczono streszczenie każdego z nich.

Artykuł 1: Połączenie metody MsFEM z analizą izogeometryczną

W artykule zaproponowane zostało budowanie wieloskalowych funkcji bazowych MsFEM wykorzystując krzywe B-sklejane wyższego rzędu rozpięte na kilku makroelementach. Główną cechą tego podejścia jest obliczanie funkcji bazowej w jednym kroku w całym jej nośniku, w przeciwieństwie do standardowych funkcji kształtu stosowanych w MsFEM, które są obliczane element po elemencie siatki zgrubnej i sklejane w czasie agregacji.

Przeprowadzono wybrane eksperymenty numeryczne na przykładzie zagadnienia przepływu w ośrodkach porowatych z periodycznym i losowym rozkładem właściwości materiału, aby przetestować zmodyfikowaną metodę MsFEM z nowymi funkcjami bazowymi. Uzyskano lepsze wyniki od standardowej metody nawet z techniką oversampling. Zaobserwowano jednak efekt rezonansu, gdy stosunek wielkości wtrąceń do rozmiaru siatki zgrubnej dążył do jednego. Pokazano, że jest możliwa redukcja tego efektu poprzez zwiększenie rzędu krzywych B-sklejanych.

Artykuł 2: Iteracyjna metoda MsFEM dla belek i płyt warstwowych

W artykule zaadaptowano metodę MsFEM do analizy belek i płyt warstwowych ze złożoną strukturą kompozytową. Zaproponowana modyfikacja znacząco zmniejsza liczbę stopni swobody modelu obliczeniowego (nawet o cztery rzędy) dzięki anizotropowej aproksymacji wyższego rzędu oraz nowym funkcjom kształtu uwzględniającym niektóre warunki brzegowe. Co więcej, w algorytmie wykorzystano iteracyjny schemat korekcyjny [42] odpowiednio zmodyfikowany do problemów zginania. Dzięki temu możliwe jest odtworzenie rozwiązania z siatki rzadkiej. Przedstawiono kilka przykładów obliczeniowych, aby zademonstrować możliwości metody. Stwierdzono, że zaproponowane modyfikacje funkcji kształtu i aproksymacja wyższego rzędu zwiększają zbieżności algorytmu iteracyjnego. Na koniec poddano walidacji model wieloskalowy, porównując wyniki numeryczne z wynikami eksperymentalnymi uzyskanymi w próbie zginania warstwowej płyty falistej o dużej gęstości. Zaobserwowano bardzo dobrą zgodność obu wyników dla pojedynczej iteracji algorytmu.

Artykuł 3: Spektroskopia czasu życia pozytonów w obiektach z ABS wytworzonych w procesie osadzania topionego materiału

W artykule przeprowadzono badania z wykorzystaniem spektroskopii czasu życia pozytonów (PALS) na próbkach z polimeru akrylonitrylo-butadieno-styrenowego (ABS) wytworzonych w procesie osadzania topionego materiału w celu zbadania możliwości identyfikacji różnic w mikrostrukturze. Przygotowano zestaw próbek składający się z płytek kwadratowych i długich prostokątnych (o długości 100 mm i 200 mm) wytwarzanych tak, że ustawienie wszystkich włókien materiału jest równoległe do dłuższej krawędzi. Stosowano różne odległości między włóknami, co skutkuje różnym nakładaniem się osadzanego materiału w kierunku poziomym i pionowym. Nieznaczny wzrost czasu życia orto-pozytonium, wskazujący na wzrost średniego promienia wolnej objętości, zaobserwowano dla najdłuższych próbek, dla których spodziewany jest największy wpływ nakładania się włókien w kierunku poziomym. Nie zaobserwowano różnic dla parametru odległości między włóknami. Badania przeprowadzono w Instytucie Fizyki Jądrowej PAN w Krakowie, w pracowni anihilacji pozytonów.

Artykuł 4: Eksperymentalne i wieloskalowe numeryczne badania elementów drukowanych 3D z mezostrukturą w warunkach obciążenia statycznego i dynamicznego

W artykule przedstawiono wyniki przeprowadzonych badań eksperymentalnych elementów ze złożoną mezostrukturą drukowaną metodą osadzania topionego materiału. Wyniki eksperymentalne posłużyły do walidacji modelu numerycznego metody MsFEM z aproksymacją wyższego rzędu. Zaproponowano trójskalowe podejście w modelu numerycznym: w mikroskali ścieżki włókien filamentu są homogenizowane przy użyciu ortotropowego modelu materiału o eksperymentalnie zidentyfikowanych właściwościach; w mezoskali wydrukowana struktura jest wbudowana do funkcji kształtu MsFEM; w makroskali całe zadanie jest ostatecznie rozwiązywane. Aby zweryfikować podejście przeprowadzono eksperymentalne pomiary statycznego zginania oraz drgań swobodnych belek o czterech różnych mezostrukturach i dwóch orientacjach drukowania. Pomiary wykonano z wykorzystaniem optycznego systemu pomiaru deformacji pola odkształcenia. Wyniki eksperymentalne zostały bardzo dobrze odtworzone przez model numeryczny w wielu przykładach. Ponadto badanie ujawniło, że hierarchiczne funkcje kształtu wyższego rzędu mogą dokładnie reprezentować drgania swobodne nawet dla wysokich częstotliwości.

Rozdział 4: Walidacja eksperymentalna

W tym rozdziale zamieszczono zdjęcia próbek i elementów badanych w czwartym artykule oraz wyniki badań numerycznych metamateriału z ujemnym współczynnikiem Poissona zaprojektowanym na podstawie badań eksperymentalnych z [34].

Ujemny współczynnik Poissona materiału oznacza, że materiał poddany rozciąganiu będzie również rozszerzał się w kierunku poprzecznym. Takie zachowanie materiału jest spowodowane obecnością periodycznej mezostruktury, której elementy skręcają się i zginają podczas rozciągania próbki. Materiał z mezostrukturą nazywany jest metamateriałem. Zaproponowano eksperyment numeryczny, w którym wyznaczano współczynnik Poissona wybranego metameteriału przy pomocy wyników uzyskanych metodą MsFEM dla różnego stopnia aproksymacji oraz z wykorzystaniem techniki oversampling. Wykazano zmniejszenie się błędu rozwiązania mierzonego w normie L_2 oraz w normie

energetycznej względem rozwiązania referencyjnego wraz ze wzrostem stopnia aproksymacji. Zaobserwowano również zwiększenie błędu przy zmniejszaniu rozmiaru siatki rzadkiej, co wskazuję na silny efekt rezonansu. Rozwiązanie uzyskane techniką oversampling jest najbardziej zbliżone do rozwiązania referencyjnego. Dla najmniejszego rozmiaru makroelementów współczynnik Poissona uzyskany z liniowymi funkcjami był dodatni i wyniósł 0.0028. Przy zwiększaniu stopnia aproksymacji uzyskano współczynnik równy -0.11. Korzystając z techniki oversampling uzyskano współczynnik -0.28. Wynik referencyjny to -0.35, a wynik z eksperymentu to -0.28.

Rozdział 5: Podsumowanie

Niniejsza rozprawa obejmuję temat modyfikacji i testowania wieloskalowej metody elementów skończonych w kontekście zaawansowanych materiałów. W pracy przedstawiono przegląd literatury dotyczącej metody, autorskie modyfikacje, testy numeryczne oraz eksperymentalną walidację metody.

Przeprowadzono liczne testy i walidację metody MsFEM z hierarchicznymi funkcjami bazowymi. Wykazano, że błąd rozwiązania wieloskalowego można zmniejszyć, zwiększając liczbę stopni swobody nawet w skrajnym przykładzie materiału o ujemnym współczynniku Poissona. Wykorzystano funkcje wyższego rzędu w problemach belek i płyt. Łącząc to podejście z iteracyjnym schematem korekcji, udało się zwiększyć szybkość zbieżności metody. Zaproponowano ponadto nowy sposób budowania wieloskalowych funkcji bazowych i zwiększania liczby stopni swobody wykorzystując krzywe B-sklejane. Wykazano, że to podejście dla pewnych rozmiarów makroelementów daje wyniki lepsze od standardowej metody MsFEM z techniką oversampling. Jednak w tym podejściu zauważono silny efekt rezonansy. Udało się go zmniejszyć, zwiększając rząd krzywych B-sklejanych.

Metoda MsFEM została poddana walidacji poprzez porównanie z wynikami z eksperymentów na próbkach wytwarzanych w technologii druku 3D. Rozwiązania numeryczne z modelów wieloskalowych z funkcjami wyższego rzędu dobrze korelowały z wynikami eksperymentalnymi statycznego zginania. Błędy rozwiązania znajdowały się w przedziale 2-5%. W testach dynamicznych zmierzone częstotliwości drgań własnych badanych próbek zostały przewidziane przez model MsFEM z błędem 5%.

Do oryginalnych aspektów pracy należą:

1. Zastosowanie krzywych B-sklejanych w algorytmie MsFEM obejmujące implementację idei i testy numeryczne dla problemu przepływu w stanie ustalonym w ośrodkach niejednorodnych.

2. Adaptacja MsFEM do analizy belek i płyt warstwowych z wykorzystaniem hierarchicznych funkcji wyższego rzędu i iteracyjnego schematu korekcyjnego. Implementacja i testy numeryczne na przykładach struktur 2D i 3D oraz walidacja z danymi eksperymentalnymi.

3. Nowatorskie testowanie elementów z ABS wytworzonych w technologii druku 3D przy użyciu optycznego systemu pomiaru deformacji pola odkształcenia, akcelerometru, i spektroskopii czasu życia pozytonów.

4. Zastosowanie MsFEM do analizy mechanicznej elementów wytwarzanych w technologii druku 3D i walidacja poprzez porównanie wyników z modelu numerycznego z eksperymentami.

5. Testowanie MsFEM na przykładzie problemu metamateriału o ujemnym współczynniku Poissona w celu identyfikacji jego właściwości.

Istnieje szereg dyscyplin naukowych i inżynierskich, w których zaawansowane materiały znajdują zastosowanie. Autor uważa, że dalsze badania nad modelowanie wieloskalowym materiałów kompozytowych i metamteriałów oraz rozwój metod wieloskalowych takich jak metoda MsFEM, przyspieszy postęp w tych dyscyplinach. Dalsze badania nad rozwojem metody MsFEM mogą obejmować implementację i testowanie innych modeli konstytutywnych. Innym aspektem przyszłych badań mogą być wspominane przez wielu autorów artykułów trudności związane z przygotowaniem modelu MsFEM np. trudność z siatkowaniem w skali gęstej, zwłaszcza blisko granicy makroelementów, co może prowadzić do nieregularności siatki i pogorszenia właściwości przestrzeni aproksymującej. Potencjalnym rozwiązaniem może być rozdzielenie siatki gęstej i siatki rzadkiej korzystając z metod niedostosowanych elementów skończonych (unfitted finite element method). W tych metodach problem jest rozwiązywany przy pomocy standardowej metody elementów skończonych, ale powierzchnie międzyfazowe lub granice geometrii siatki rzadkiej są zintegrowane w sformułowaniu wariacyjnym, a siatka gęsta nie musi być dopasowana do tej geometrii. Może to ułatwić proces przygotowywania wieloskalowych modeli i korzystanie z MsFEM w komercyjnie dostępnym oprogramowaniu.